University of Évora

ARCHMAT
(ERASMUS MUNDUS MASTER IN ARCHaeological MATerials Science)

Mestrado em Arqueologia e Ambiente (Erasmus Mundus – ARCHMAT)

Assessing the impact of 74ka Toba Super eruption on palaeovegetation of Late Pleistocene South Asia using sedimentary organic biomarkers

Avaliação do impacto da erupção do supervulcão Toba à 74ka na vegetação do Pleistoceno Superior no Sul da Ásia através da análise de biomarcadores em sedimentos

Gopesh Jha
m44415

Cristina Maria Barrocas Dias
(Supervisor – Universidade de Évora)

Nicasio Tomás Jiménez-Morillo
(Co-supervisor – Universidade de Évora)

Ana Zélia Miller
(Co-supervisor – Universidade de Évora)

Évora, Portugal, December 2021

A tese inclui as criticas e sugestões do Júri

Jury members:

Presidente: Nicola Schiavon

Investigador Principal Convidado - Universidade de Évora

Arguente:
Carlos Alexandre da Silva Ribeiro, Prof. Auxiliar (Departamento de Geociências), Universidade de Évora.

Orientador:
- Cristina Maria Barrocas Dias, Prof. Associado c/ Agregação (Departamento de Química e Bioquímica), Universidade de Évora.
- Nicasio Tomás Jiménez-Morillo, Doutora, Universidade de Évora.
- Ana Zélia Miller, Doutora, Universidade de Évora.

Vogal:
- Donatella Magri Professora Associada Università di Roma La Sapienza
- Federico di Rita, Professora Associada Università di Roma La Sapienza
- Spathis Panagiotis, Professor, Laboratory of Chemical and Environmental Technology, Aristotle University of Thessaloniki.

Resumo

A erupção de ~74ka Toba é considerada o maior evento vulcânico explosivo dos últimos 23 milhões de anos, com um Índice de Explosividade Vulcânica (VEI) de 8,8. Pensa-se que tenha causado um caos global, levando a um arrefecimento global drástico e a um estrangulamento populacional. Muitos registos climáticos globais e estudos de simulação mostraram que ~74ka erupção de Toba teve um impacto severo no hemisfério norte e pode ter afectado também zonas hiper-áridas do hemisfério sul. No entanto, é difícil dizer a manifestação do impacto de Toba no ambiente terrestre local e regional devido à falta de registos ambientais terrestres bem actualizados. A investigação actual fornece uma imagem holística do cenário paleo-ambiental de duas zonas biogeográficas diversas (isto é, planície costeira e inter-montano) que estão directamente associadas ao jovem Toba tufo (YTT). A investigação multi-proxy destes locais levou a seguir inferências: 1) O ambiente local de Tejpor e Jwalapuram já estava inclinado para condições mais secas antes do evento de Toba, sugerindo sinais de evento global GI-20S; 2) Jwalapuram mostra o impacto imediato da erupção de YTT em termos de ambiente húmido e seco altamente instável e oscilante, a queda de cinzas sufocou o sistema fluvial e causou também um certo grau de desflorestação; 3) Tejpor mostra o impacto a longo prazo do YTT, o ambiente local parece ter-se tornado mais seco embora a rotação climática não seja tão severa. A investigação actual sugere que Toba tem um impacto notável que varia no tempo (duração), bem como no espaço. No entanto, é altamente improvável que tenha desencadeado um evento de nível de extinção, uma vez que ambos mostram o sinal de um rápido ressurgimento.

Abstract

The ~74ka Toba eruption is considered the largest explosive volcanic event of the last 23 million years, with a Volcanic Explosivity Index (VEI) of 8.8. It thought to have caused global havoc, leading to drastic global cooling and population bottleneck. Many global climatic records and simulation studies have shown that ~74ka Toba eruption had severe impact on northern hemisphere and may have affected hyper-arid zones of southern hemisphere as well. However, it is hard to tell the manifestation of Toba impact on local and regional terrestrial environment due to lack of well-dated terrestrial environmental record. Current research provides holistic picture of paleoenvironmental setting of two diverse bio-geographical zones (i.e., coastal plain and inter-montane) that are directly associated with young Toba tuff (YTT).

Multi-proxy investigation of these sites led to following inferences: 1) Local environment of Tejpor and Jwalapuram was already inclined towards drier conditions prior to Toba event, suggesting sign of global GI-20S event; 2) Jwalapuram shows immediate impact of YTT eruption in terms of highly unstable and oscillating wet-dry environment, ashfall choked the riverine system and caused certain degree of deforestation as well; 3) Tejpor shows the long-term impact of YTT, local environment seems to have become drier although climatic turnover is not that severe. Current investigation suggest that Toba does have remarkable impact that varies in time (duration) as well as space. However, it is highly unlikely that it would have triggered extinction level event, as both shows the sign of rapid resurgence.

ACKNOWLEDGEMENT

Content

List of abbreviations

ACL: Average chain length

ATR-FTIR: Attenuated total reflectance-Fourier-transform infrared spectroscopy

CAM: Crassulacean acid metabolism

CIA: Chemical Index of Alteration

CIW: Chemical Index of Weathering

CPI: Carbon preference index

CT: Computed Tomography

DNA: Deoxyribonucleic acid

D-O: Dansgaard–Oeschger events

DRE: Dense-rock equivalent

EA-IRMS: Elemental analysis - Isotope ratio mass spectrometry

ED-XRF: Energy dispersive X-ray fluorescence

GC-MS: Gas chromatography – Mass spectrometry

GI: Greenland interstadials

GISP: Greenland ice sheet project

GS: Greenland stadial

HDT: Haranggoal Dactite tuff

JWP: Jwalapuram

Ka: Kilo year ago

KDAP: Kadapa district archaeological project

Loc.: Locality

LOI: Loss on ignition

MIS: Marine isotope stages (also known as Oxygen Isotope Stages)

MTT: Middle Toba tuff

OM: Organic Matter

OSL: Optically stimulated luminescence

OTT: Old Toba tuff

Paq.: Aquatic plant *n*-Alkane proxy

PIA: Plagioclase Index of Alteration

Pwax.: Terrestrial plant *n*-alkane proxy

Py-GC-MS: Pyrolysis - Gas chromatography – Mass spectrometry

R: Ruxton Index

REE: Rare earth elements

Sa: Silicon to aluminium ratio (Sa)

Saf: Silicon to aluminium plus iron ratio

SEM-EDS: Scanning electron microscopy (SEM)- Energy dispersive X-ray spectroscopy

TAR: Terrigenous Aquatic Ratio

TJP: Tejpor

TOM: Total organic matter

V: Vogt's Index

VEI: Volcanic Explosivity Index

WIP: Weathering Index of Parker

XRD: X-ray diffraction

YTT: Young Toba tuff

Chapter I

Introduction

Paleoenvironmental research has shown the prominent impact of environmental fluctuation on human subsistence and resulting behavioural transformation[1–3]. Especially in a region like South Asia which is heavily affected by the monsoonal trends, triggering changes in precipitation, and can cause a massive spatial shift in river boundaries[4]. The recurrent shifts in monsoonal intensity at the onset of different glacial and interglacial phases must have triggered crucial changes within the local and regional environment[31] which may have led to the reduction in the availability of freshwater resources, disturbance of morphological processes, and a higher intensity of natural calamities [4,5]. These environmental fluctuations are often regarded as a shaping force behind changing human behaviour. Hence, it is critical for understanding the impact of these fluctuations and how they are manifested in the behavioural records of archaic human populations[1]. The ~74 ka Toba super eruption is one of the major events happened during late Pleistocene which thought to have created climatic havoc during late Pleistocene and resulted into near-extinction event [6–8].

1.1. Research question and objectives

Proposed project intends to explore the very crucial problem which comes in the reaches of the fields of human ecology, evolutionary anthropology, and ancient climate studies. It intends to examine the nature of human-environment interaction between water availability, plant landscape and human behavioural markers. It is extremely crucial to understand the impact of cataclysmic event like Toba on human-environment interaction.

Iconic paper of Harpending *et. al.*[9] argued, based on genetic evidence that sometime prior to ca. 60 ka hominin populations across the globe suffered a severe population bottleneck. Estimated human population that survived was around 3,000 to 10,000. It was hypothesized that ~74 ka eruption of Toba caused such planetary havoc and led to global climatic disruption and drastic reduction of global human population[6,10,11]. Key aspect of the Toba hypothesis is the correlation between following factors: temporal context of genetic bottleneck, onset of MIS 4, D-O interstadial 20, technological transitions and temporal context of young Taoba eruption. Correlations presented by Ambrose *et. al.*[7,10] was highly criticized and defined as a theoretical model which lacks several pieces of evidence. Different scholars have negated it and stated

that the association between YTT and aforementioned events are purely circumstantial[12–16]. Therefore, an alternative and less catastrophic explanation was proposed, arguing Toba has minimal or no impact on late Pleistocene environment and archaic or modern human populations [12,14,16–19]. However, the current subject needs deeper investigation and demand more emphasis on spatial variability of the environmental impact[20,21]. Research on Toba is full of ambiguity as many of the aforementioned studies fails to assess its direct impact on human population. Most of the studies lacks well-defined and high-resolution chronology, poor sedimentary context, unavailability of paleoenvironmental data and poor correlation with archaeological assemblages[21,22].

The uncertainty masks the exact impact of ~74 ka Toba eruption on past human population and paleoenvironment highlights the demand for research that employs more pragmatic approach to test this problem. Current investigation represents the first detailed multi-proxy paleoenvironmental reconstruction of YTT associated site in South Asia, discussing probable impact of Toba super eruption on sedimentary and vegetational environment. The main intention is to explore the paleoenvironmental dynamics before and after Toba eruption and verifying the possibility if environmental conditions became deteriorated and inhospitable due to ~74 ka Toba super eruption. It is important to understand that different environmental settings or eco-niche will respond different to climatic stress[20,23]. Thus, different regions (region stands for environmental zones) must have responded differently to this catastrophic event[24].

Local-scale impacts are defined as changes occurring at the level of the habitat or eco-niche, and thus at the level of the local hominin groups that occupied these areas at that point of time. The aim of this level of assessment is to obtain high resolution paleoenvironmental, and paleopedological data from specific areas (i.e., the Tejpor and Jwalapuram) with the aim to make relatively robust conclusions rather than the more general observations which are often made at global or regional scale. Current investigation allows us to compare and place local climatic records into regional and global climatic framework, enabling us to discuss local manifestation of global climatic changes.

1.2. Research Methodology

The impact of ~74 ka Toba eruption on local environment is assessed through the sedimentological analysis of pre-Toba, Toba and post-Toba sediments from two sites of Tejpor and Jwalapuram in western and southern India respectively. Sediment samples are analysed

using geochemical techniques to understand the environmental changes caused due to Toba eruption. Current investigation put special emphasis on two major environmental factors, i.e., paedogenic processes (soil-formation process) and paleovegetation. Paleopedological factors are analysed by ED-XRF, XRD, ATR-FTIR and SEM-EDS techniques with the intention to explore changes in elemental and mineralogical cycle caused due to Toba eruption. Paleovegetation reconstruction is major part of this study. Current work employed leaf-wax biomarker analysis (GC-MS) to characterize the nature of plantscape before and after Toba eruption.

1.3.Organisation of the thesis

Current chapter further discusses following components: research background explaining the important facets of Toba eruption and why it holds very important place in Human origins research.

Chapter II explains the material and methods used in the current investigation. Different analytical techniques are briefly explained along with their theoretical principle, protocol and how they are contextualized for current investigation.[25]

Chapter III is dedicated to the results of different geochemical analysis. It discusses the highlights and reporting of the results and explains the different facets of environmental trajectory. Chapter III is divided into three parts: Sediment screening, Inorganic paleoenvironmental proxies, and Organic paleoenvironmental proxies. The sediment screening section discusses the results of FTIR, Micro-CT, and SEM-EDS. The sediment screening section is followed by the section of Inorganic paleoenvironmental proxies, and organic paleoenvironmental proxies where the results of ED-XRF, XRD, and GC-MS are presented and discussed. Current chapter only discusses the observation which are made in regard to paleoenvironmental processes. Additional data and other necessary information are provided as a supplementary information.

Chapter IV is the last chapter that explain the inferences withdrawn from different data obtained within the thesis. It explains the individual perspective of each analysis and how they complement each other. Chapter IV summed up by a brief conclusion that explains the feasibility of current observations and how they contribute towards the current research about the ~74ka Toba eruption. It also provides an outlook explaining the future premise of current research.
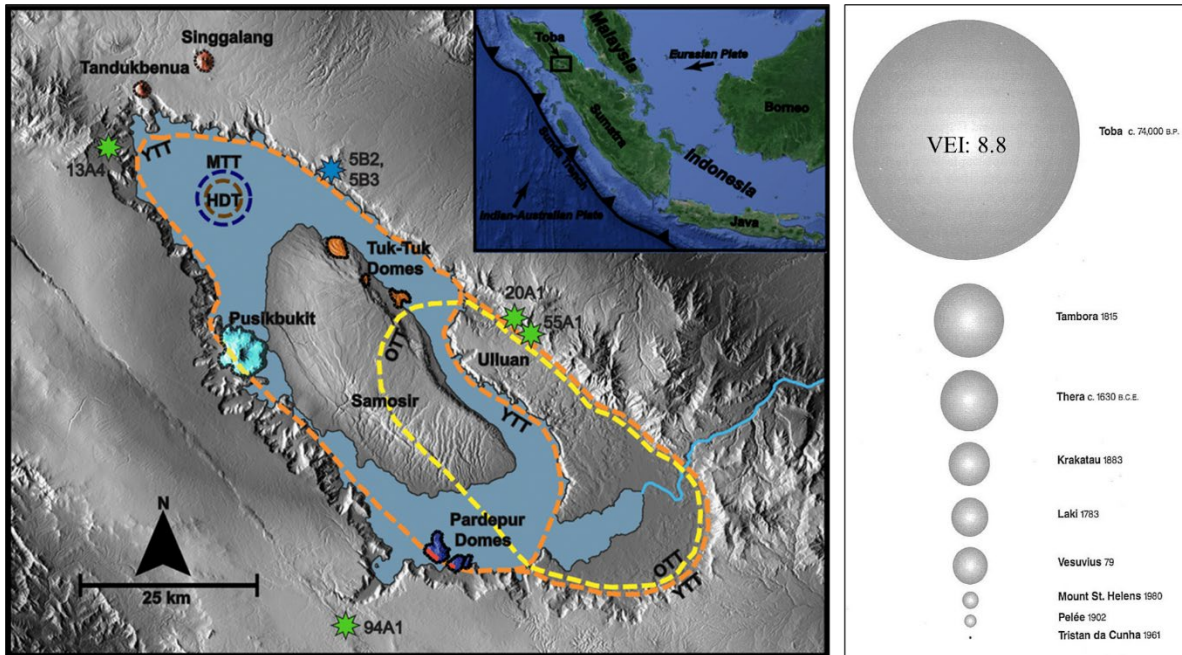
Figure 1: Location inset and DEM map of the Toba Caldera Complex showing location of the caldera and outline of major eruptions (coloured dashed lines), post-YTT lava domes and nearby volcanic centres (color highlighted landforms), and pumice locations for this study (coloured stars). Boundaries taken from Chesner (1998).

1.4. Research Background

Toba Super-eruption

Toba volcano of northern Sumatra in western Indonesia, is one of the most important volcanoes of Sunda volcanic arc (Sunda Trench). Geographically, it falls in the subduction zone which marks the tectonic boundary between Indian-Australian boundary. It has been observed that the volcanoes which falls in the subduction zones are the most hazardous and dangerous to the local as well as global ecology[26]. It explains why ~74 ka Toba eruption turned out to be a massive planetary event. With a VEI (Volcanic Explosivity Index) of 8.8, ~74 ka Toba eruption is the largest explosive event in the last 23 million years[21,27]. Toba caldera is known as one of the massive quaternary calderas covering the spatial span of 3000 km^2.

Toba caldera experienced four major eruptions during Pleistocene epoch: Haranggoal Dactite Tuff (HDT) – 1.2 ma; Oldest Toba Tuff (OTT) - ~840 ka; Middle Toba Tuff (MTT) – ~501 ka; Youngest Toba Tuff (YTT) - ~74[28] or 75 ka (75.0 ± 0.9 ka) [29]. These four-eruption resulted into the massive magma production that is estimated around 3400 km^3. However, ~74 ka YTT is the greatest among the four, it produced 82.3% (i.e., 2800 km^3) of total mass of magma expelled by Toba caldera[30,31]. Maximum proportion (~2000 km^3) of DRE is predominated by

thick ignimbrite deposits masking the wide area of 20,000 to 30,000 km^2. The hot and hazardous pyroclastic flow estimated to have wiped out the local[32]. Subsequently, it led to the collapse of the roof of the magma chamber and resulting into the formation of the Toba caldera[24]. It ended up creating a great depression that was later filled by a lake spanning ~35
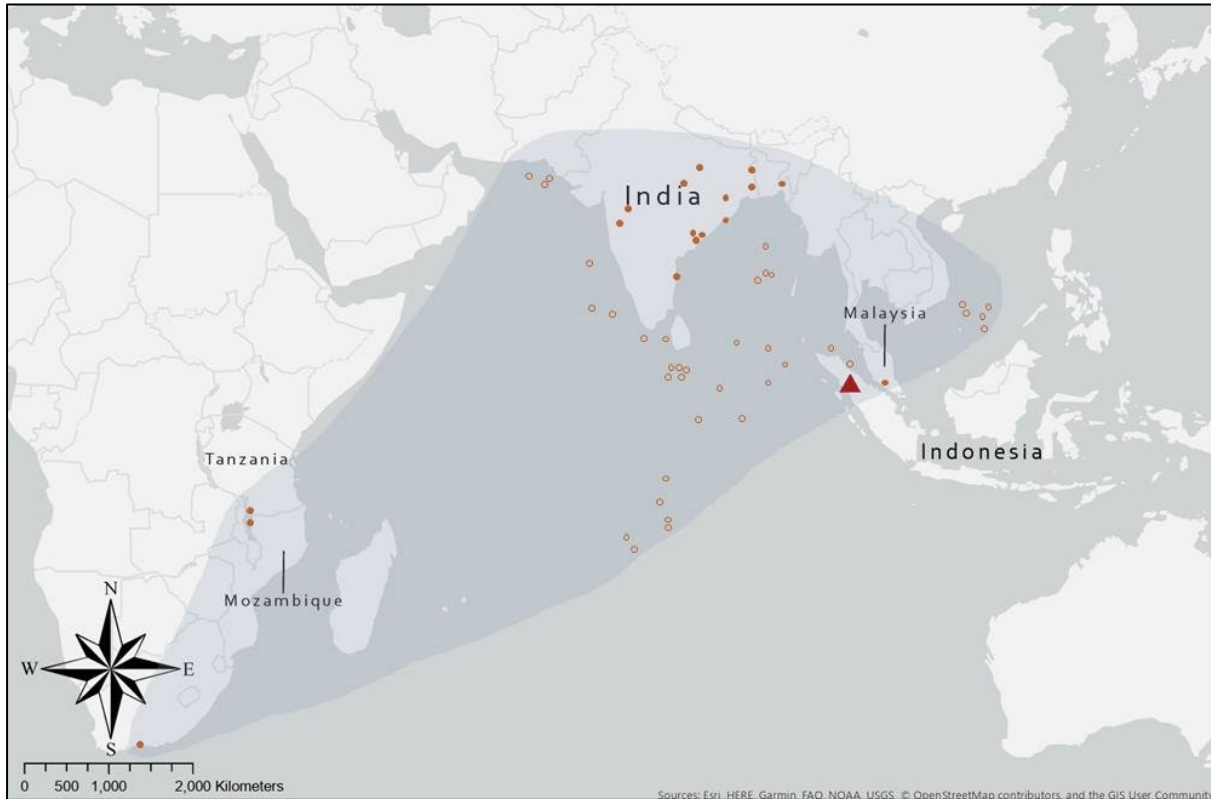
Figure 1.2 Map of sites with identified YTT tephra and/or tephra (adapted from Lane et al. 2013), with Toba caldera marked as a red triangle. No*n*-filled circles depict marine core sites, filled circles indicate terrestrial sites.

by ~95 km. Many volcanologists refer Toba caldera complex as a Toba volcano-tectonic depression[28].

Massive amount of volcanic tuff was also injected in the stratosphere forming cloud, holding the massive mass of tuff (estimated around ~800 km^3). Strong stratospheric wind led to the rapid dispersal of distal Toba tuff[21] probably during south-west monsoon as tuff travelled both to the east and west of Sumatra[33]. The distal tephra falls out masked the vast area of ~40 million km^2 [21]. Furthermost cryptic trace of YTT is reported from Lake Malawi (7300 km w. of Lake Toba) and southern cape coast of South Africa (9000 km). The massive deposits of YTT are found across peninsular India, within the fluvial deposits of several river basins[34,35].

Earlier scholars have considered YTT as an isochronous marker[8,29,35]. However, most of the YTT deposits in South Asia are redeposited tuff which dates much younger in nature[36,37]. Hence, it is highly sceptical to consider YTT as a chronological marker in South Asian context,

which might create temporal ambiguity. Ambiguous temporality of YTT have created a problem for archaeologists and paleoenvironmentalists in terms of its sedimentary context.

Toba eruption and Modern Human origins

Two different models have been proposed concerning Toba and its impact on paleoenvironment and archaic population. The first model is proposed by Ambrose[10] and Rampino and Ambrose[6] where they hypothesize the relationship between the Toba eruption and major behavioural shift which occurred during the Late Pleistocene. List of argument was proposed under the model of "Weak garden of Eden", it was argued that YTT creates a population bottleneck event (among the population of H. *sapiens* and archaic populations) which was reflected in the Late Pleistocene genomic record (mismatch distributions of mitochondrial DNA)[9]. It is argued that ~74 ka Toba eruption thought to have wiped-out the massive human population around the globe, leaving a residual population of 3,000 to 10,000 individuals (fig. 1.3). Similar signatures of population bottleneck are also noticed in the genetic record of eastern African Chimpanzees [38]. It is also believed that massive eruption accelerated the long-term cooling trend which coincides with the onset of MIS 4/GI-20S/D-O-9 event[6]. Zielinski *et al.*[11] reported that cooling already had begun before the sulphate peak in the
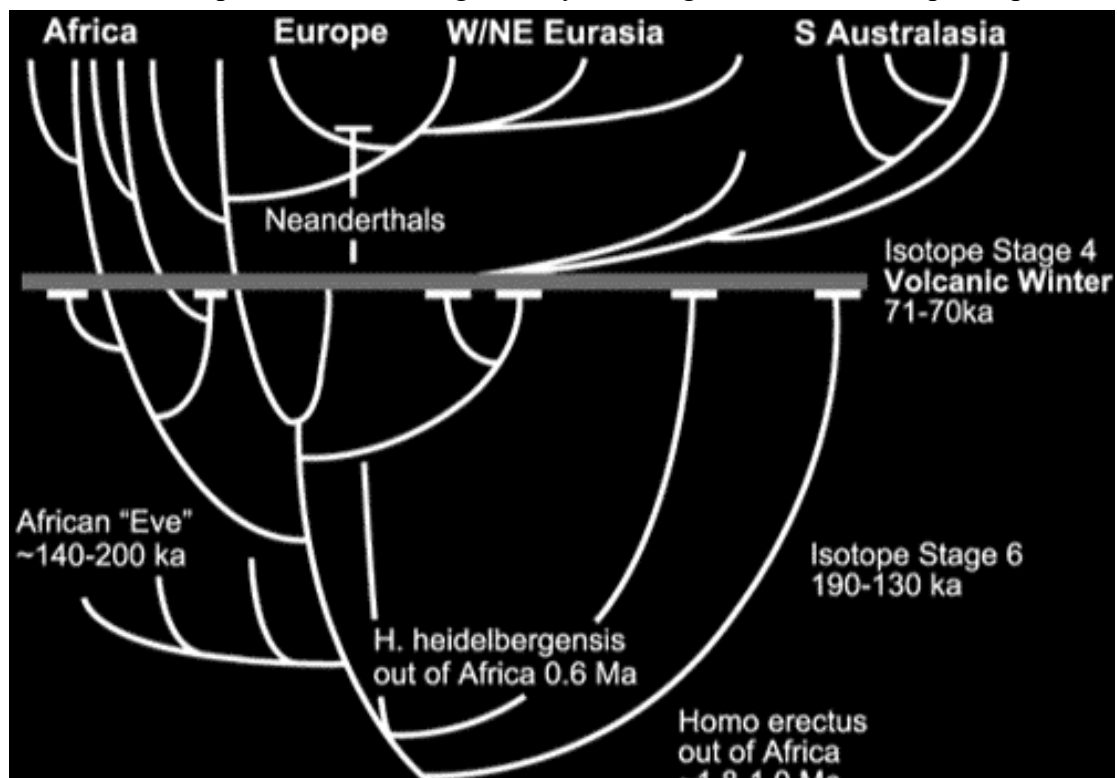
Figure 1.3: The Volcanic Winter/Weak Garden of Eden model proposed by Ambrose.

Greenland GISP2 ice core at 71±5 ka, which they attributed to the YTT eruption. However,
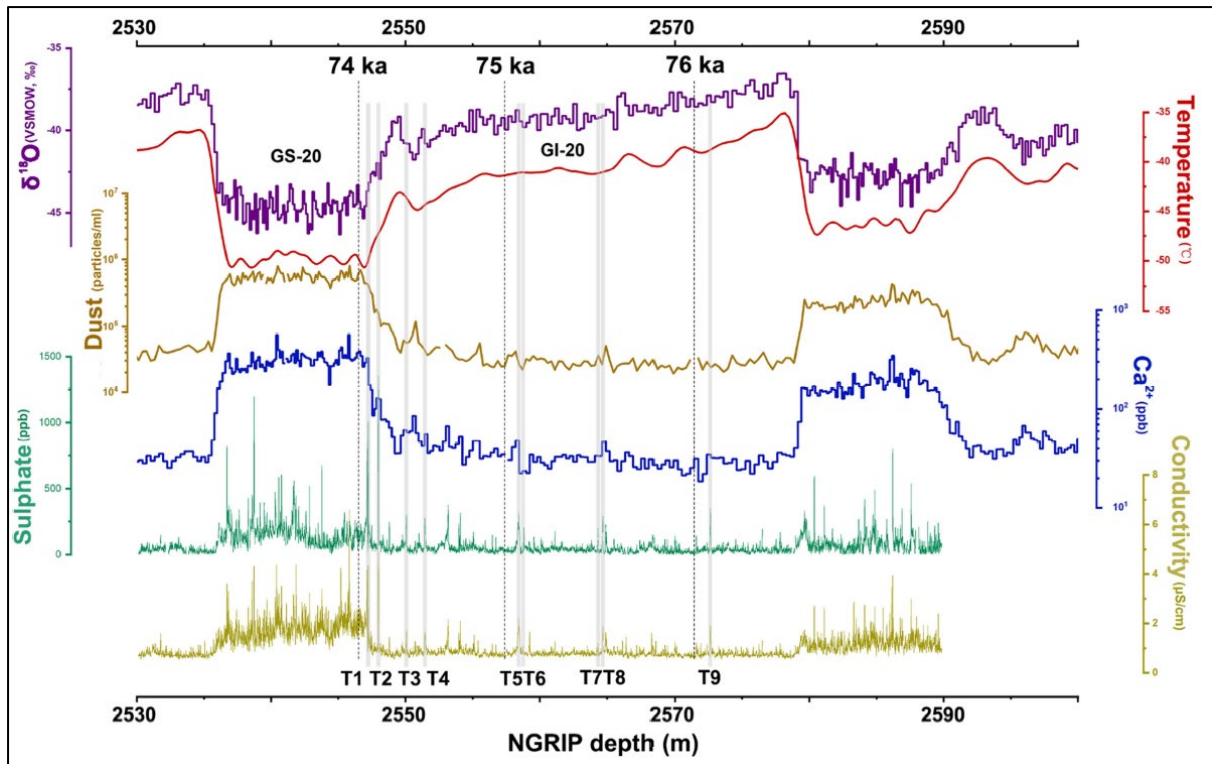
Figure 1.4: NGRIP ice core records around GS-20/GI-20. The dashed lines show ages based on the GICC05modelext time scale (Wolff et al., 2010). The light grey bars (T1-T9) are possible Toba events recognized in bipolar ice cores (Svensson et al., 2013).

these temporal correlation are challenged and argued that YTT eruption occurred after D-O 9 and GI-20S (fig. 1.4)[12].

The model of "Weak Garden of Eden" was highly criticized and defined as a theoretical model which lacks several pieces of evidence. Different scholars have negated it and stated that the association between YTT and previously discussed events are purely circumstantial[12–14,16–18]. Therefore, an alternative and less catastrophic explanation was proposed which explained the reason behind the behavioural shift occurred during the drier environment of MIS 4. Challenging climatic fluctuations might have contributed to the shaping of human habitats which must have triggered rapid dispersal and demographic shift[39]. Although the relationship between these climatic fluctuating and Toba eruption is very poor[12]. Hence, it is proposed that Toba has minimal or no impact on late Pleistocene environment and archaic human populations[12–14,16–18].

Beyond the friction of these bipolar popular notions, many of recent studies have shown diverse environmental impact of ~74 ka Toba eruption[20]. Different marine core data from Bay of Bengal and ice cores from Greenland are analysed for oxygen isotopes. Data suggested that the
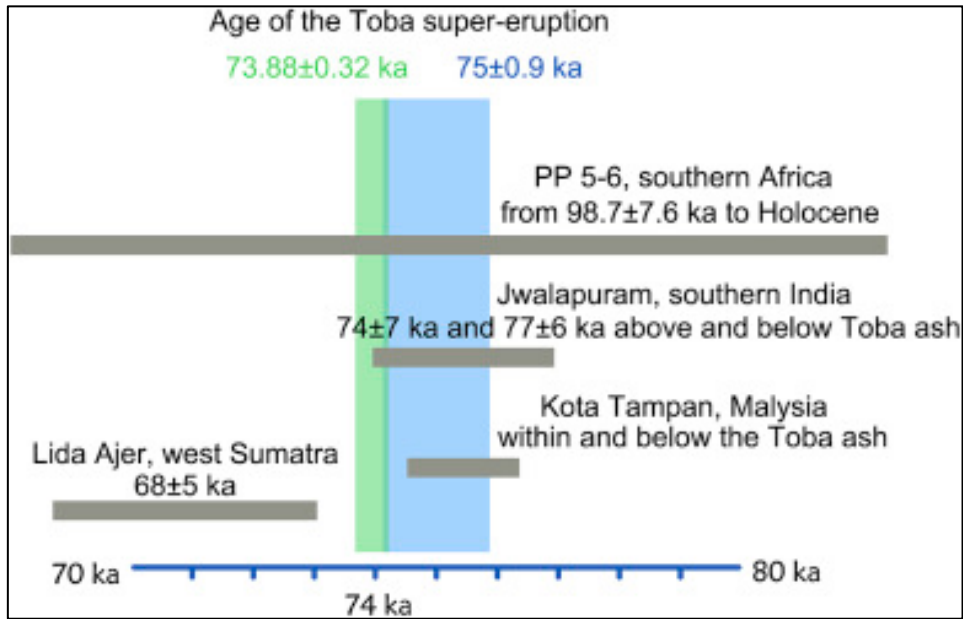
Figure 1.5: Archaeological sites that near Toba volcano or contain the YTT (Ge and Gao, 2020). Illustration shows evidence of human habitation associated with ~74ka Toba eruption. Ge and Gao suggest that the hominin population may have thrived and successfully survived through this catastrophe.

world did cool drastically right after the eruption and that there were several centuries of lower temperatures and reduced precipitation[7].

As far as archaeological record is concern, recent evidence of Dhaba from northern India[25] pointed towards the continued habitation during YTT, showing that the hominins must have thrived through this catastrophe. A similar set of habitational trends are also noticed at Lida Ajer[40] and Kota Tampan[41,42]. Especially the site of Kota Tampan, situated in the closer geographical proximity of Toba caldera shows, that humans may have survived this disaster[12]. Formerly mentioned evidence is also complemented by the faunal record of Late Pleistocene. Louys[43,44] noted that the similarity among the multiple populations of terrestrial mammals in Southeast Asia which lived through Toba catastrophe. Thus, most of humans and animal populations must have survived this hypothesized catastrophe. However, a larger amount of uncertainty surrounds the precise impacts of the Toba eruption on paleoenvironment, and past human populations highlights the need for research that is designed to empirically test this problem.

1.5. Site details

Current investigation is based on the sediment sequence of two quaternary sites i.e., Tejpor and Jwalapuram. Both sites represent different geographical context. Established and dated sedimentary context of both sites allows us to assess the environmental impact in ~74ka Toba

eruption. Main idea is to understand spatial variability in terms of environmental impact of ~74ka Toba eruption.

1.5.1. Jwalapuram

The archaeological site of Jwalapuram is situated in the Jurreru Valley ~11 km west of the modern town of Banganpalle, located in Kurnool district of Andhra Pradesh, India. The archaeological richness of the Jurreru valley and surrounding areas was quickly realized whilst initial stage of KDAP project in 2003[24]. Numerous archaeological localities have now been established, ranging from the Lower Palaeolithic through to Historical periods. Site type found across Jurreru valley is quite variable, varying between painted rock shelters with stratified levels containing pottery and microliths, to open air sites with stone artefact scatters lying on Pleistocene and Holocene surfaces (fig. 1.7). Jwalapuram was excavated by team led by Prof.
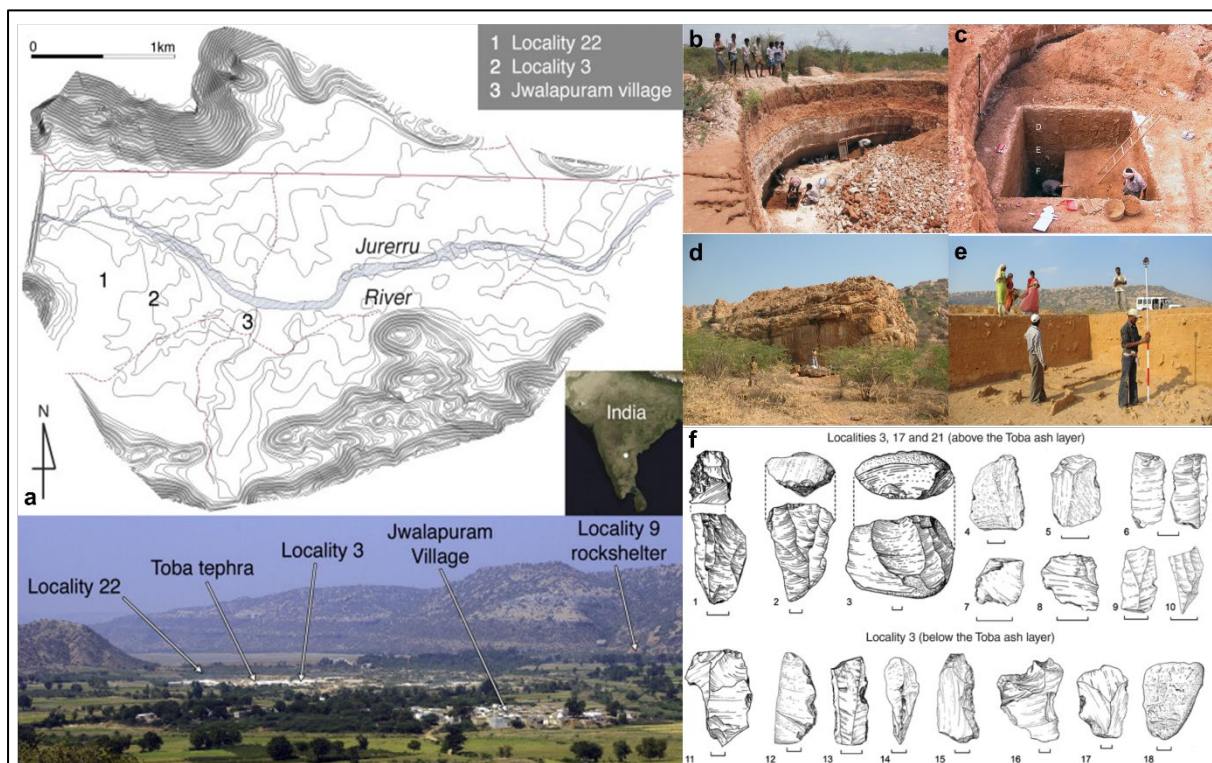
Figure 1.6. Visual overview of Jwalapuram site. a. DEM of Jurreru valley and location of excavated localities in Jwalapuram; b. and c.Jwalapuram locality 3 (current sediment samples are collected from Loc 3); d. Jwalapuram rockshelter; e. Jwalapuram locality 22; f. Pre- and Post-YTT stone tools from Locality 3, Jwalapuram. Image courtesy: Michael Petraglia, Michael Haslam and KDAP.

Michael Petraglia and Prof. Ravi Korisettar in 2003 and 2004. Jurreru valley is famous for its massive Toba ash deposits that has been quarried by detergent industries for more than last three decades (fig. 1.6). Recent quarrying has exposed different sequences of sediment. KDAP projected excavated some of the parts of Jwalapuram with an aim to reconstruct patterns of hominin occupation in the Jurreru valley before and after Toba and therefore, to determine if

the eruption had an impact on populations in the valley and, if so, the extent or severity of this impact[19,23,24]. Project reported and documented 68 archaeological sites in 4.5 km radius of the Jwalapuram.

Different parts of Jurreru lake were excavated in order to expose pre- and post-YTT archaeological horizon. Localities such as 3, 17, 20, 22 & 21 are known for their post-Toba archaeological deposits. Localities like 3 and 22 presents more intact and integrated quaternary sequence showing multiple phases of hominin occupation in the valley at 85ka, 74ka, 71ka, 35ka, 34ka, and 12ka respectively (fig. 1.7). Petraglia and colleague argued based on detailed chronological evidence that hominins were present in the Jurreru River valley, South India, immediately before and after the YTT eruption. Analyses of the archaeological industries recovered from the site indicate a strong element of technological continuity between the pre- and post-Toba assemblages[15,19,45].
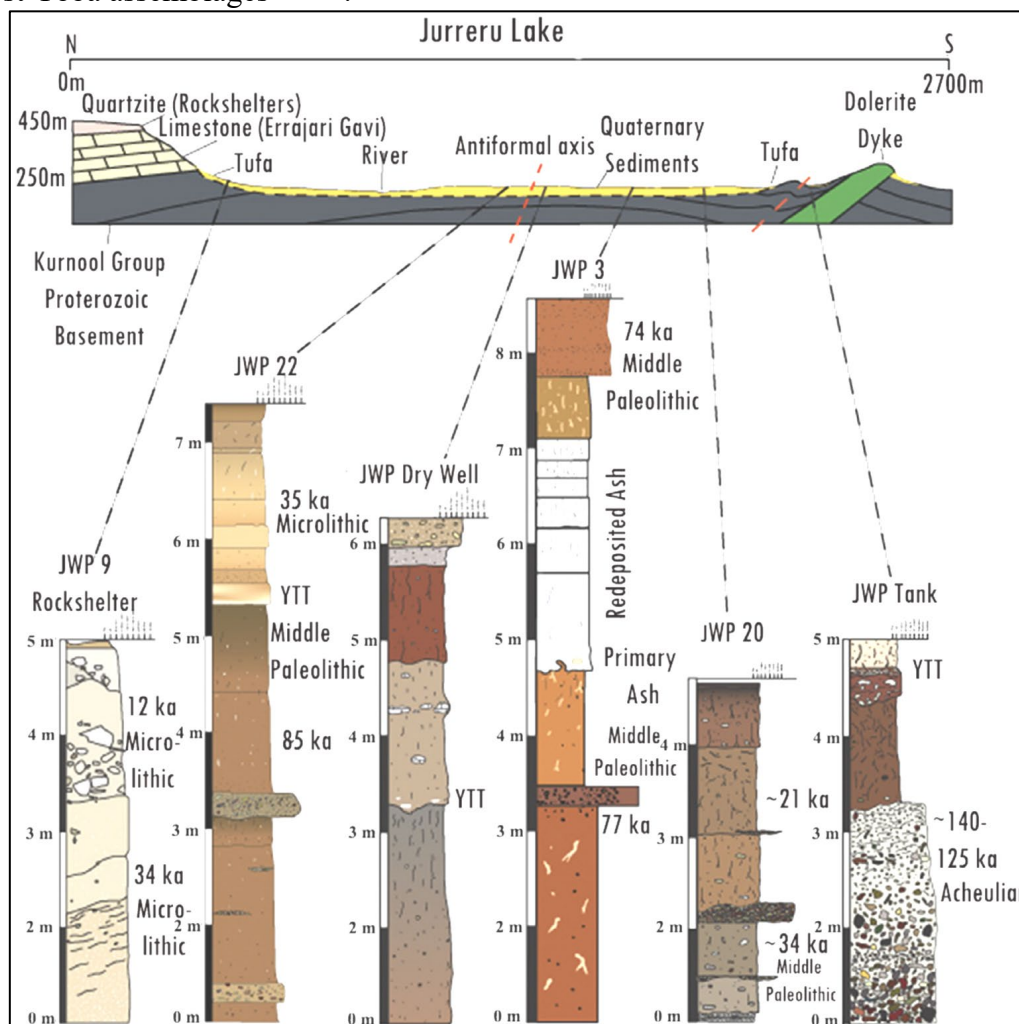
Figure 1.7. Series of valley bottom sedimentary profiles from localities designated JWP9, JWP22, Dry Well, JWP3, JWP20, and JWP Tank from the foot-slopes of Peddakonda to the footslopes of Eddulakonda. The Middle Paleolithic assemblages occur interstratified with the YTT, also constrained by OSL chronology. JWP9 is a rock shelter microlithic site. JWP Tank is an Acheulian site associated with colluvial deposit. Source: The Kurnool District Archaeological Project. See Jones, 2007 for detailed stratigraphic info.

However, Jwalapuram post-Toba sequence had some chronological problem. In 2010, geochronologist Richard Roberts argued that post-Toba dates at Loc. 3 are wrong and they are as young as 55ka[46]. Hence, Jwalapuram investigation is so far unable to solve the question of Toba catastrophe.

Reappraisal

Current instigation solely focusses on pre-YTT and YTT horizon of the Jwalapuram, with an intention to understand the immediate impact of YTT ashfall and probable environmental deterioration. Jwalapuram has 6-fold deposits of young Toba tuff demarcated by 5 greyish hard pans (fig. 1.8). These redeposited YTT layers seems to be a aeolian deposit, deposited at season or annual intervals[23]. Current investigation employs multiproxy approach to understand immediate impact of ~74ka Toba eruption on local environment of Jurreru valley by exploring environmental signatures preserved in re-deposited and primary YTT layers.

1.5.2. Tejpor
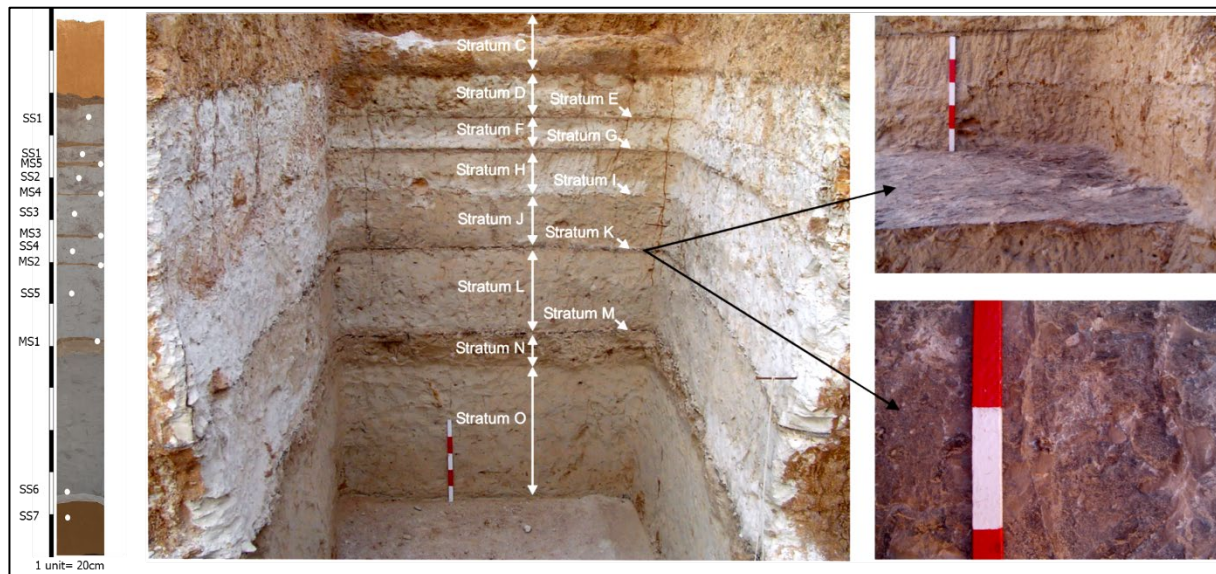
Figure 1.8. Stratigraphic log of Jwalapuram locality 3. Lithostratigraphy shows six to seven-fold of YTT deposits demarcated by six layers of greyish hard pans. SS7: Pre-YTT, SS6-0: redeposited ash stratum and MS1-5: Greyish hard pan stratum. Representative samples are collected from each stratum. Note the brownish-greyish hardpan on the zoomed image.

Tejpor is situated in the lower Narmada valley in Southern Gujarat, India. The S_1 surface of the Madhumati river basin yields 36m long quaternary fluvial sediment succession along the bank (fig. 1.9)[47]. Very thin layer of white volcanic ash is documented at the height of ~7 to 9m. Stratigraphically, ash is sandwiched between silty sand and sandy silt litho units. Geo-chemical and REE signature suggest that the volcanic tuff belongs ~74ka Toba eruption[47]. Pre-Toba, Toba and Toba sediments are later dated by OSL technique[37]. Tejpor YTT is dated back 71±9

ka. Pre-YTT OSL samples collected from 30cm beneath the ash base that gave the date of 74±7 ka. Post-YTT OSL sample is collected from 10cm above the ash layer which yielded the date of 60±6 ka. It is important to notice that post-YTT date of Tejpor has a huge temporal lag suggesting probable sedimentary disconformity. Current investigation is based on the sediments collected from 40cm above and below Toba ash to understand paleoenvironmental trend. Quaternary sequence at Tejpor doesn't yield archaeological deposits. However, region has multiple set of similar middle paleolithic sites that are often associated with Toba ash deposits, although lack of dated middle paleolithic sites makes it impossible to understand their temporal relationship with YTT event.
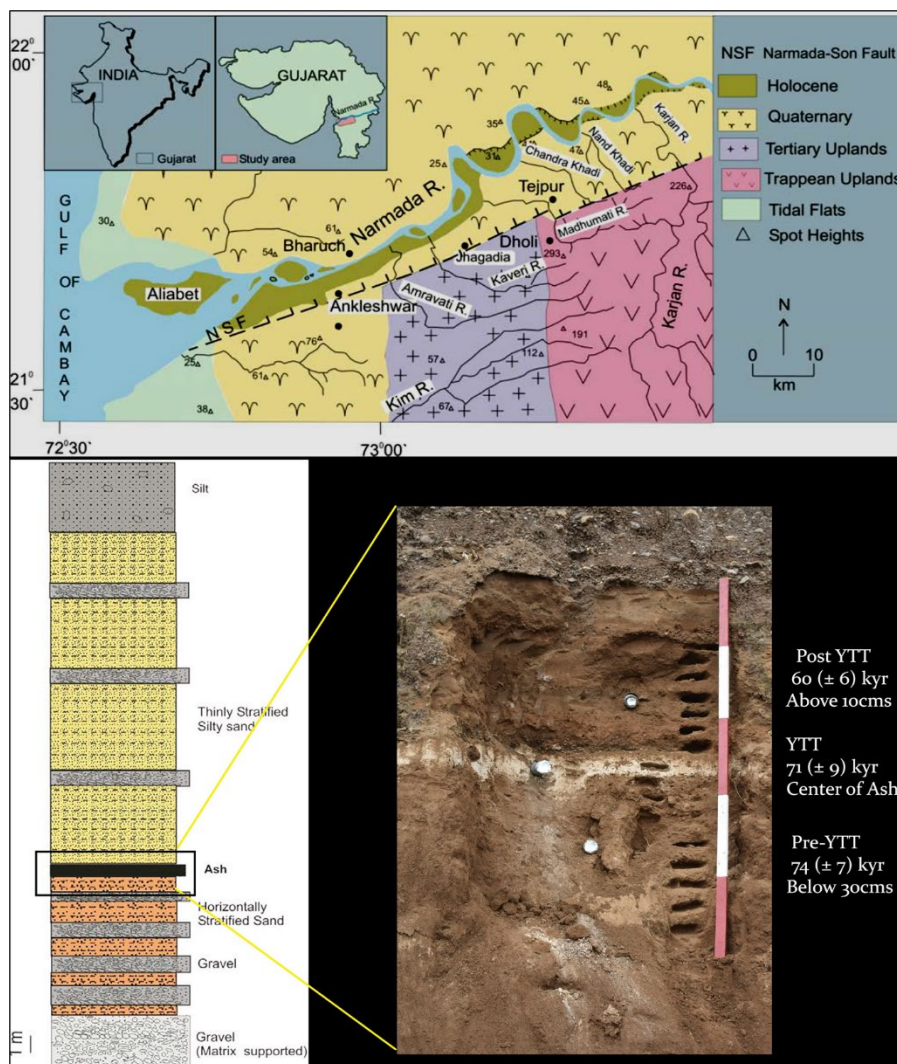
Figure 1.9. Geological location of Tejpor (up) and Litho-stratigraphy of YTT bearing Madhumati section. (Map courtesy: Rachna Raj)

1.6. Paleoenvironmental Proxies

1.6.1. Inorganic paleoenvironmental proxies

Weathering of thermodynamically influenced mineralogical groups in earth sediments is a fundamental aspect of global elemental cycles. Changing trajectory of weathering profiles define the nature of paedogenesis (soil formation) which is directly and indirectly related with different environmental components such as climate, hydrology, atmospheric compositions, etc[48]. Different variety of quantitative tools/indices are used to examine this process by determining past weathering and paedogenesis to re-construct Paleoenvironment and paleoclimatic conditions during the formation of litho/pedo units. Weakening or straightening of paedogenic processes depends on different environmental processes like-precipitation, temperature, topography, etc [48,49]. It is extremely crucial to determine the responsible factors behind weathering and disintegration of existing minerals (soil as well as rock) to understand that what environmental processes have contributed to the soil formation process. For an instance, climate induced alteration in clay minerals is extensively reviewed in various studies[49]. Chemical alteration in clay mineral is directly correlated with climatic conditions, factors like – temperature and soil humidity determine the nature and intensity of chemical weathering in soils. Earlier works has suggested that the clay minerals follow certain weathering pattern as the hot-humid climate shifts to cool and dry (weathering order in clays: kaolinite-smectite-vermiculite-chlorite-illite-mica)[48–5152]. Certain geochemical transitions can be inferred by elemental and mineralogical assessment, and they can help to understand past paedogenesis and their paleoenvironmental context. Current study put emphasis on inorganic environmental proxies based on elemental and mineralogical composition of sediment (fossil soils) to answer the question of Toba catastrophe. Super eruption such like ~74 ka Toba are thought to have created havoc and disrupted global climatic cycle [21,53]. These climatic disruptions must have had some impact of sedimentary and paleopedological environment. These inorganic proxies (i.e., weathering indices, major element ratios and mineralogical transitions) will not only explain the impact of such massive event but it will unveil the story of resurgence in post-event phase.

Major element ratios, weathering indices and paedogenic processes

Primary rock-forming elements are often referred as "major elements", such as Ca, Fe, K, Mg, Na, Al, Si, Mn, P, Ti [49,50,52]. Among these Ca, Mg, Na, K, Mn, and P are considered as base elements that are susceptible to weathering. Remarkable degree of mobility is noticed among

base elements due to increasing weathering. On contrary, other major elements like- Al, Si, Fe, Mn, Ti are immobile and resistant to chemical alteration. These elemental ratios are widely used to explain different paedogenic processes (Table 1.1.), such as – hydrolysis, leaching, acidification, and salinization. Most of these processes are climate sensitive and very well reflected in weathering profiles.

Apart from major element ratios, different chemical weathering and alteration indices are used to understand the intensity of weathering and the role of climatic stress in paedogenic processes[54]. Different weather indices focus on mobility of different major and minor elements, and how different compounds or mineralogical group goes through chemical transformations due to their mobility[49,50,52]. Due to harsh weathering, silicate minerals (tephra in this study) disintegrate, and silica is partially leached resulting into the deposition of residual sesquioxides, and formation of new sesquioxides as well. These relative variations of various elements can be used to understand the intensity of chemical weathering/alteration and act as important paleoenvironmental proxies[51]. Table 1.2 explains the basic principle and application of weathering indices.

Table.1.1. Molecular weathering and pedogenesis ratios (Sheldon and Tabor, 2009).

Molecular weathering and Paedogenic ratios		
Ratio	Formula	Pedogenic process
Bases/Al	*ΣBases/Al	Hydrolysis
Base Loss	Base/Ti	Leaching
Clayeyness	Al/Si	Hydrolysis
Provenance	Ti/Al	Acidification
Salinization	(K+Na)/Al	Salinization
Leaching	Ba/Sr	Leaching/Hydrolysis

*ΣBase=K+Na+Ca+Mg

Table 1.2.: Summary of weathering indices. >50 values in CIA, CIW and PIA represent early weathering products (Price and Velbel, 2003).

Weathering Indices				
Indices	Formula	Optimum Fresh Value	Optimum weathered value	Trend (Increase in weathering)
Silicon/Aluminium (Sa) and Silicon/ Aluminium +Iron (Saf)	Silicon/Ai & Silicon/Ai+Fe	0	-	Positive
Ruxton Index	SiO_2/Al_2O_3	>10	0	Reducing
Weathering Index of Parker	$(100)[(2Na_2O/0.35)+(MgO/0.9)+(2K_2O/0.25)+(CaO/0.7)]$	>100	0	Reducing
Vogt's Index	$(Al_2O_3+K_2O)/(MgO+CaO+Na_2O)$	<1	Infinite	Positive
Chemical Index of Alteration	$(100)[Al_2O_3/(Al_2O_3+CaO+Na_2O+K_2O)$	≤ 50	100	Positive
Chemical Index of Weathering	$(100)[Al_2O_3/(Al_2O_3+CaO+Na_2O)$	≤ 50	100	Positive
Plagioclase Index of Alteration	$(100)[Al_2O_3-K_2O /(Al_2O_3+CaO+Na_2O-K_2O)$	≤ 50	100	Positive

These weather indices and major elemental ratios are further complimented by mineralogical data, showing change in nature of mineralogical groups/compounds in soil. Chemical alteration can also lead to the changes in the crystallinity of mineral groups/compounds, resulting into phase transition due to changing thermal dynamics. Several studies have explained phase transition within phyllosilicates and transformation of feldspar into clay due to paleoweathering, which is certainly induces by paleoclimatic fluctuation. However, many of these weathering indices, major elemental ratios and other inorganic paleoenvironmental proxies has certain limitations. Nevertheless, clumping elemental and mineralogical paleoenvironmental proxies can provide a holistic image of past environment and climatic conditions.

1.6.2. Organic Proxies

Diverse range of organic geochemical biomarkers are widely used to understand past environmental dynamics. These biomarkers are organic compounds coming from specific biological origins[55,56]. They can be used for chemotaxonomy; hence they are known as biological markers[56]. These biomarkers can be originated from various lifeforms, ranging from

archaea, bacteria to whole kingdom of animal and plants. Often these markers are well preserved in the sedimentary archive, and various proxies based on these "fossilized organic compounds" extracted from geological archives have been enabled us to understand, assess and reconstruct wide array of paleoenvironmental and paleoclimatic conditions, throwing light on the key factors like past temperature, vegetation, and hydroclimate.

Leaf-wax biomarker and paleovegetation

Plant wax biomarkers are lipid markers that are highly refractory and idly preserved in aquatic settings[57]. These waxy part of the cuticular layer of the leaf which act as a barrier or a shield between soft plant tissues and challenging environmental factors, protecting the plant from severe water loss, diverse range of disease, and ultraviolet radiation[58] (fig. 1.10). These leaf-waxes produces specific biological marker called *n*-alkyl lipids which are used as an innovative proxy for reconstructing past floral composition and structure, temperature, rainfall intensity, and other environmental processes[59]. Leaf-wax biomarkers are commonly used in earth and climate sciences and recently incorporated and contextualized in archaeology and paleoanthropology to answer crucial questions regarding past human-environment interactions and revealing multiple facets of human origins. It is generating intriguing and significant information explaining paleoecological context in which Homo and its closest relatives evolved, adapted, and invented different behavioural signatures such as stone tool, fire, etc. [59].

n-alkyl lipids are comprised of *n*-alkanes, *n*-alkanols, *n*-alkanoic acids, and wax esters, produced by the vascular plants of terrestrial as well as aquatic regime[59]. Generally, numbers of carbon atoms in these lipid compounds are considered as a fingerprint of the source[55]. Long-chain *n*-alkyl lipids ore one of the most significant compounds, exhibiting a strong predominance of odd over even number of carbon atoms in a chain (*n*-alkanes) or even over odd carbon number chain length predominance (*n*-alkanoic acids)[60]. These compounds can be divided into three categories based on their chain length, i.e., short, mid and long-chain compounds.

The long carbon chain lengths are predominant in terrestrial higher plants (C_{29}-C_{35} for *n*-alkanes and C_{28}-C_{34} in *n*-alcohols and *n*-alkanoic acids): mid-chain length homologues such as C_{23}-C_{27} (*n*-alkanes) and C_{24}-C_{26} (*n*-alkanoic acids), are mostly contributed by aquatic macrophytes but they are also produced by terrestrial higher plants in smaller quantities, shorter chain lengths (C_{17}-C_{21} for *n*-alkanes and C_{16}-C_{22} in *n*-alkanoic acids) are often coming from sources such as aquatic algae and microbes[59–61]. Difference in the proportion of short,

mid and long-chain *n*-alkyl compounds can be used as an important tool to determine the nature past vegetation and infer to paleoenvironmental conditions[57,62]. Current investigation particularly focusses of *n*-Alkane distribution to assess the paleoenvironmental context of per and post Toba environment at Tejpor and Jwalapuram.
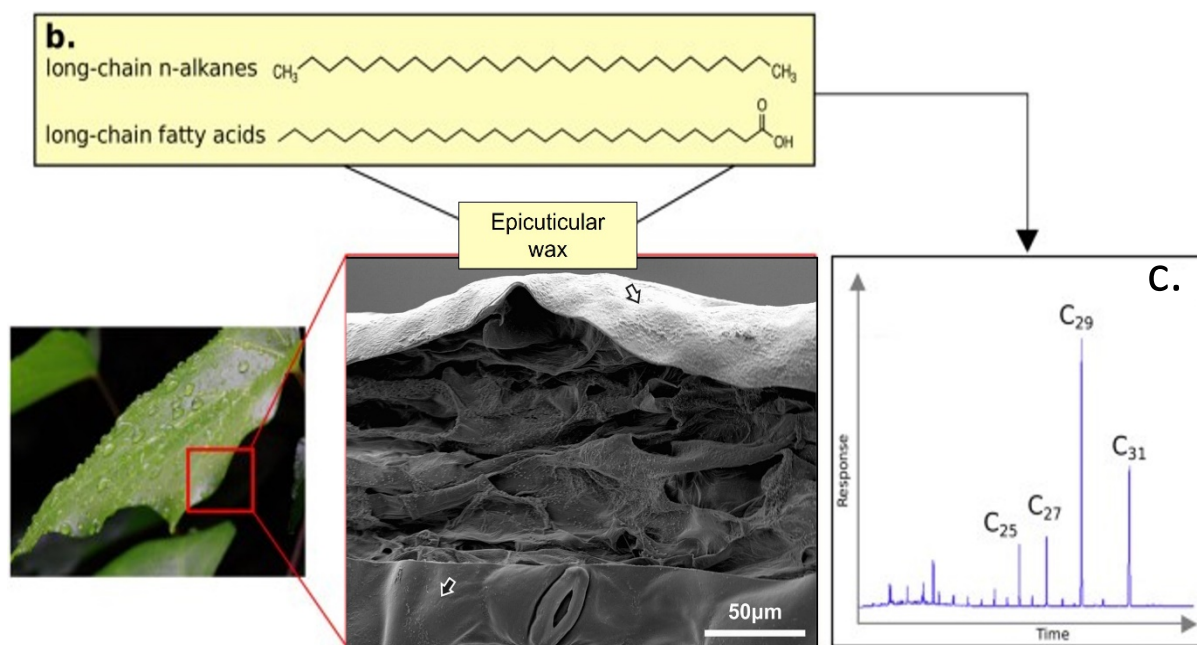
Fig.1.10. a. Micrograph of leaf cross section, arrow pointing towards upper epidermis covered by a cuticular membrane with epicuticular wax deposits on its outer surface. b. long chain *n*-alkanes and fatty acids, ubiquitous compounds in leaf waxes from terrestrial higher plants; and (c) typical chromatogram of leaf wax *n*-alkanes from terrestrial higher plants showing the distribution of long-chain homologues (Courtesy: Patalano et. al. 2021; Eley and Hren 2018).

n-Alkane distribution and past plantscape

Most of the compound types within *n*-alkyl lipids have similar chemical composition. However, abundance and distribution of these compounds may vary due to environmental conditions[57]. Ratios based on *n*-alkane homologues can be used to understand the environmental dynamics and proportional differentiation between contribution of different floral communities into the lipid pool[56]. Different methods for determining source apportionment of *n*-alkanes are described below.

Carbon preference index (CPI)

CPI is commonly used as measure to understand odd/even carbon number predominance as it allows to differentiate between biogenic and anthropogenic source of hydrocarbons. CPI values can be calculated by a different method focused on different categories of homologues. Current study used the following formula:

$$CPI = \frac{2\Sigma C_i}{\Sigma C_{i-1} + \Sigma C_{i+1}}$$

Bray and Evans devised the CPI ratio as a numerical representation, where. i and C represents odd numbered n-alkane homologues and its relative concentration, respectively[63]. The CPI ratio can be used to access the biological source and how much of the original biomarker is preserved in sediments as a way of quantifying OM maturity. Any fluctuation in factors like sedimentation rates and degree of lake water oxygenation cause severe impact on the preservation of these biomarkers. Usually, CPI are calculated by using the relative concentration of C_{12}-C_{35} n-alkanes. If CPI (C_{12}-C_{35}) value are greater than 1 then it indicates predominance of odd over even carbon numbered n-alkanes. CPI values less than 1 characterizes the predominance of even numbered alkanes which indicate that the greater source of alkanes is coming from aquatic material such as algae and bacteria. CPI value of C_{23}-C_{35} indicates the contribution of terrestrial plant waxes. CPI (C_{23}-C_{35}) values are greater than 1 suggest terrestrial plants are the greater source of n-alkanes.

Average chain length (ACL)

The main function of epicuticular waxes is save plant from environmental stressors and causes of desiccation. Plants tend to adapt the chain lengths of lipid components in their waxy layer in response to fluctuation in environmental factors such as temperature and moisture availability[57,60,64]. The ACL value is derived from the concentration-weighted mean of the respective long chain compounds[61], and due to land plants biosynthesizing long chain compounds in warmer (and drier) climates, can be used to infer changes in paleoclimate. Longer ACL value of leaf wax layers suggest hotter and drier conditions and shorter ACL reflect cooler and wetter condition respectively. ACL values are calculated by following formula:

$$ACL = (23 \times C_{23} + 25 \times C_{25} + 27 \times C_{27} + 29 \times C_{29} + 31 \times C_{31} + 33 \times C_{33})/(C_{23} + C_{25} + C_{27} + C_{29} + C_{31} + C_{33}).$$

Aquatic plant *n*-alkane proxy (Paq)

Paq. indice is based on the distinctive differences in *n*-alkane chain lengths prevalent in submerged macrophytes (C_{23} and C_{25}) vs higher terrestrial plant matter (C_{29}, C_{27} and C_{31}) to reconstruct the relative proportions of the i*n*-situ plant assemblages in response to environmental changes different lacustrine bodies. Paq is also used to reconstruct moisture availability in terrestrial conditions (lakes in particular).

$$P_{aq.} = (C_{23} + C_{25})/ (C_{23} + C_{25} + C_{29} + C_{31})$$

Terrestrial plant *n*-alkane proxy (Pwax)

Pwax. indice is also based on same premise of characteristic carbon chain length distribution between aquatic (submerged macrophytes) versus terrestrial plants. Pwax proxy is used to measure relative proportions of emergent and terrestrial plant inputs in relation to all higher plants to reconstruct the paleoprecipitation and paleovegetation[64].

$$P_{wax} = (C_{27} + C_{29} + C_{31})/ (C_{23} + C_{25} + C_{27} + C_{29} + C_{31})$$

Terrigenous Aquatic Ratio (TAR)

Predominance of the *n*-alkanes C_{27}, C_{29} and C_{31} is characteristic of terrestrial higher plants whereas the predominance of *n*-alkanes C_{15}, C_{17} and C_{19} indicates aquatic source[57,64,65]. Hence, the terrigenous aquatic ratio is useful for evaluating whether the main source of *n*-alkanes is terrestrial or aquatic. TAR values lesser than 1 indicates the aquatic source and TAR values greater than 1 suggest terrestrial source[66].

$$TAR = (C_{27} + C_{29} + C_{31})/ (C_{15} + C_{17} + C_{19})$$

.

Chapter II

Material and methods

2.1. Sampling

Two set of sediment samples are collected from Tejpor and Jwalapuram respectively. In case of Tejpor, total 80cm of sediment was sequenced at the interval of 5cm (fig. 2.1.), covering pre-Toba and post-Toba sediments. On the other side, representative samples are collected from each stratum of Jwalapuram sediment sequence (fig. 2.2). All samples are untouched and collected in aluminium foil containers. Collected samples are opened in the HERCULES lab and dried in the Memmart oven at 40°C for overnight. Dried samples are further grinded, powdered and homogenized in the agate mortar. Agate mortar and pestle are episodically cleaned with acetone and sand after homogenization of each sample, to avoid inter-sample contamination. Homogenized samples are stored in glass vials for further analysis.
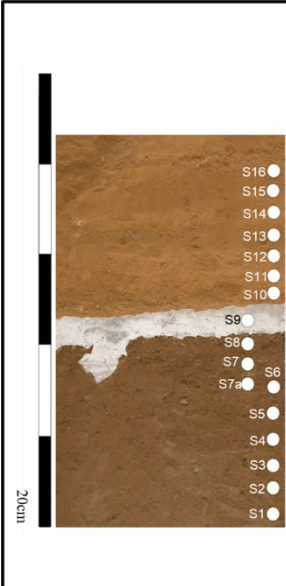
Figure 2.1: Sample information for Jwalapuram. All the results are plotted as per normalized depth model.

Sample Name	Sample Detail	Depth from Surface (cm)	Normalized Depth (cm)
SSO	Redeposited Toba ash	50	212
SS1	Redeposited Toba ash	80	200
MS5	Greyish Hardpan	85	195
SS2	Redeposited Toba ash	92	188
MS4	Greyish Hardpan	100	180
SS3	Redeposited Toba ash	112	168
MS3	Greyish Hardpan	123	157
SS4	Redeposited Toba ash	133	147
MS2	Greyish Hardpan	140	140
SS5	Redeposited Toba ash	155	125
MS1	Greyish Hardpan	180	100
SS6	Primary Toba ash	260	20
SS7	Pre-Toba Sediment	280	0

2.2. Analytical framework

Current investigation employs an array of analytical techniques to explore and reconstruct paleoenvironmental conditions. Whole analytical framework is divided into three parts:

Figure 2.2: Sample information for Tejpor. All the results are plotted as per normalized depth model. Multiple YTT samples are collected laterally (belong to same depth).

	Sample Name	Sample Detail	Depth from YTT layer (cm)	Normalized Depth (cm)
	S16	Post-YTT	35	75
	S15	Post-YTT	30	70
	S14	Post-YTT	25	65
	S13	Post-YTT	20	60
	S12	Post-YTT	15	55
	S11	Post-YTT	10	50
	S10	Post-YTT	5	45
	S9, T1, EA1, EA2, EA3	YTT	0	40
	S8	Pre-YTT	-5	35
	S7	Pre-YTT	-10	30
	S6	Pre-YTT	-15	25
	S5	Pre-YTT	-20	20
	S4	Pre-YTT	-25	15
	S3	Pre-YTT	-30	10
	S2	Pre-YTT	-35	5
	S1	Pre-YTT	-40	0

screening, inorganic proxies, and organic proxies. Coming to the core part of analytical framework, different inorganic proxies are produced based on mineralogical and elemental data using XRD and ED-XRF technique. Organic proxies are central focus of the current investigation. These proxies are based on leaf-wax biomarker data processed by GC-MS.

2.2.1. Sediment screening

a. As we are dealing with fossilized soil, it is quite crucial to screen the samples to understand its suitability for stable isotopes and leaf-wax biomarker analysis. Different techniques are used for screening purposes such as general microscopy, SEM-EDS, Micro-CT, and FTIR.

b. Attenuated Total Reflection (ATR) – Fourier Transform Infrared spectroscopy
   Homogenized sediments samples are screened under ATR-FTIR in order assess the suitability of soil samples for biomarker and stable isotope analysis. Multiple IR spectra are produced using Bruker ALPHA FTIR spectrometer. 1 spoon (~0.2 g) of homogenized sample is placed over ATR crystal plate. The results were acquired in absorption mode. Spectra were collected using OPUS 7.2 software with spectral resolution of 4 cm^{-1} and 32 scans. Produced IR spectra are corrected using extended ATR correction in OPUS program. Further, baseline correction and normalization are also done. Exported IR data is processed in Microsoft Excel and ORIGIN software where diagnostic IR peaks (like: CO_3) are statistically quantified using gaussian corelations.

c. General microscopy

Representative soil sample are screened under Stereo zoom microscope LEICA M205C and Hirox digital microscope (HRX-01).

d. Scanning Electron Microscopy (SEM) – Energy Dispersive X-ray Spectroscopy (EDS)

Representative samples from both sites are selected from SEM screening (mostly using SE imaging). The analysis of the soil samples was performed by variable pressure scanning electron microscopy (Hitachi S3700N) coupled with energy dispersive X-ray spectrometry (BRUKER Xflash 5010SDD). The samples were analysed at an accelerating voltage of 20 kV and at low vacuum (40 Pa). The images were acquired in the secondary electron mode.

Samples are placed on the carbo*n*-tape coated sample holder. Some of the samples are sputtered by gold to create conductive surface. Samples are sputtered using 25 mA sputter current for 120 secs. in Q150R Plus – Rotary Pumped Coater. Some of the u*n*-sputtered samples are also analysed for elemental characterization under EDS. Multiple spot/point (single as well as multiple), line and elemental mapping are done. The operating conditions for EDS analysis were as follows: backscattering mode (BSEM), 20 kV accelerating voltage, 10 mm working distance, 100 μA emission current and 40Pa pressure in the chamber.

e. Micro-Computed Tomography (CT)

Micro-CT analysis was conducted on some of the fossilized root-cast and hardpan fragments from Jwalapuram. X-ray microcomputed tomography (micro-CT) was used to assess the three-dimensional (3D) internal microstructure and compositional heterogeneities of soil samples. Digital radiographs were acquired with a micro-CT SkyScan 1172 scanner (Bruker, Billerica, MA, USA) using an X-ray cone incident on a rotating specimen. Micro-CT analysis was facilitated by CERENA lab, Uni. de Lisboa, Lisbon.

2.2.2. Paleoenvironmental proxies

a. X-ray Diffraction (XRD)

X-ray Diffraction (XRD) is employed for mineralogical characterization, determining impact of paleopedological processes on the crystalline structure of different mineralogical compounds that is manifested in terms of phase transitions. 29 finely powdered samples are assessed by pXRD (powder X-ray diffraction) using Bruker

AXS D8 Discover XRD with the Da Vinci design. A Cu Kα source operating at 40 kV and 40 mA and a Lynxeye 1-dimensional detector were used. Scans were run from 3 to 75 ° 2θ, with 0.05 2θ step and 1s/step measuring time by point. 8 samples are re-assessed for finer compound segregation. These samples were run at 14 sec per step with 0.02 degrees increment. Diffract-EVA software with PDF-2 mineralogical database (International Centre for Diffraction Data - ICDD) was utilized to interpret XRD patterns. Origin and R programming software is further used for visualization purposes.

b. Benchtop X-Ray Florescence (XRF)

XRF analysis is used for elemental characterization of sediment. Analyses were performed operating an Energy Dispersive X-Ray Spectrometer (EDS-XRF) Bruker S2 Puma. Current investigation adopted a methodology suggested by Georgiou[67]. Samples were fused on a Claisse LeNeo using a flux (Li-tetraborate): sample of 10:1 to form fused beads. ratio current study using ignited samples instead of raw samples which may have produced errors in current dataset.

However,quantifications were obtained using a regression method with 19 standard reference materials (SRM) namely GSP-2, SBC-1, BCR-2, BHVO-2, BIR-1A, DTS-2B, SGR-1B, SDC-1, QLO-1, AVG-2, COQ-1, W2A (USGS SRM), SARM-52 (MINTEK SRM), STSD-3 (Natural Resource Canada SRM), SXO7-10 (LGC SRM), DC 60105, DC 73020, DC 61101, DC 62108c, DC 73309 (NCS SRM). Samples were also reassessed with standard less method using SMART oxide module. Main intention was to understand the quantitative difference between both methods in order to determine the nature of systematic error. The loss of ignition was evaluated by calcination (on crucibles) of roughly 1g of dry sample in a muffle furnace for 1 hour at 1050 °C. LOI allows us to quantify the loss occurred during the formation of fused beads.

The Spectra Elements 2. software was utilized for acquisition and data processing, reporting the final oxides/elements concentration and the instrumental statistical error associated. XRF elemental data is used for paleopedological analysis. Current XRF dataset has certain errors due to issues related to sample preparation protocol as earlier mentioned. Although current dataset can be used to assess elemental trends. Thus, different pedogenic ratios, chemical weathering and alteration indices were calculated using elementary data. Current paleopedological analysis contextualizes the mosaic of

methods proposed by Sheldon[49], Babechuk[48], Price[52] and Harnois[50]. It is very important that current data should be revised as per the analysis of raw sediment samples.

c. Gas Chromatography – Mass Spectrometry

Two set of three samples (pre-YTT, YTT and post-YTT) are selected for leaf-wax biomarker analysis. Free lipids were obtained from sample aliquots with a Dionex ASE 100 accelerated solvent extractor using dichloromethane (DCM) and methanol (MeOH; 9:1)[68]. 4 g of homogenized sample is mixed with 4g of diatomic sand, filled in the extraction cell (34 ml). ASE set-up is cleansed for 15 mins at 23° C prior to extraction. It was single extraction event using continuous extraction method. Extraction is done through 3 static cycles where duration of each cycle is around 5 mins. Sample are extracted at 1500 psi and 100° C[68]. Average 71 ml of solvent is used for each extraction. Extracted lipid is further evaporated in Buchi R-210 Rotavapor-Evaporators. Concentrated lipid extract is mixed with 20 μL of hexane and 2 μL of Tetratriacontane (C34 as an internal standard). Lipid mixture is vortexed in VWR vortex mixture. *n*-Alkanes (leaf-wax) are separated from prepared lipids, using Shimadzu GC-2010 PlusR gas chromatograph equipped with a ZebronR ZB-5HT InfernoTM column (15 m. x 0.25 mm i.d; 0.25 m. film thickness) and coupled with a Shimadzu QP2010 mass spectrometer was used to analyse the samples. The samples were injected in a splitless mode with a sampling time of 1 minute. Helium was used as the carrier gas and the operating conditions were as follows: The furnace was initially set at 50° C for 2 minutes. Then it was ramped up to 300° C at a rate of 10° C/min. The furnace temperature was held at 300° C for 5 minutes after which it was raised to 400° C at a rate of 10° C/min. It was again held at 400° C for 5 minutes. The detector voltage of the mass spectrometer was set automatically relative to the tuning result of the specific day by the equipment. The scanning range was set between m/z values of 40 and 1090. The data from the GCM was exported in .cdf format and processed in AMDIS software. The retention times of the observed peaks were identified using NIST[TM] database. Mass chromatograms of m/z values of 85 (*n*-alkanes) are exported and plotted using Microsoft excel and Origin. Area of base peak of each *n*-alkane molecule is documented and normalized against the base peak area of internal standard (C34). Normalized data is further used for OM source characterization using different indices such as – CPI, ACL, TAR, $P_{aq.}$ $P_{wax.}$

Chapter III

Results and discussion

3.1. Sediment screening

Sediment samples are screened for determining following things, such as – availability of organic matter, micro-structures, compositional characterization etc. Different technique such as stereo microscopy, SEM-EDS, Micro-CT, ATR-FTIR, stereo microscopy.

3.1.1. Incipient weathering of YTT
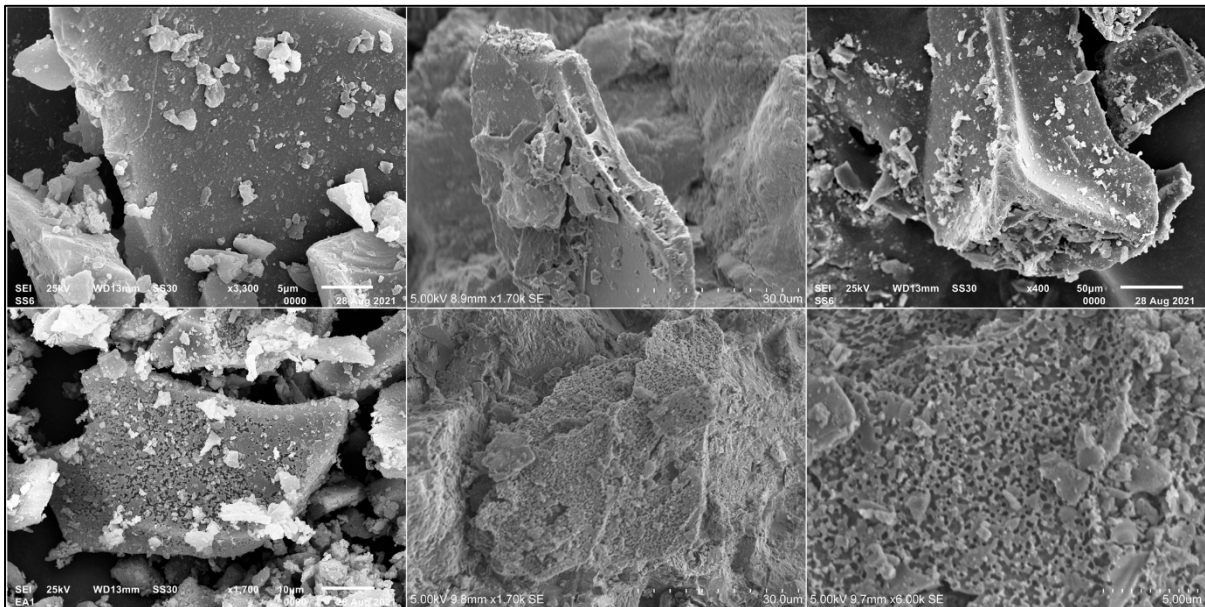
Figure 3.1: SEM (secondary electron) micrographs of YTT glass shards from Jwalapuram (top) and Tejpur (bottom). Note the distinctive difference in the surface morphology of YTT glass shards from both sites. Jwalapuram YTT shards are fresh, showing minimal degree of structural alteration. In contrast, Tejpur glass shards are desiccated and highly weathered. Higher degree of weathering of glass may be an indicator of arid climatic conditions suggesting the local environment at Tejpur may have get drier and cooler immediately after Toba event.

SEM-EDS of Toba ash from Jwalapuram and Tejpor showed some interesting structural features. Surface morphology of glass shards in Jwalapuram ash samples are structurally intact and less weathered (fig. 3.1). Minimal physical alteration of Toba ash at Jwalapuram also compliments the fact that the YTT was deposited in aquatic-marshy environment[69]. In contrast, surface morphology of Tejpur ash is highly deteriorated showing signatures of heavy desiccation and massive weathering. The desiccation of glass shards seems to be a signature of weathering probably occurred due to severe aridity[70,71].

3.1.2. Assessment of black stains in Jwalapuram sample: possible indicator of microbial activity

Apart from incipient weathering of glass shards, SEM-EDS analysis also helped to understand the signatures of microbial activity in Jwalapuram samples (particular in MS samples). Earlier Jones *et al.* suggested that hard-pan stratum (MS samples) of Jwalapuram yielded prominent signature of microbial activity highlighted by black specks (fig. 3.2).

Figure 3.2: Stratum E (equivalent to MS5) at Jwalapuram. (a) North face of excavated trench indicating the position of stratum E. (b) The surface of stratum E in plan view. (c) Multiple very fine traces are visible; these are paler in colour than the dark grey surface of stratum E. (d) A close-up image of the possible rootlet traces in (c). (e) Patches of black specks are visible on the surface of stratum E. These may represent manganese or iron staining, or they may represent the traces of microbial growth. Image courtesy: Sacha Jones
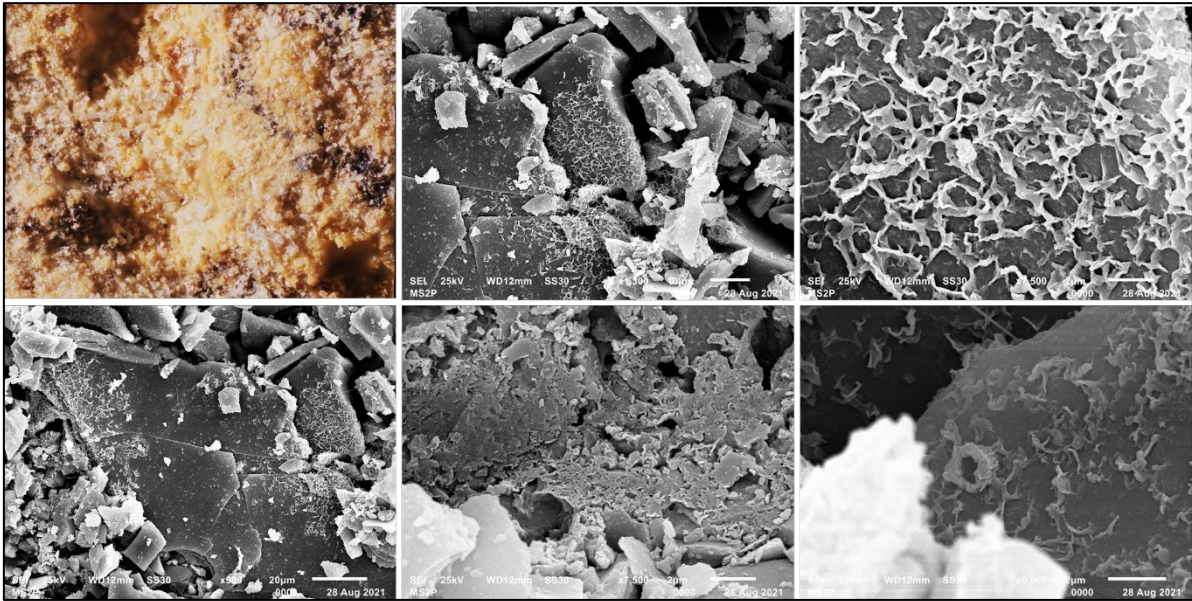
Figure 3.3: Zoomed image and micrograph of black specks on MS1 sample from Jwalapuram. These black stains are embedded in silica matrix of glass. Morphologically, it looks like a biofilm that has dendritic structure. In many cases, these films have led to disintegration of glass surfaces.
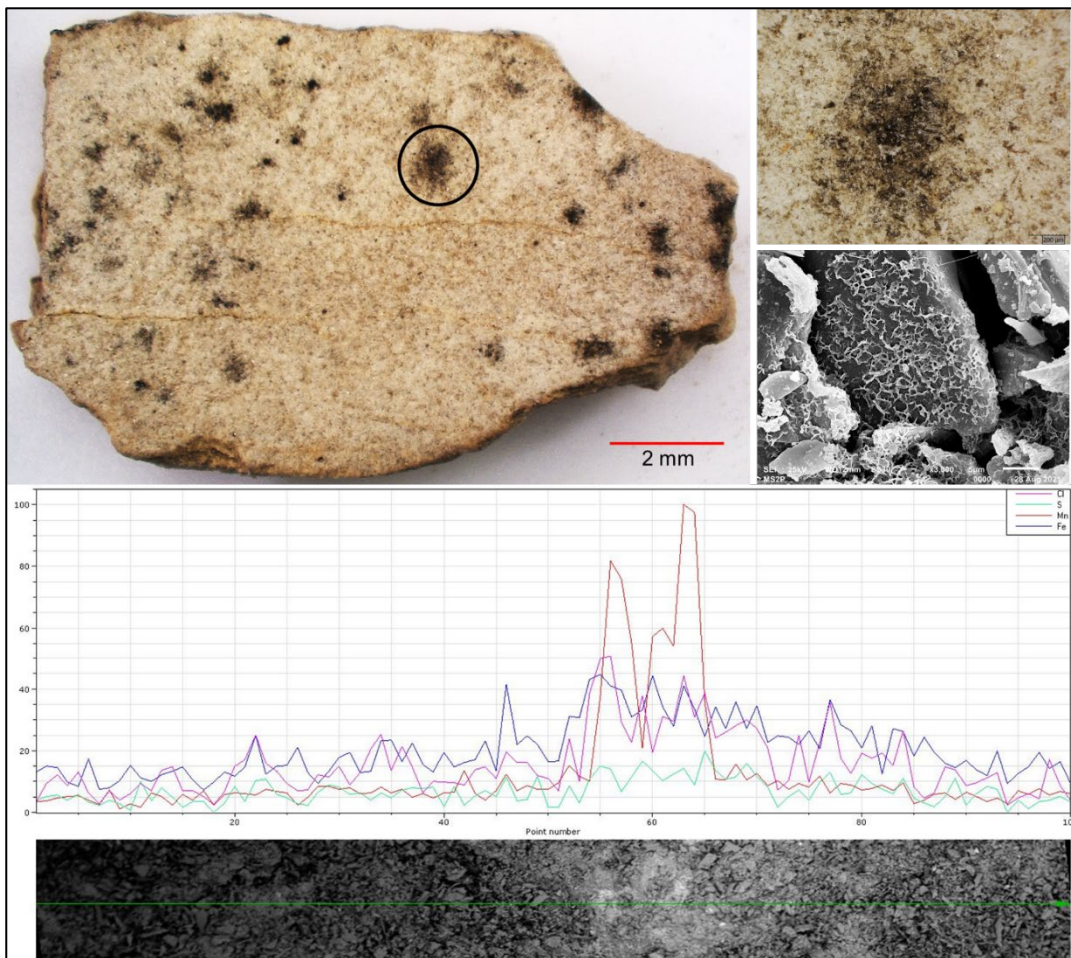
Figure 3.4: Image and micrograph a fragment (reverse face) of MS1 hardpan from Jwalapuram (up). Line-diagram of one of black spots (down). Line-diagram from EDS shows higher presence of Manganese. Jones (2007) speculated that most of the black stains are Fe-Mn spots that are the signature of redox environment suggesting drastic loss of soil moisture. Current SEM-EDS data confirms the previous speculation that these spots are composed of Fe and Mn.

SEM screening of black specks on hard pans (MS samples) showed thin film of dendritic layer formed on the top of glass shards (fig. 3.3). These signatures were absent in case of SS samples. Line scanning through SEM-EDS (fig. 3.4) showed that these black stains contained Mn and Fe as argued by Jones[69].

3.1.3. Analysis of rhizosphere cast and hardpans from Jwalapuram

We employed micro-CT and SEM-EDS to understand the compositional pattern of root cast and hard-pans in Jwalapuram. Main idea is to explore the process behind the formation of same. SEM and micro-CT data showed that most of these root cast are entirely covered by layer of glass shards (fig. 3.5 and 3.6). Internally, they have bubbly-pelleted surface made of very fine sediment (fig. 3.5). Micro-CT data shows that the internal surface of cast is formed of relatively dense matter, probably dominated by Fe content coming from detrital matter. It also contains several fragments of highly dense material which could be a compound of Ti, S, and Ba (fig. 3.6).
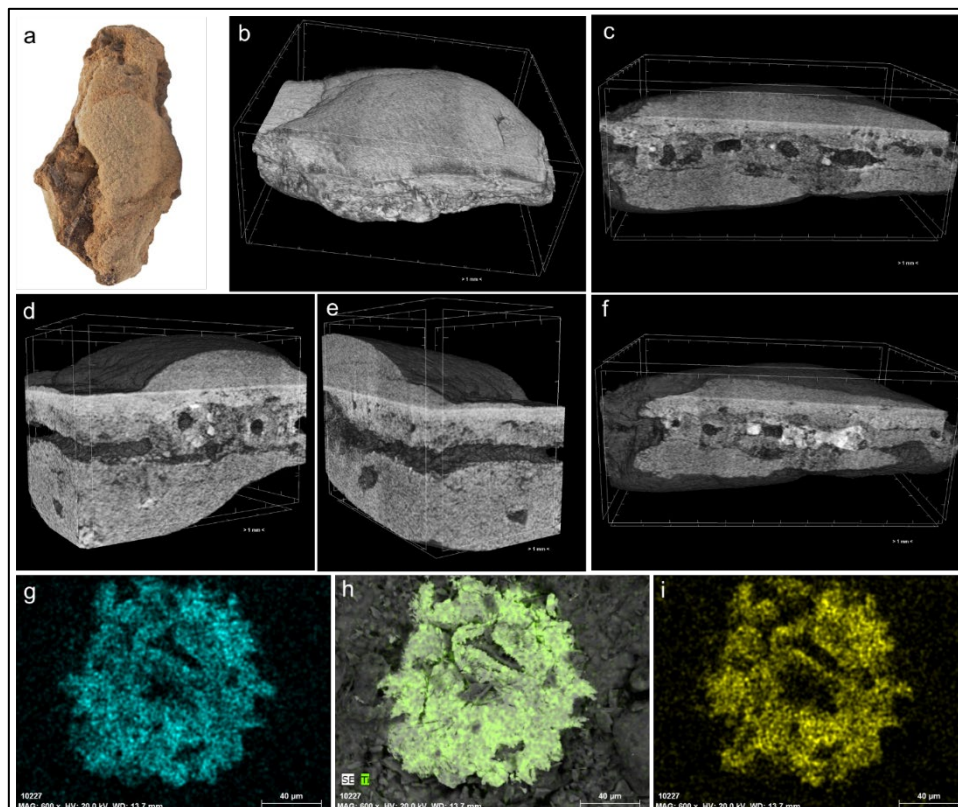
Figure 3.5: Micro-computed tomography of the fragment of greyish hardpan (MS1) from Jwalapuram. a. Coloured image of the sample, observe the greyish hardpan covered with glassy (silica) layer, b. Homogenous glassy substrate sandwiches the grey hardpan, c-f: decomposed rhizospheric cast reflected as less dense and black hollow feature. These root cast hole contains some very dense elements reflected by white specs. g-I, SEM-EDS micrograph (g. Sulphur, h. Titanium, i. Barium). White specs could be Fe-Ti oxide or any other Ti based compound that is very dense in nature.
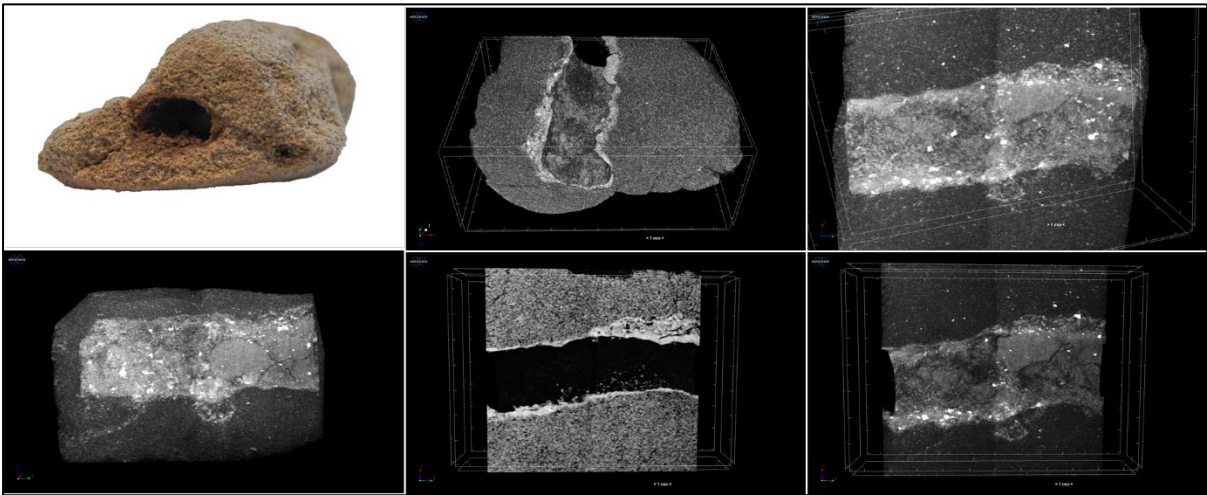
Figure 3.6: Micro-CT scan of rhizosphere from MS3 hardpan. Periphery of the root cast is marked by a relatively dense element. These dense specs could be Fe-Ti oxides, probably coming from detrital matter or YTT itself.

3.2. Inorganic paleoenvironmental proxies

3.2.1. Jwalapuram: Paleopedogenesis and Paleoenvironmental Implications

3.2.1.1. Elemental characterization based on XRF data

It is important to understand the elemental mobility caused due to chemical alteration, particularly understanding such mobility among major elements. Immobile elements such as Al, and Si shows lesser degree of temporal fluctuation in compared to other major elements.
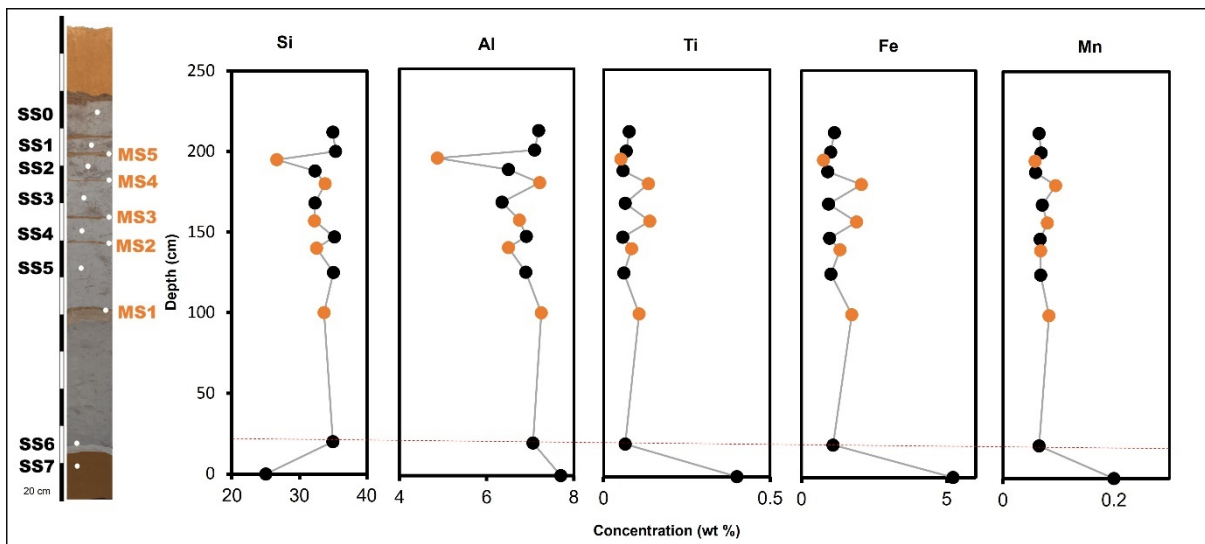
Figure 3.7: Elemental profile of lesser mobile or immobile major elements. Sharp fluctuation in all elemental profile is noticed during YTT ashfall (20cm). Al and Si has constant profile, showing loss during MS5 (195cm). Profile of Fe, Mn and Ti shows inverse trend and suggest gradual rise during MS stratum. Dotted red line marks the initiation of YTT ashfall. All black dots (20cm upwards) represent redeposited YTT stratum (SS). All orange dots represent cemented hardpan stratum (MS).

Figure 3.8: Elemental profile of base elements. Sharp fluctuation in all elemental profile is noticed during YTT ashfall (20cm). Na and K shows loss during MS stratum which in inversely reflected in Ca, Mg and Base profile, showing certain degree of mobility in these elements. Note the sharp rise in concentration of Ca, Mg and Base at MS5 (195cm) which inversely represented in K. Dotted red line marks the initiation of YTT ashfall. All black dots (20cms upwards) represent redeposited YTT stratum (SS). All orange dots represent cemented hardpan stratum (MS).

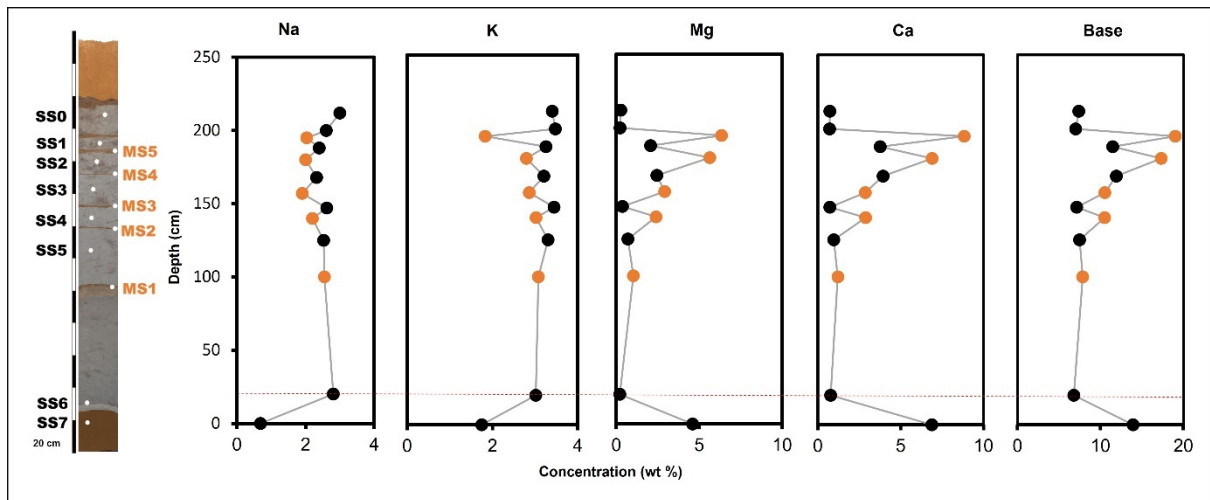Increase in Al and Si is noticed during YTT redepositions (SS stratums) (fig. 3.8). However, concentration decreases during the formation of pale-greyish cemented hard pans (MS stratums) (fig. 3.7). On contrary, other major elements like – Fe, Mn and Ti show opposite trends. Fe, Mn and Ti increases during the formation of MS stratums and decreases during SS stratums. However, the intensity of mobility among these major elements (i.e., Al, Si, Fe, Mn, Ti) is considerable low that's shows their stronger resistance towards chemical alteration[54].

Elemental trend in base elements (i.e., Ca, Mg, Na, K) shows remarkable amount of mobility in compared to previously discussed elements (fig.3.8). There are two different groups within base element showing two distinct trends. K and Na are monovalent alkali elements that increases during SS stratum and decreases in MS stratum although intensity of K and Na is much lower than other base elements. Temporal progression of the K and Na compliments Al and Si, showing constant trend in elemental profile.

Ca and Mg are divalent alkaline earth elements, showing different elemental profile than Na and K. Elemental profile of Ca and Mg shows higher degree of mobility in compared to other base elements. There is gradual rise in Ca and Mg concentration which reaches its pinnacle at MS5 and fall backs to normal during deposition of SS1. Profile suggests the oscillating or stepwise progression of Ca and Mg showing higher concentration in MS stratum than the SS stratum. The overall concentration of base elements is at highest during the formation of MS5 stratum which is inversely represented in element profile of K and Na.
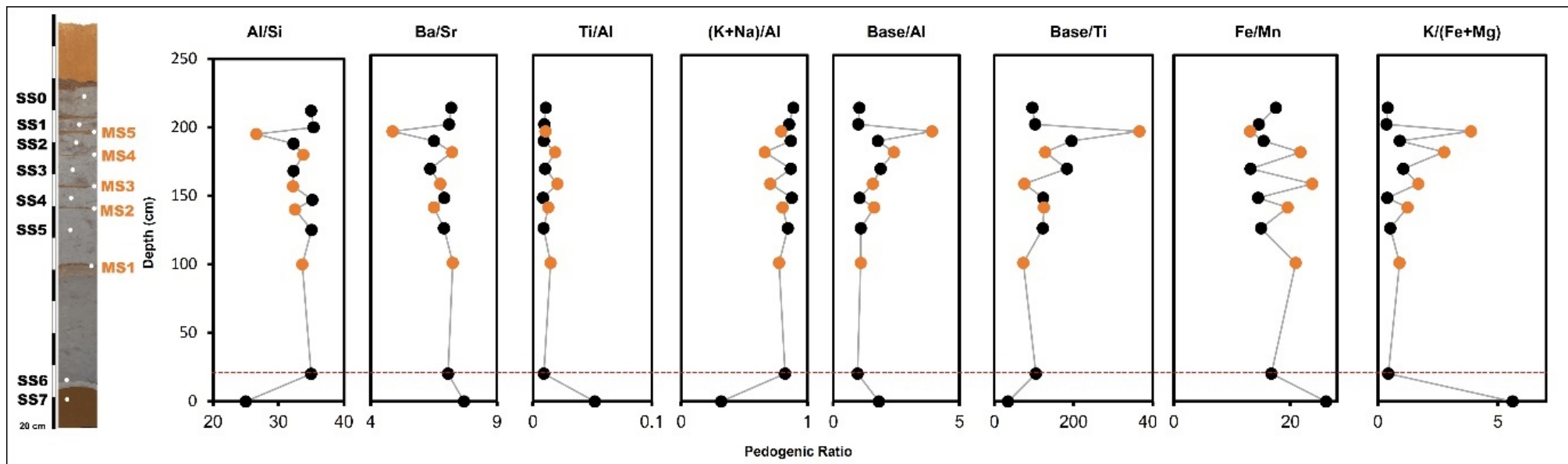
Figure 3.9: Molecular weathering and pedogenesis ratio. Sharp fluctuation in all weathering profile is noticed during YTT ashfall (20cm). Ratios based on base elements indicates higher elemental mobility during MS stratum. Dotted red line marks the initiation of YTT ashfall. Sharp fluctuation in all profile is noticed during YTT ashfall (20cm). All black dots (20cms upwards) represent redeposited YTT stratum (SS). All orange dots represent cemented hardpan stratum (MS).
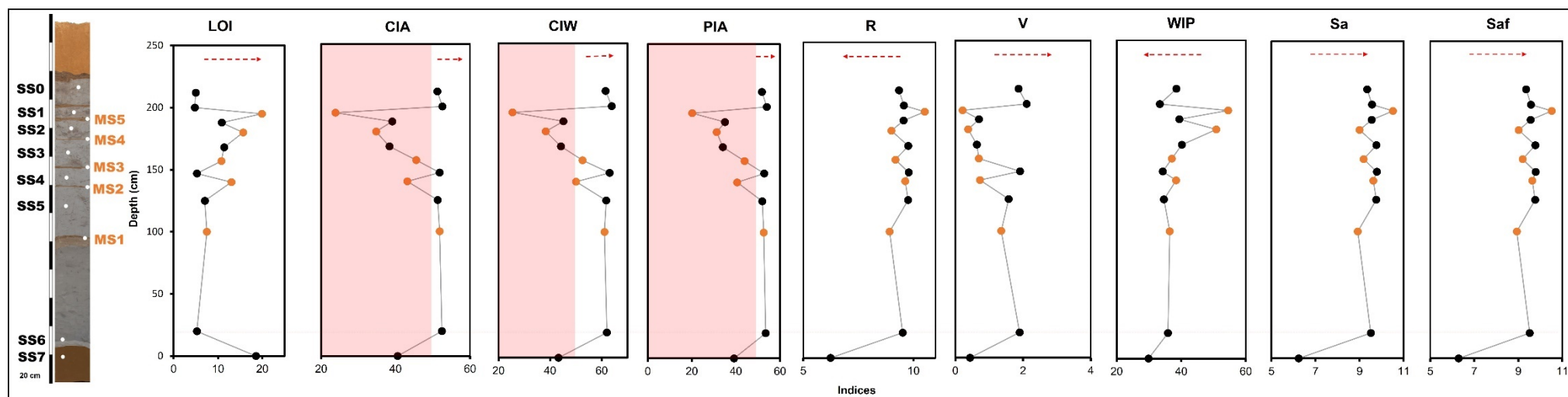
Figure 3.10: Indices of chemical alteration or weathering. Most of the indices suggest breakdown of compounds (possibly plagioclase) from SS stratum, resulting into the formation of MS stratum that is dominated by Ca and Mg based sesquioxide. All black dots (20cm upwards) represent redeposited YTT stratum (SS). All orange dots represent cemented hardpan stratum (MS). Abbreviation: loss in ignition (LOI), chemical index of alteration (CIA), chemical index of weathering (CIW), base alteration (BA), Ruxton Index (R), Vogt index (V), weathering index of Parker (WIP), silicon to aluminium ratio (Sa) and silicon to aluminium plus iron ratio (Saf). Red arrows show trend of index suggesting increase in weathering. Dotted red line marks the initiation of YTT ashfall. Red-coloured zone at CIA, CIW and PIA represents freshly weathered sediments.

Molecular weathering and paedogenic ratios

Different element ratio (fig. 3.9) represents different facet of paedogenic processes. Ratio of immobile elements such as Al, Si, and Ti show minimal degree of hydrolysis, reflecting lesser amount of clayness during sediment deposition in post-YTT phase[49,72–74]. According to Base/Al ratio, relatively higher degree of hydrolysis is observed during formation of MS stratum reflects higher mobility among base elements[75]. Generally, Ti and Al are immobile at near-neutral pHs (5.5-8) and they only become mobile under acidic pH conditions [49]. Increasing in Ti/Al ratio in MS stratum shows increasing acidification during that phase[76–78]. Most of the proxies of leaching and hydrolysis shows certain degree of molecular weathering during MS stratum which is comparatively higher than SS stratums.

Base element is more soluble and tend to leach and precipitate during chemical processes [50]. Base/Ti ratio show higher degree of leaching during SS stratums although maximum amount of chemical leaching is noticed at MS5. Reducing Ba/Sr ratio during MS stratums verifies the increasing nature of chemical weathering during that phase. Ba/Sr also highlights that relative intensity of chemical weathering was much higher between MS3 and MS5, pointing towards deterioration of environmental conditions. Reducing Ba/Sr trend at MS5 marks the extreme dry period[79–81]. MS stratum also show increasing Fe/Mn ratio, suggesting higher redox environment and period of less soil humidity[49,82]. Most of the pedogenic ratios suggests high degree of molecular weathering during MS stratums which is complimented by higher degree of mobility among base elements (fig. 3.9) and high redox environment during that period. As far salinization is concern, (K+Na)/Al ratios show no remarkable fluctuation during SS stratums although it reduces during MS stratums. Overall, salinization has very minimal contribution during pedogenesis which is also complimented by the elemental profile of Na and K (fig.3.8).

Other most important pedogenic ratio is the detrital input ratio (K/(Fe+Mg) showing contribution of detritism in soil formation process[83]. Detrital ratio shows that all MS samples has higher contribution of detrital input. Detrital input ratio mirror elemental trend of base elements (fig. 3.8) and S-Q trend of dolomite (fig. 3.14). Increase in detritism is the main marker of deforestation[84,85]. Thus, MS straum may have experienced remarkable degree of deforestation which was at pinnacle during MS5.

Chemical indices of weathering

Chemical weathering indices based on weathering resistant sesquioxide's of Al, Si, and Fe, such as Sa, Saf, Ruxton Index (R) show minimal or no weathering throughout the profile (fig. 3.10). It complements the molecular weathering ratio and elemental profile of immobile elements. On contrary, weathering indices based on sesquioxide's of base elements such as weathering index of Parker (WIP), BA, and Base/Ti highlights higher degree of chemical weathering during the formation of MS stratums. Among MS stratums, MS5 indicates the highest degree of chemical weathering and suggest severe dry and arid period[50,54,75,86–88]. Indication of highest aridity during MS5 is also highlighted by elemental profile (fig. 3.8) and weathering ratios (fig. 3.9). Other significant weathering indices like Chemical index of weathering (CIW) and Chemical index of alteration (CIA) presents the much-detailed picture of weathering cycle. As per CIW and CIA indices, all SS stratum falls in the ranges of minimal weathering and all MS stratum falls in the category of weathering products[48,49]. Thus, intensity of chemical alteration was much higher during MS period suggesting arid environmental conditions[89–91]. Both CIW and CIA supports WIP, BA and Base/Ti and indicates that the MS5 was the phase of highest chemical weathering. Inferences are further verified by Voght Index (V) that point towards increasing period of weathering between MS3 and MS5 where MS5 show highest degree of chemical alteration. Vogt's weathering profile suggest the formation of Ca and Mg based compounds during MS stratum, possibly due to the leaching of Al and K based compounds (plagioclases)[50]. Lastly, loss on ignition (LOI) confirms and verifies the trends discussed in other weathering indices. LOI represent the loss of CO_2 from sesquioxide, particularly from the sesquioxide's of Ca, Mg, Na, and K. LOI supports the fact that base elements and their associated sesquioxide were mobile and highly affected by chemical processes (possibly caused due to increasing aridity)[49,50,52,90]. Most of the indices of chemical weathering indicate towards the rising trend of aridity[52,77,88] which gets back to normal during SS1 and SS0.

3.2.1.2. Mineralogical profile and paleoenvironmental reconstruction (based on XRD data)

Different mineralogical profile explains the nature of sedimentological environment in Jwalapuram. Sediment in Jwalapuram is dominated by YTT deposit which has variety of minerals such as Quartz, Sanidine, Plagioclase, Biotite, Fayalite, Zircon, Ilmenite, Apatite,

chromite, Fe-Ti oxides etc[32,92]. Minerals like Fayalite, Zircon, apatite is in lesser amount (fig 3.11). However, remarkable amount of different Fe-Ti oxides were noticed during ED-SEM screening of primary YTT (fig. 3.11). Current study put more emphasis of major mineral types such as – quartz, clays, feldspar (aluminosilicates), biotite and dolomite, main intent is to understand the nature of deposition and alteration of minerals to determine paleoclimatic stress on mineralogical cycle. XRD data reflect certain signature of relative intensity of aforementioned compounds.

Amorphous and crystalline are two states that define the typical nature of solids (sediment in case), XRD helps to compute the amorphous-crystalline proportion. Amorphous-Crystalline ratio profile of JWP shows drastic changes in sedimentary sequence (fig. 3.13). Sharp increase in amorphous fraction is observed during primary YTT ashfall at SS6, occurred due to massive deposition of volcanic tuff (glass) in Jwalapuram. Crystalline fraction in post SS6 phase is mostly ranging from 7% to 40% with mean of 16.1%. Three major episodes of rise are observed in crystalline fraction profile between MS3 and MS5 where MS4 being the highest percentage of crystalline fraction of 39.2% in post-Toba phase. This rise is explained by the formation of neo-sesquioxide (such as dolomite) based on base elements (Ca and Mg in particular), possibly formed due to leaching and breakdown of Al, Si, Na and Mg based compounds (fig. 3.7, 3.8 & 3.9).
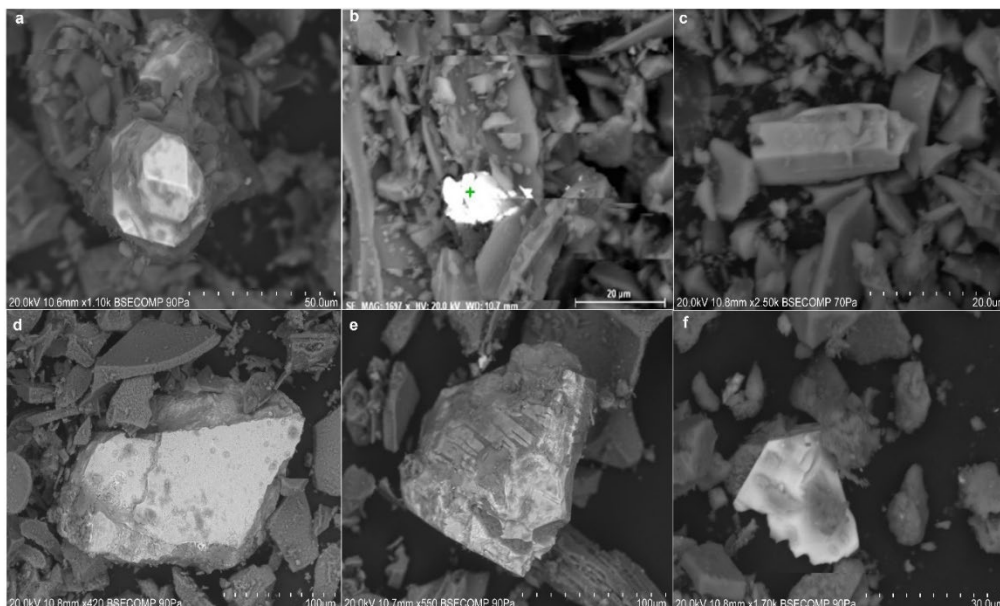

Figure 3.11: SEM (secondary electron image) micrographs of primary YTT from Jwalapuram (a-c) and Tejpor (d-f). (a & f) Zircon, (b) chromite, (c) Fe-Ti oxide and (d & e) Mn-rich ilmenite.

.
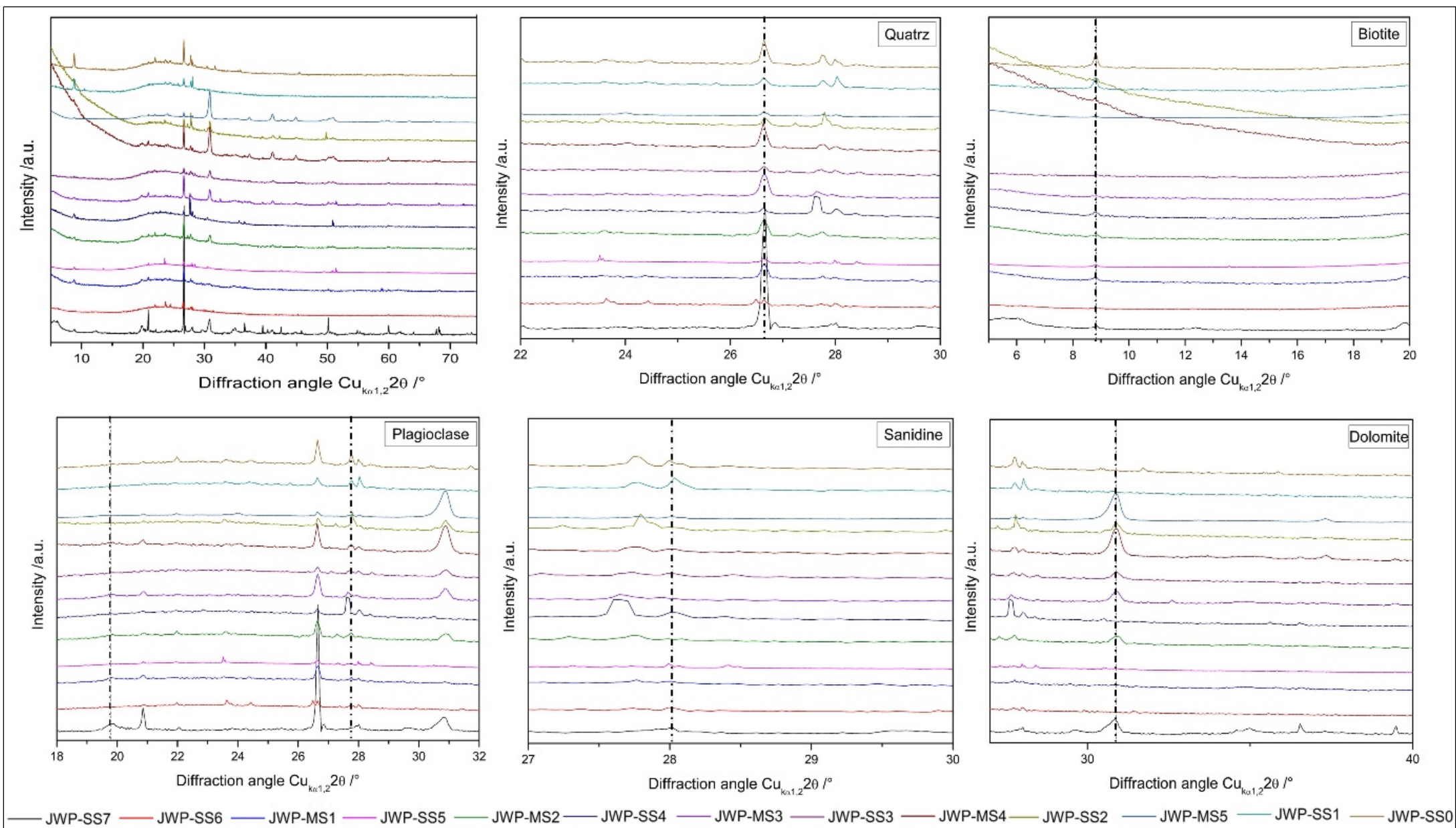
Figure 3.12: XRD diffractogram of JWP sediment showing invidual diffractogram of major mineral types . Dotted black line highlghts the peaks of specific compound. Note the gradual increase in dolomite.
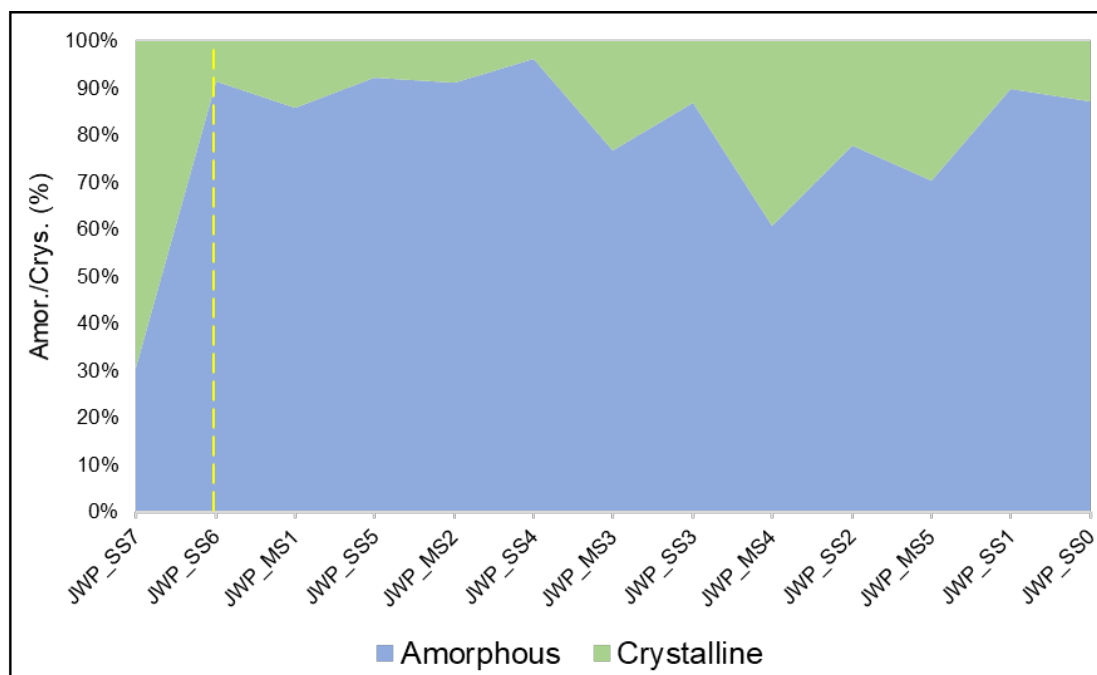
Figure 3.13: Amorphous-Crystalline ratio. More than 50% increase in amorphous fraction is observed in sediment sequence, marking the event of YTT ashfall in Jwalapuram. Dotted yellow line highlights the first phase of YTT deposition.

Similar trends are also observed in S-Q (semi-quantitative) profiles of major mineral groups (fig. 3.14). S-Q profile of quartz shows higher concentration during MS stratum although MS5 yields the lowest S-Q value. Lower S-Q value of quartz at MS5 is also complimented by the elemental profile of Si and SiO_2 (fig. 3.7). As S-Q value and Al/Si ratio (fig. 3.9) suggest breakdown of quartz due to hydrolysis and resulting into the formation of MS stratums. It is inversely reflected in S-Q profile of both feldspar types. Feldspar is one of the most weathering affected mineral group [48,49,70]. Due to chemical processes, feldspar tend to leach and disintegrate. During weathering, feldspar loses its base elements such as Ca, resulted into formation finer clayey like material. Lower S-Q values of plagioclase and sanidine during MS stratums shows elemental loss. Similarly, biotite loses its Mg due to weathering.

It suggests that the MS stratums are formed out of leached and weathered elements of underlying SS stratums, as it yields higher mobile base elements (Ca and Mg) and less concentration of immobile elements (Al and Na). Similar trends are also observed in the profile of CIA, CIW and WIP index profiles (fig. 3.10) where all MS stratum falls in the range of weathered products. Thus, it clearly demonstrates the nature of weathering that is caused by constant wet and dry events. S-Q profile of clay also point towards weakening of paedogenesis, suggesting dry and less precipitation during post-YTT phase.
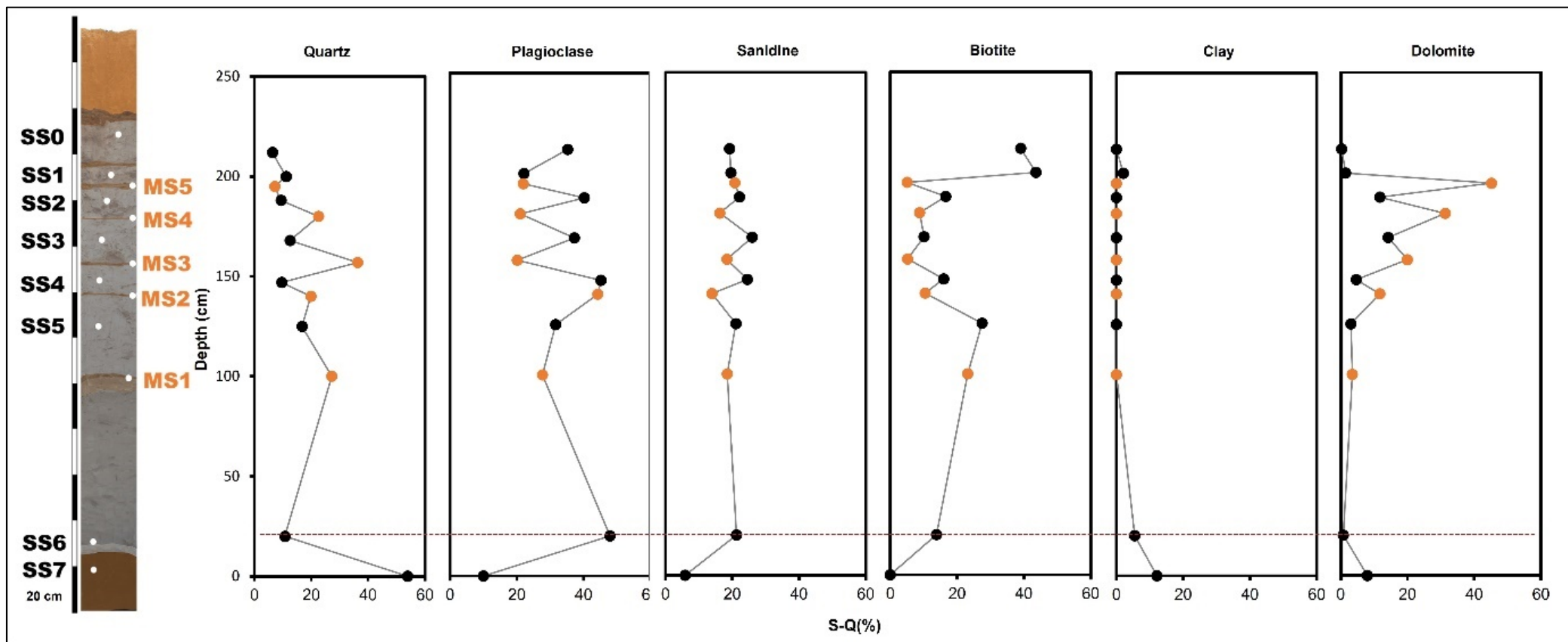
Figure 3.14: S-Q profile of major mineral types. Both feldspars show reduction during MS stratum. Biotite shows higher reduction between MS2 and MS5 where MS5 has lowest concentration of biotite in post-Toba phase. All black dots (20cms upwards) represent redeposited YTT stratum (SS). All orange dots represent cemented hardpan stratum (MS). Dotted red line marks the initiation of YTT ashfall.

Formation of dolomite: signature of aridification

Dolomite is a one of the common rock-forming mineral composed of calcium magnesium carbonate ($CaMg(CO_3)_2$). It often occurs as rhombohedral crystals which sometimes have curved faces[93]. Dolomite, $CaMg(CO_3)_2$ is known to have rhombohedral crystal structure ($R\overline{3}$ space group). Jwalapuram shows reflections in XRD patterns (corresponding to the conventional hexagonal, and Bravais-Miller indices, respectively) are unique to dolomite due to this distortion in charge density. These peaks with reference to the peak at ~30° 2θ corresponding to 104 Bravais-Miller index are used for identification of dolomite[93]. XRD data of Jwalapuram reflect formation of low temperature dolomitic, particularly during MS stratums (fig. 3.15a). As it explained earlier, the sediment samples from SS horizon shows signal of weathering of biotite and feldspar (fig.3.14). It seems that the weathering of these compounds led to formation of new sesquioxide. XRF data also verifies high chemical weathering and alteration of mineral type like feldspar and biotite where, Ca is mostly weathering from feldspar minerals and Mg is leaching from biotite and led to formation of dolomitic compounds[98–100]. Dolomitic compound in Jwalapuram seems to be stochiometric (non-authigenic) as Kaczmarek *et. al.* successfully temperature sensitive nature of dolomite that explains its formation during dry periods of hardpan formations (MS sample)[93] (fig. 3.15). Changing Mg^{2+} to Ca^{2+} ratios in dolomite indicate the changing environment in the area in which these compounds are formed.
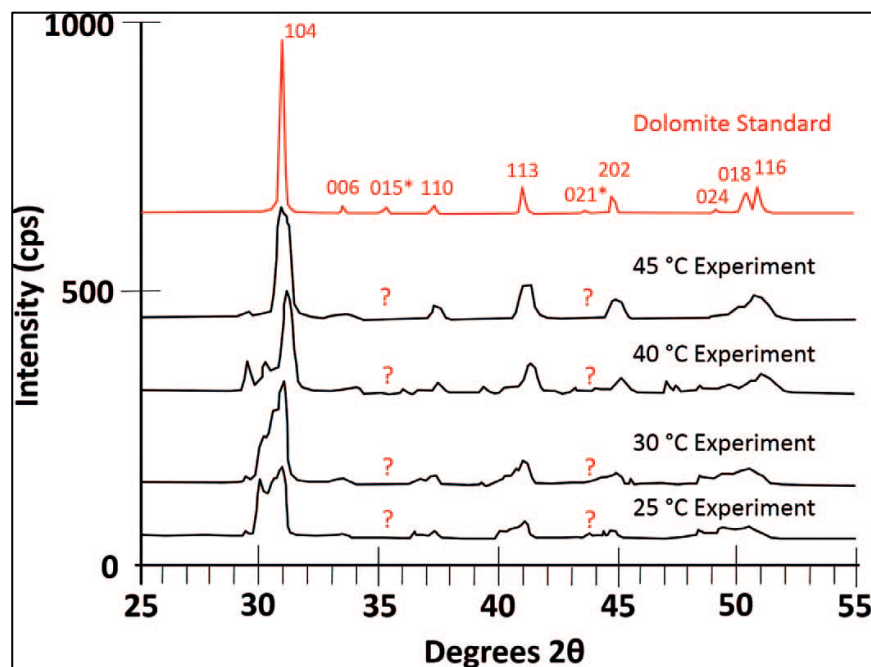
Figure 3.15: Simplified line tracings of XRD patterns (CuKa) for dolomite and a series of products made in low-temperature (25–45° C) experiments conducted at 25 to 55° 2hrs. Reflections labelled with *hkl* indices on dolomite standard. Note lack of ordering reflections in relative intensity of dolomite with rising temperature. Kaczmarek argues about microbial implication that contributes to dolomization with rising temperature (Kaczmarek *et. al.* 2017).

This ratio can mainly vary with temperature (25-60 °C) and microbial activity as suggested by Kaczmarek et. al.[93,101]. LOI profile (fig. 3.10) also compliments S-Q profile of dolomite, pointing towards the formation of evaporites during MS stratums. Similar weathering pattern of biotite and feldspar during post-Toba phase is also reported from other parts of India such as Sagileru [71] and Purna basin [70]. These pulses of dolomitization noticed in YTT sequence of Jwalapuram seems to be a profound signature of environmental aridification[102].
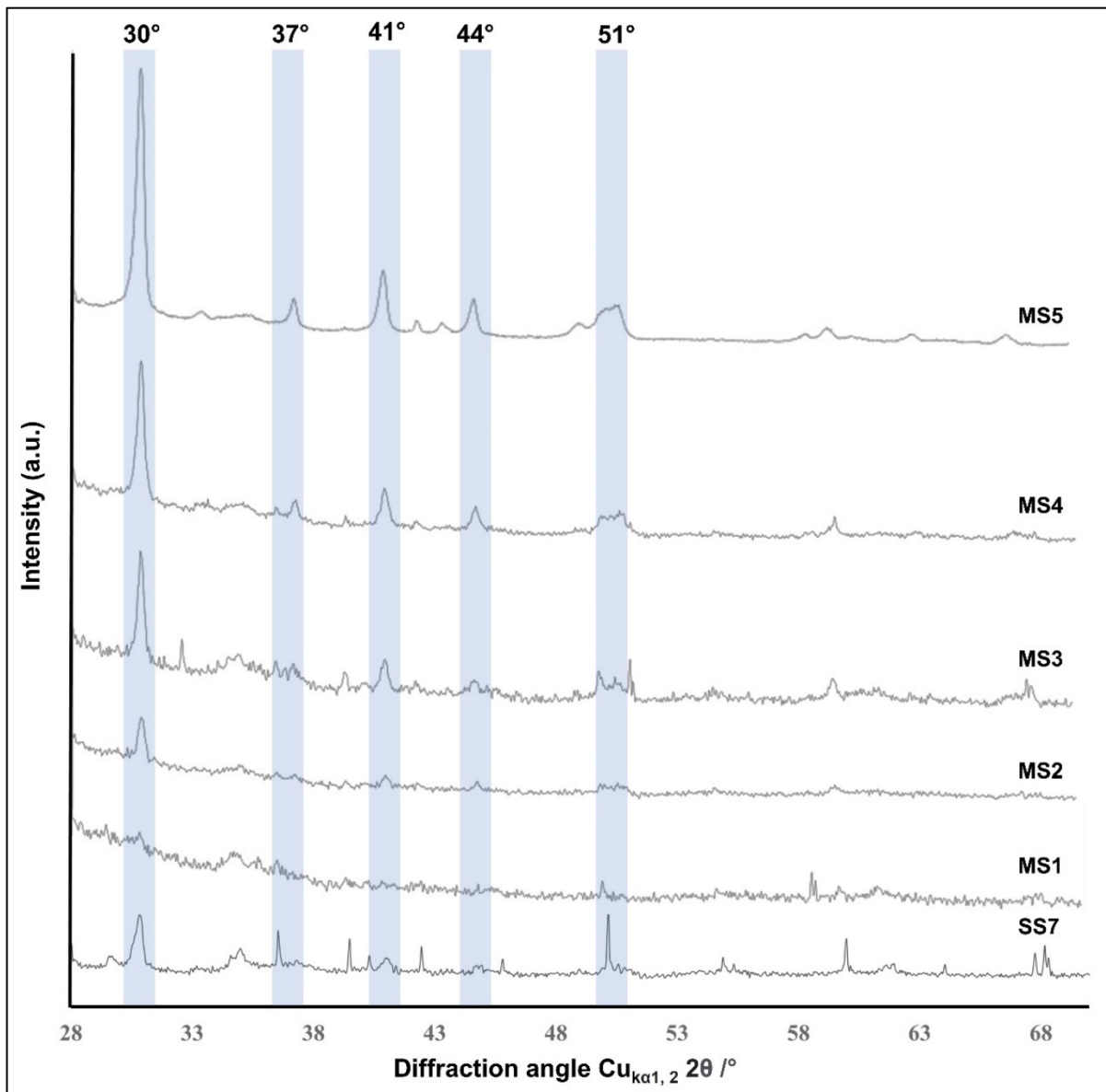
Figure 3.15a: Different reflection of dolomitic compounds are observed in XRD diffractogram of Jwalapuram at 30.8°, 37°, 41°, 44° and 51°. Note the rise in the relative intensity of dolomitic compound in Jwalapuram samples. Interestingly, pre-YTT samples of SS7 always shows reflection of dolomitic compounds. The gradual rise in dolomitic compound is also complimented by FT-IR, XRF and other XRD (S-Q) data.

3.2.1.3. Identification of Dolomite using ATR-FTIR spectroscopy and Paleoenvironmental Implication

Current study demonstrates that ATR- FTIR is an effective and time-efficient method to assess evaporites (qualitatively and quantitively)[101,103–105]. ATR-FTIR analysis of Jwalapuram samples compliment the signatures of dolomization what is reflected in XRD and XRF data. The ATR-FTIR spectra of Jwalapuram reflects significant intensities of bands originating from the vibrations of the group $(CO_3)^{2-}$ of dolomite (maxima at: 1431 cm^{-1}, 878 cm^{-1}, 728 cm^{-1})[104] (fig.3.16). Most significant band is noticed at 1431 cm^{-1} that shows V_{as} asymmetric stretching vibration of $(CO_3)^{2-}$. Other diagnostic bands are originating around 878 cm^{-1} and 728 cm^{-1} which belongs to γ – out of plane bending vibration of bonds O–C–O in $(CO_3)^{2-}$ group and δ – in plane bending vibration of O–C–O in $(CO_3)^{2-}$ group respectively[104,106]. Thus, these IR band could be attributed to the dolomite.

FTIR data highlight probable variability in the relative intensity of SiO2 in Jwalapuram samples since the intensity of the band is related to the amount of a compounds (Beer-lambert law) in a sample, considering the fact that the pathlength is the same. Reflected intensity of a band that is attributable to dolomite and same can be correlated with the amount of a certain compound (i.e., dolomite) on the samples providing that the experimental conditions are the
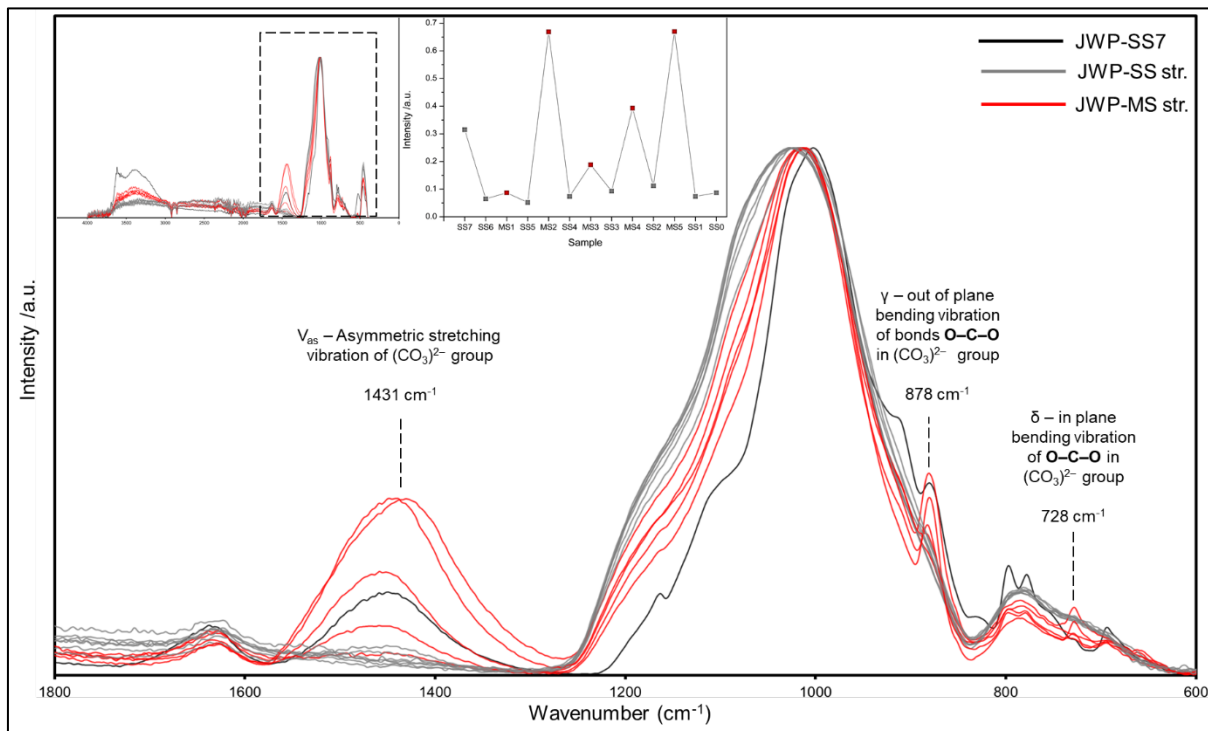
Figure 3.16 ATR-FTIR spectra of Jwalapuram, showing characteristic peaks of dolomite. Note the varying intensity of dolomite among Jwalapuram sediment.

same (which are in this case). Using that premise, abovementioned bands of are statistically fitted using gaussian fitting. Maximum IR intensity of bands are recorded and compared against depth model[102]. As like XRD and XRF, IR data showed the prominent relative intensity of dolomite at MS 5 and MS 4. JI et. al. used similar dolomite signatures for reliable correlation with arid environmental phases (such as Heinrich events)[103]. ATR-FTIR data of Jwalapuram show similar signatures of dolomite that can be conserved as a sign of environmental aridification particularly during MS5 which has highest band intensity (fig. 3.16).

3.2.2 Tejpor

Paleopedogenesis and Paleoenvironmental Implications

3.2.2.1. Elemental characterization (based on XRF data)

Sediment sequence at Tejpor represents the temporal archive of at least 35ka, demarcated by thin YTT layer. Most of the elemental and mineralogical profiles show sharp change in trend at the time of YTT ashfall. Immobile major elements (fig. 3.17) such as Al, Si, Ti, Fe, shows relatively constant trend throughout sequence (excluding YTT horizon). Among all immobile major elements, Mn shows sharp rise between S7 and S13. Usually, profile of Fe and Mn compliments each other and any fluctuation in profile suggests change in redox environment. However, Fe profile doesn't show any rise between S7 and S13. Increase in Mn could be related to the increase in detritism[83].

Elemental profile of base elements (fig. 3.18) shows certain episodes of changes before and after Toba event. YTT contains higher amount of Na and K than local sediments. In contrary,
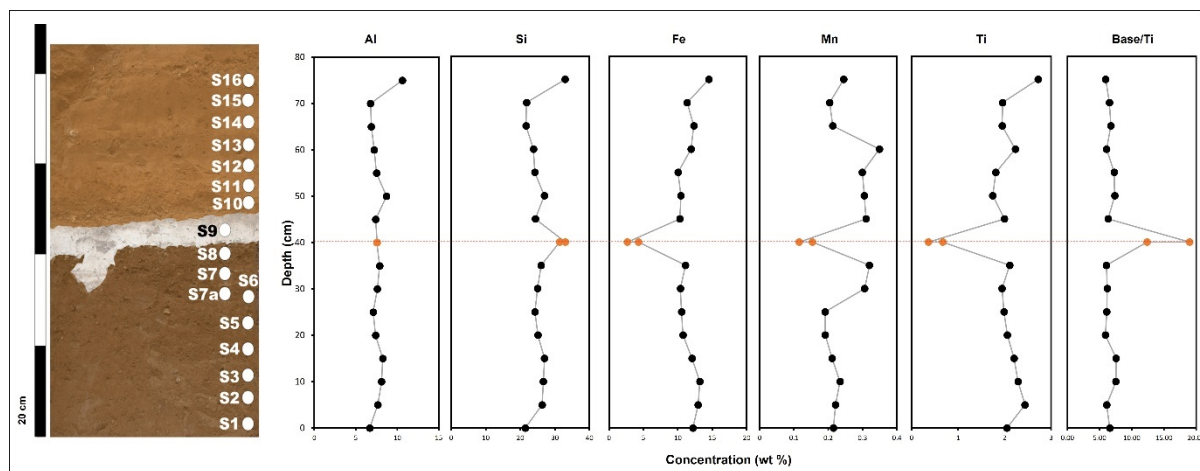
Figure 3.17: Elemental profile of lesser mobile or immobile major elements. Sharp fluctuation in all elemental profile is noticed during YTT ashfall (40cm), highlighted by the sharp rise in Si concentration. Dotted red line shows the period YTT ashfall. YTT layer is represented by orange dots.

Ca and Mg is much higher in local sediments that YTT. Ca and Mg profile shows fluctuation in elemental profile between S2 and S5. Similar trend is noticed in ΣBase profile that indicate
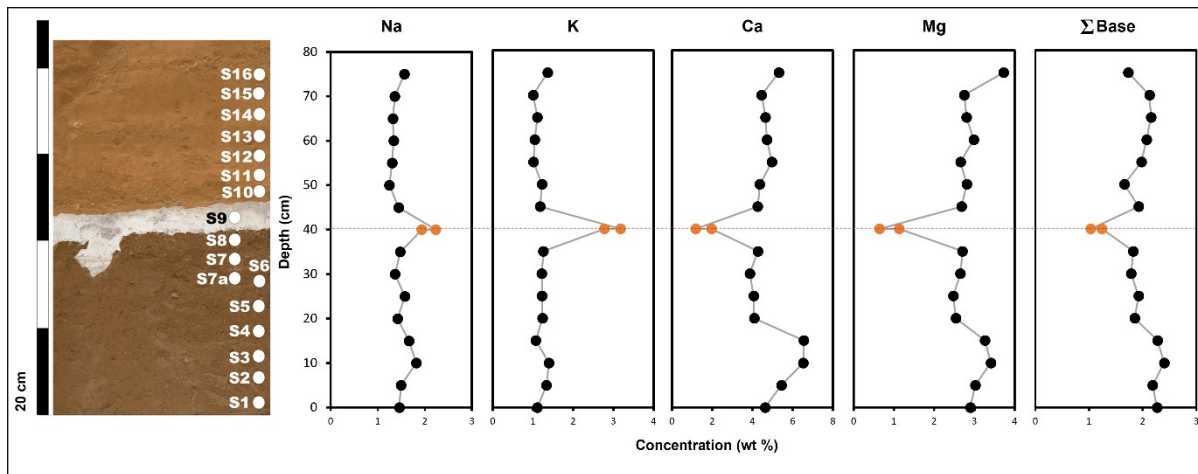
Figure 3.18: Elemental profile of base elements. Sharp fluctuation in all elemental profile is noticed during YTT ashfall (40cm). YTT ashfall is represented different by both groups of base elements, Na and K shows rise during ashfall phase which is inverse reflected in Ca and Mg profile. Dotted red line shows the period YTT ashfall. YTT layer is represented by orange dots.

the rising concentration between S2 to S5 and S11 to S16. Certain rise in base elements could be the result of higher mobility among these elements reflecting changing environmental conditions, possibly indicating towards slightly drier environment[49,54,83].

Molecular weathering and paedogenic ratios

Different paedogenic ratios based on Al shows different signals of hydrolysis before and after Toba eruption. Relative increase in Al/Si ratio at the depth of S4 indicate the increase in clayness, mostly formed due to the leaching of silicates[72–74,89]. It is complimented by rise in elemental profile of Si and mobility among base elements was also noticed during that phase. Episodes of rise in Al/Si ratio are inversely reflected in Ti/Al ratio showing certain drop in leaching processes, which could be pointing towards less acidic environmental conditions[49]. Similar trend is noticed in salinization profile ((K+Na)/Al). However, most of the fluctuation is not severe, thus, paedogenic environment is relatively stable throughout the sequence.

Weathering ratios like (K+Na)/Al and Bases/Al shows relative mobility among base elements during previously mentioned phases (i.e., S3 to S5 and S12 to S16). Specially during post YTT phase, increase in the leaching and hydrolysis of base elements which get back to its former condition in the end (S16). Gradual rise and fall of weathering trend are observed in weathering (fig.3.19) and elemental profile (fig.3.18) of base elements. Fe/Mn profile of TJP shows massive fluctuations. There is a sharp drop in redox environment is noticed between S6 and

S13 which gets back to normal at S14. It is inversely reflected in the elemental profile of Mn (fig.3.17). It is hard to explain the nature of rise, it could be a marker of reduction in detrital flux[109]. Although detrital input ratio doesn't show such changes (fig 3.19)

Chemical Indices of weathering

Different indices of chemical weathering reflect changes in paedogenic environment in Tejpor (fig. 3.20). LOI values of TJP ranges from 11% to 5% where YTT layer yields the lowest LOI value of 5.26%, confirms the argument that YTT event occurred during wetter environmental conditions (similar trends in these indices are also noticed in Jwalapuram)[23]. LOI shows that the gradual rise in CO_2 from S4 and continues till YTT ashfall (S9). Relatively higher LOI rise is observed in post YTT phase, 1.38% rise in LOI in post YTT phase shows relatively drier environment after Toba eruption[110–112]. However, LOI turnover after Toba is not that massive, showing minimal change in paedogenic environment. Among chemical indices, WIP show sharp rise in weathering during mobile alkali and alkaline elements, also supported by the rise in BA profile. Other chemical weathering indices like CIA and CIW shows small events of chemical alteration. Drop in CIA and CIW between S2 and S5 pointing towards the depositions of freshly weathered products. Similar drop is also noticed between S11 and S15 showing accumulation freshly weathered sediments. It is inversely reflected in BA profile, reflecting mobility among base elements although there is no change observed in WIP, V, R and Sa-Saf profile during post YTT phase. Thus, different indices such as LOI, R, V, Base/Ti, Sa-Saf, IOL shows very minimal or no change in paedogenic environment.

3.2.2.2. Mineralogical Profile and Paleoenvironmental reconstruction (based on XRD data)

Crystallographic analysis throw light on crucial mineralogical info of Tejpor sediments. Geographically, Tejpor falls in the conjunctional region of Deccan trap, Northern Aravali and Eastern Vindhyan system[113]. Sites is situated on the riverbank which runs on the fault line dividing tertiary and quaternary deposits. Current regions possess complex mineralogical profile which is primarily predominated by basaltic minerals[47,113,114]. Sediment at Tejpor is mostly comprised of quartz, calcium dominated plagioclase (albite), augite (orthopyroxene), clays (smectite, chlorite, saponite and vermiculite) and zeolites (laumontite and stilbite) (fig.3.21). Current study only focuses on major mineral types such as quartz, biotite,
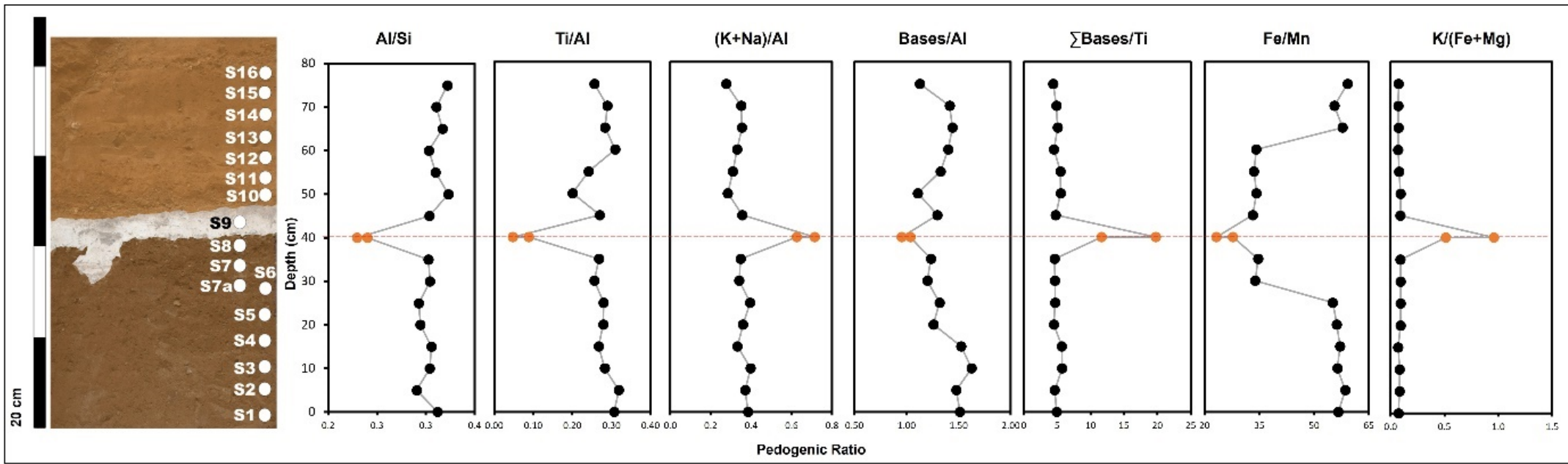
Figure 3.19: Molecular weathering and pedogenesis ratio. Sharp fluctuation in all weathering profile is noticed during YTT ashfall (40cm). Dotted red line and orange dots marks YTT event. Drastic drop in Fe/Mn ratio is noticed between 30cm and 60cm.
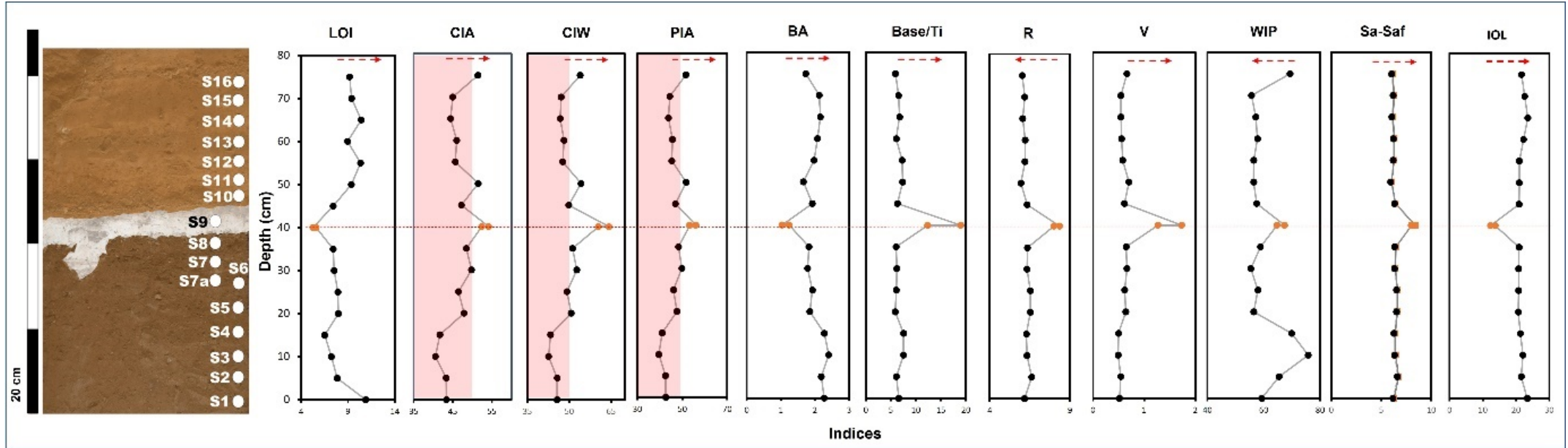
Figure 3.20: Indices of chemical alteration or weathering. Red arrows show trend of index suggesting increase in weathering. Dotted red line marks the initiation of YTT ashfall. All indices show sharp fluctuation in weathering trend during YTT ashfall.
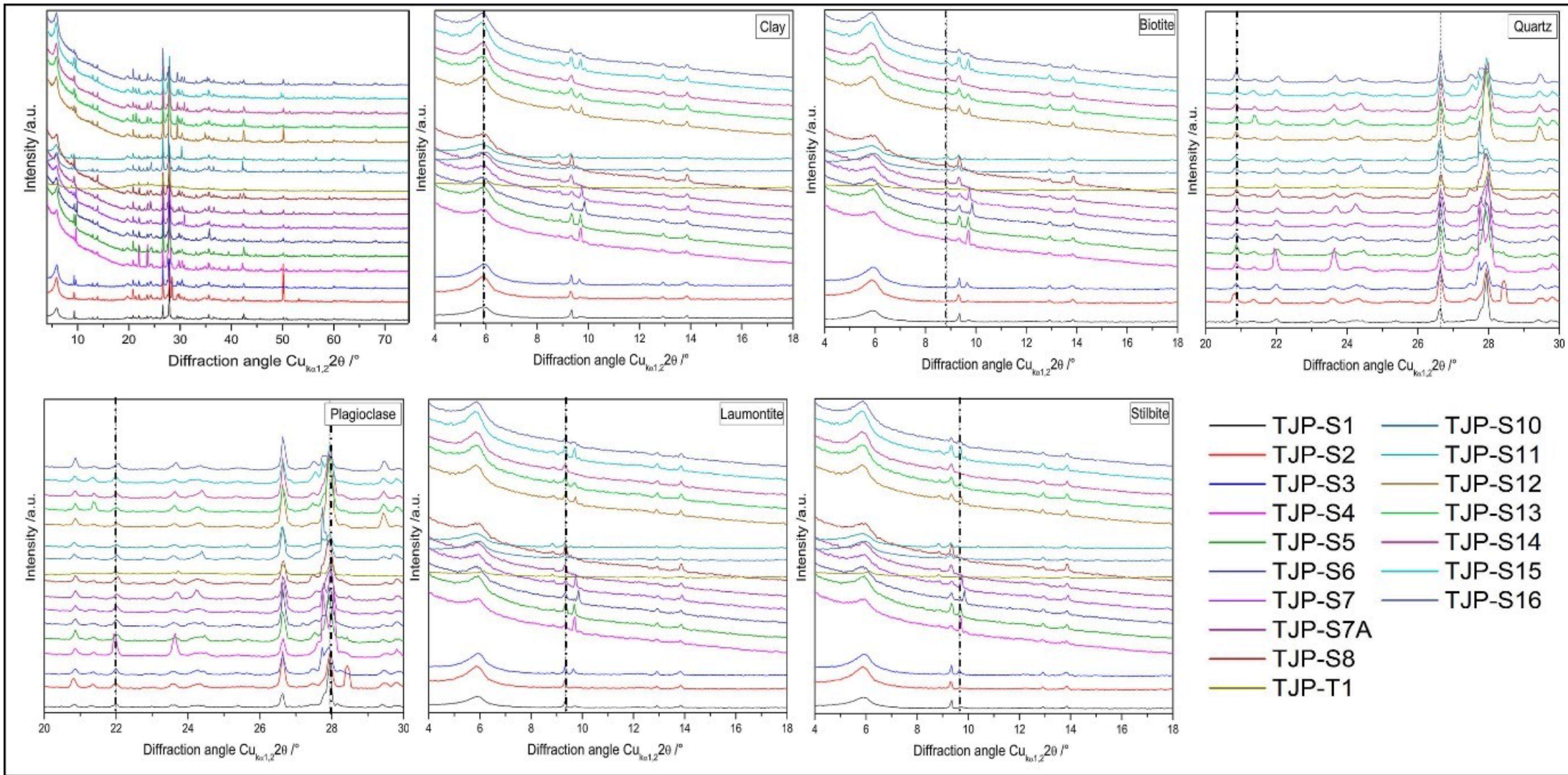
Figure 3.21: XRD diffractogram of JWP sediment showing invidual diffractogram of major mineral types . Dotted black line highlghts the peaks of specific compound. Most of the mineral types are consistent throughout the sequence except Stilbite

45

plagioclase, clays, and zeolite. Increase and decrease in the relative S-Q% provides important paleopedological information.

Amorphous-crystallinity ratio profile (fig. 3.22) of Tejpor shows sharp increase in amorphous fraction at T1/S9 (YTT layer). 45% increase in amorphous fraction is mostly result of vast deposition of amorphous Toba tuff, creating an isochron. Apart from YTT, amorphous-crystallinity profile highlights sharp rise in crystalline fraction during S4. Certain fluctuation during S4 is also observed in most of the weathering indices (such as, WIP, Base/Ti, BA, Base/ Al,) showing mobility among base elements and possibly new crystalline compounds.
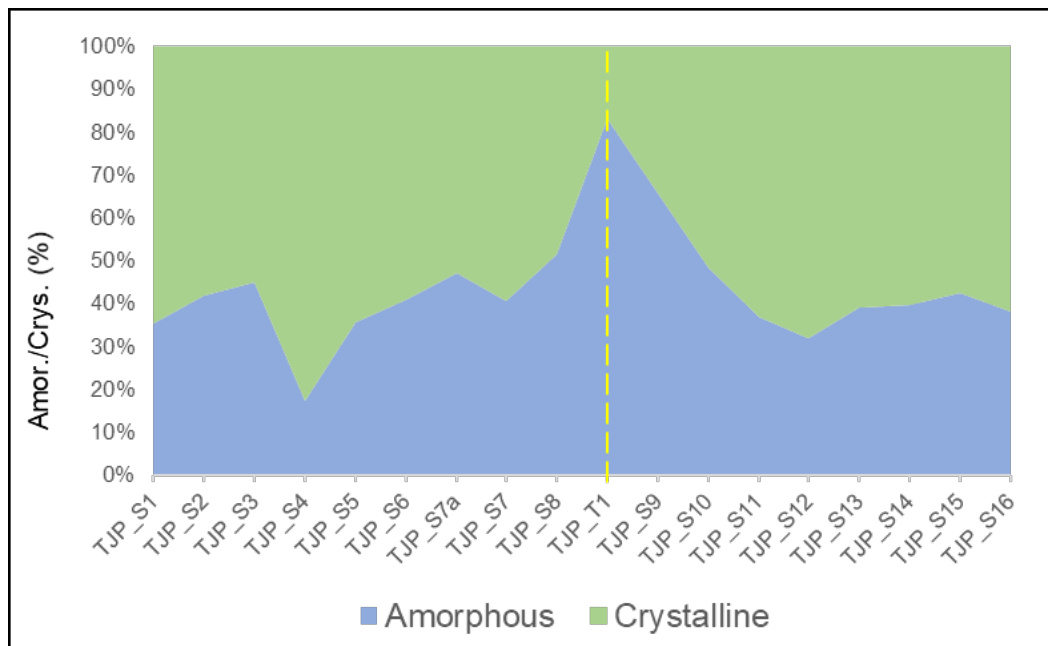
Figure 3.22: Amorphous-Crystalline ratio. More than 45% increase in amorphous fraction is observed in sediment sequence, marking the event of YTT ashfall in Tejpor. Dotted yellow line highlights the first phase of YTT deposition

However, soil LOI (CO_2) and Fe:Mn contradicts the formerly mentioned data suggesting showing slight increase in soil humidity[49,108]. Nevertheless, different indices based on XRF data highlighted that the paedogenic environment in Tejpor was relatively stable which is also supported by amorphous-crystallinity profile.

S-Q profile of different mineral types suggest certain changes in paedogenic environment before and after Toba eruption (fig. 3.23). As like amorphous-crystallinity ratio, most of the S-Q profile shows sharp fluctuation in trend during S4. Major loss in quartz is observed at same which is inversely reflected in plagioclase and biotite. Increase in plagioclase and biotite is supported by increase in Al/Si ratio and elemental ratio of base elements suggesting increase in paedogenic processes such as hydrolysis[107]. Loss in quartz could be signature of chemical

weathering suggesting increase solubility of quartz and higher mobility among alkaline elements such Ca and Mg[49,50,98]. Rise in weathering at S4 (15cm) is also complimented by rise in WIP (fig.3.20) and loss in clay S-Q (fig. 3.23). However, loss in LOI, and stable trend of Si contradicts the previously discussed signature. Post-YTT phase shows gradual fall in S-Q trend of plagioclase and biotite, showing relative weakening of fluvial processes and relative increase in weathering, also reflected in CIA and CIW profile (fig.3.20). Mineral types like plagioclase and biotite were more susceptible to chemical weathering during post YTT phase. There was certain degree of leaching among them which is resulting into the mobility of base elements and forming new sesquioxides. Certain rise in LOI profile (fig.3.20) in post-YTT phase confirms the rise in soil CO_2 due to the deposition of sesquioxides. It is inversely reflected in S-Q profile of clay and laumontite which are possible formed due to leaching or chemical weathering of minerals like plagioclase and biotite. As CIA and CIW (fig.3.20) showed the deposition of weathered products which compliments the rise in S-Q profile of clays and laumontite.

Tejpor shows mosaic of paedogenic feature, suggesting relatively stable environmental conditions. There are two signals of environmental changes were noticed, one at S4 and other immediately after YTT ashfall. These changes are complimented by most of inorganic proxies. It is quite evident that environment was already drier prior to Toba eruption (based on changes at S4) and continued afterwards although intensity of these changes doesn't seem to be that massive. Different molecular weathering and elemental ratio along with the different weathering indices show relatively stable environment suggest minimal impact on pedological processes due to Toba event.

3.3 Organic paleoenvironmental proxies

Pre-YTT, YTT and Post-YTT samples from Jwalapuram and Tejpur are analysed for leaf-wax biomarker analysis. Total lipid extraction was performed using accelerated solvent extractor (ASE). Extracted lipid is further analysed by gas chromatography-mass spectrometry (GC-MS) for assessing *n*-alkane distribution.

3.3.1. Jwalapuram

Leaf-wax biomarker
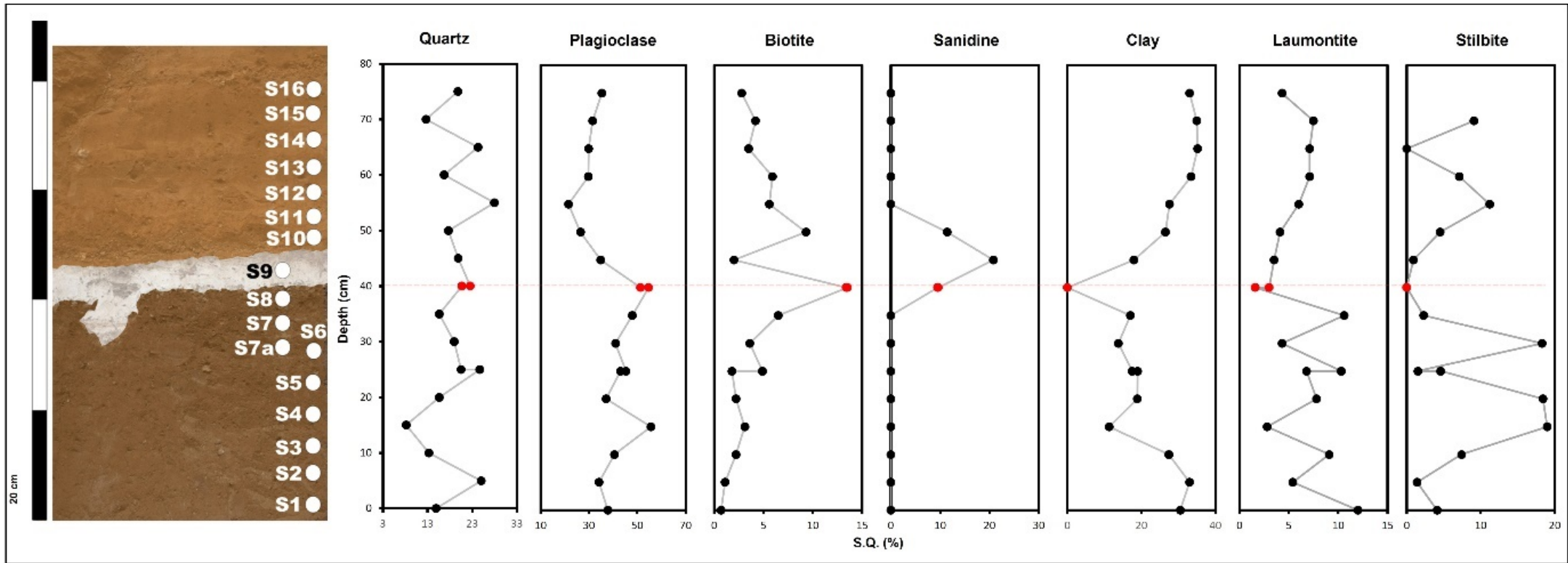
Figure 3.23: S-Q profile of major mineral types. Major increase in plagioclase, biotite, and sanidine is observed during YTT ashfall. Major fluctuation in S-Q trend is noticed at 15cms (S4). Dotted red line and red dots highlights the YTT event.

Current investigation exclusively focuses on *n*-alkane distribution. Four samples from JWP were processed for leaf-wax biomarkers: SS7 (Pre-YTT), SS6 (Primary YTT), MS1 (Post-YTT) and MS5 (Post-YTT).

Most of the samples yielded long series of *n*-alkanes homologue starting from C_{11} to C_{35} (fig. 3.24 and 3.25). Distribution pattern of *n*-alkanes in pre-YTT, YTT and post-YTT sediments provide significant insights into past plantscape and paleoenvironmental conditions. Relative abundance of short-chain *n*-alkanes (C_{17}-C_{21}) throughout the sequence ranges from 30.5% to 41.1%. Major increase of 10% is observed during (SS6) and immediately after Toba event (MS1) suggesting increase in aquatic algae and microbial community. However, relative intensity of short-chain *n*-alkanes gets back to its formal state during MS5. Relative intensity of mid-chain homologues falls in the bracket of 33.4% to 54.1% where MS5 shows highest relative abundance. Sharp rise of 15% in mid-chain *n*-alkanes in MS5 occurred due to the drastically increase in C_{23} suggesting massive increase in aquatic macrophytes and mosses plants[115]. This increase can also be considered a marker of increasing soil microbial activity [116].

Relative abundance of long-chain *n*-alkanes (C_{27} to C_{35}) ranges from 36% to 13.92% where MS5 shows the lowest relative intensity (fig.3.25 and 3.26). Sharp fall of 16-23% is observed in long-chain *n*-alkane post YTT ashfall suggesting decrease in terrestrial high plants cover[57,117]. Within long-chain *n*-alkanes certain *n*-alkanes such as C_{27} and C_{29} are highly present in woody plants and C_{31}, C_{33} and C_{35} are commonly found in graminoids (grasses) [118]. Long-chain *n*-alkanes in Jwalapuram samples are dominated by C_{27} and C_{29} suggesting higher population of woody plants in compared to grasses. Remarkable amount of decline is noticed among all long-chain *n*-alkanes. Relative loss of terrestrial high plants shows immediate impact of YTT event on Jwalapuram plantscape suggesting remarkable degree of loss in vegetation cover. Interestingly, increasing relative intensity of aquatic macrophytes and mosses suggest active lacustrine/marshy environment throughout the sequence.

n-Alkane ratio

Multiple ratios based on *n*-alkanes such carbon preference index (CPI), average chain length (ACL), aquatic plant *n*-alkane proxy (P_{aq}), terrestrial plant *n*-alkane proxy (P_{wax}), and
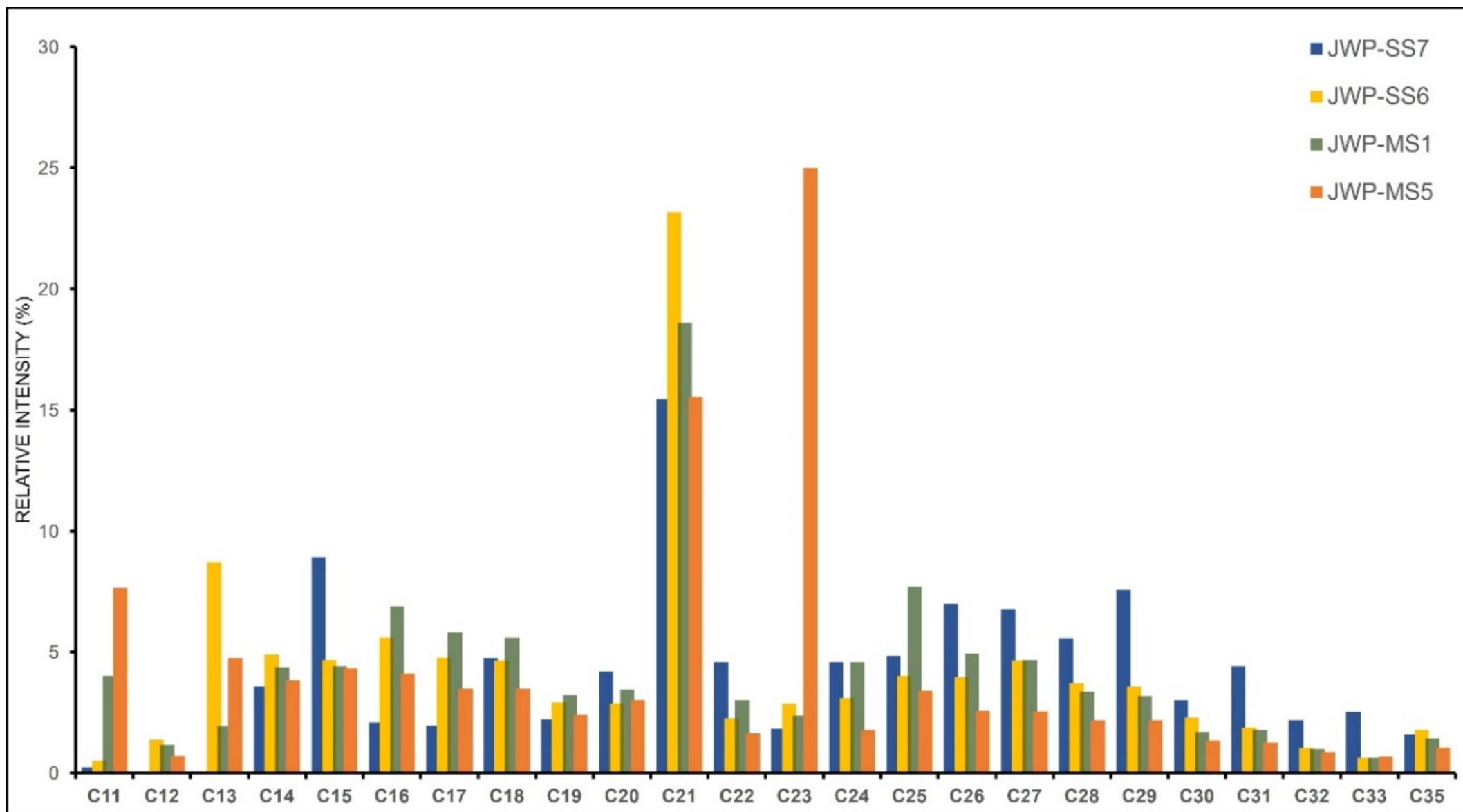
Figure 3.24: Plot of n-alkane distribution in Jwalapuram. Note the higher relative intensity of long-chain *n*-alkanes in SS7.
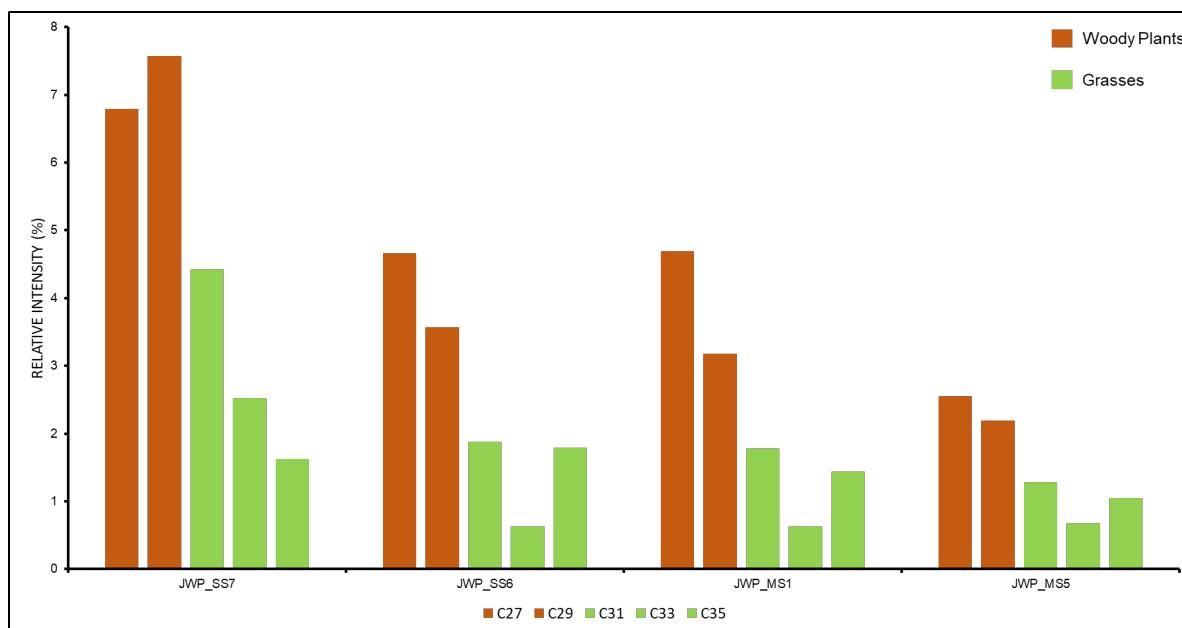
Figure 3.25: Distribution of long-chain n-alkanes in Jwalapuram. Note the predominance of C_{27} and C_{29} suggesting higher abundance of woody plants in compared to graminoids.
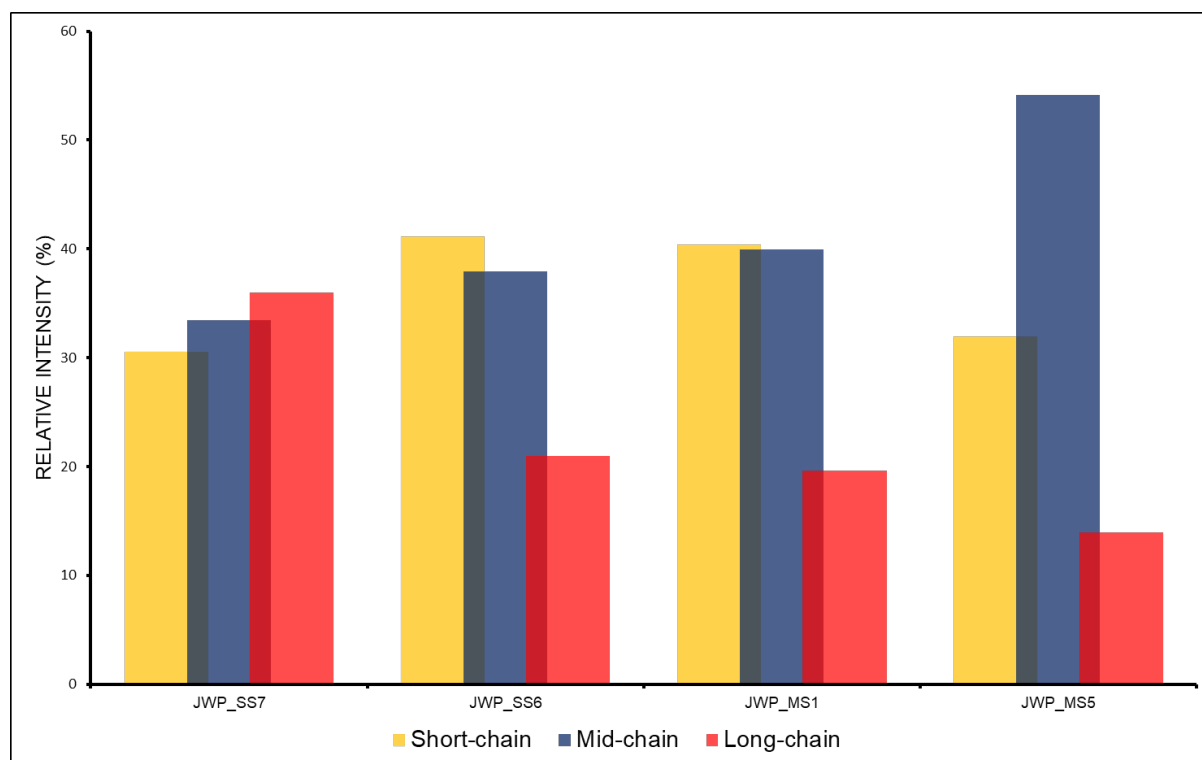
Figure 3.26: Plot showing difference in the relative intensity of short, mid, and long-chain *n*-alkane in Jwalapuram. Note the decreasing relative intensity of long-chain *n*-alkanes suggesting decline in terrestrial high plant cover after YTT ashfall.
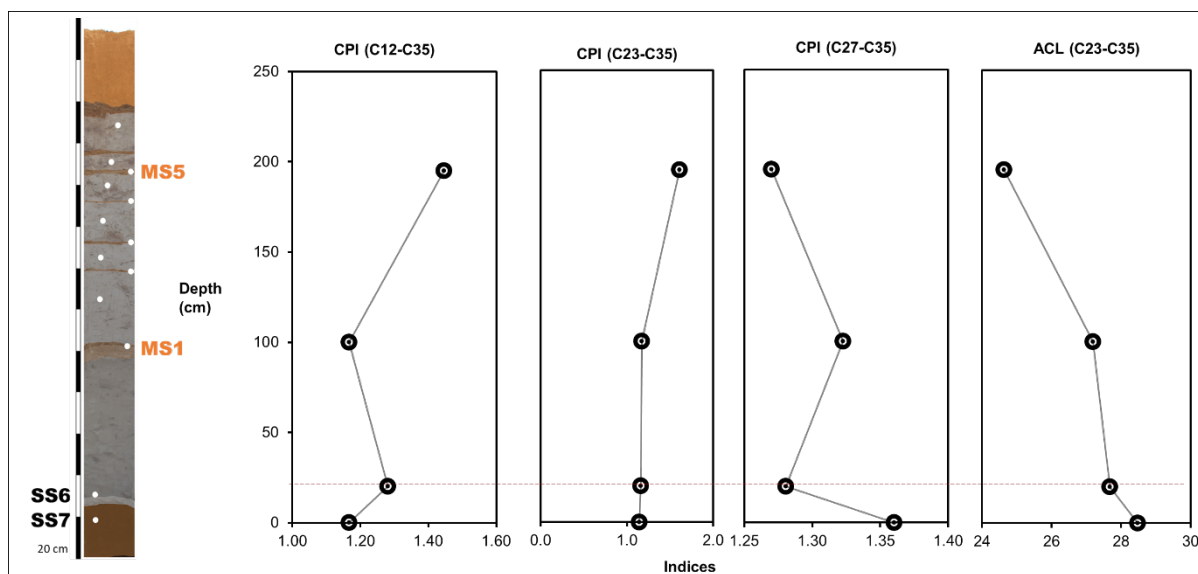
Figure 3.27: Carbon preference index and Average chain length of Jwalapuram. CPI based on mid-chain n-alkanes has inverse trend in compared to CPI of long-chain n-alkanes. Red dotted line marks the Toba event.

terrigenous aquatic ratio (TAR) are calculated to understand past environmental conditions [55,62].

Different carbon preference index is calculated based different *n*-alkane categories (i.e., short, mid- and long-chain *n*-alkanes). All CPI values are more than one suggesting predominance of odd over even numbered *n*-alkanes. All CPI values ranging between 1 and 2 suggesting terrestrial source of lipid[63]. Although CPI values are lower than 4 that suggest zero or minimal contribution of terrestrial high plants[119] (fig. 3.27). It seems most of organic matter is sourced from aquatic plants (submerged, floating, and sub-emergent aquatic plants) as suggested by Paq. data (fig.3.28). CPI values based on mid-chain *n*-alkanes show sharp rise during MS5 suggesting increase in aquatic macrophytes and mosses[119,120]. On other hand, ACL ($C_{23} - C_{35}$) values of Jwalapuram shows declining trend (fig. 3.27) ranging from 28.4 to 24.6. Changing ACL values may suggest change in environmental conditions that is manifested in changing homologues preference[121]. Sharp decline in ACL from 28 to 24 can be consider as a signature of shift in organic matter sourcing within aquatic plants (from emergent aquatic plants to submerged aquatic plants)[119]. However, it is still unclear what plant ACL variability reflects. ACL values do not remain constant as leaves develop and are not consistent across all plant groups or functional types[57].

Aquatic plant and terrestrial plant ratio highlight some important signatures of paleoenvironmental change (fig. 3.29). Paq. values of Jwalapuram ranges from 0.36 to 0.89 where MS5 has the highest value of 0.89. Paq. profile suggest higher contribution of emergent aquatic plants during pre-YTT (SS7) and YTT phase (SS6). Both MS stratum (MS1and MS5)
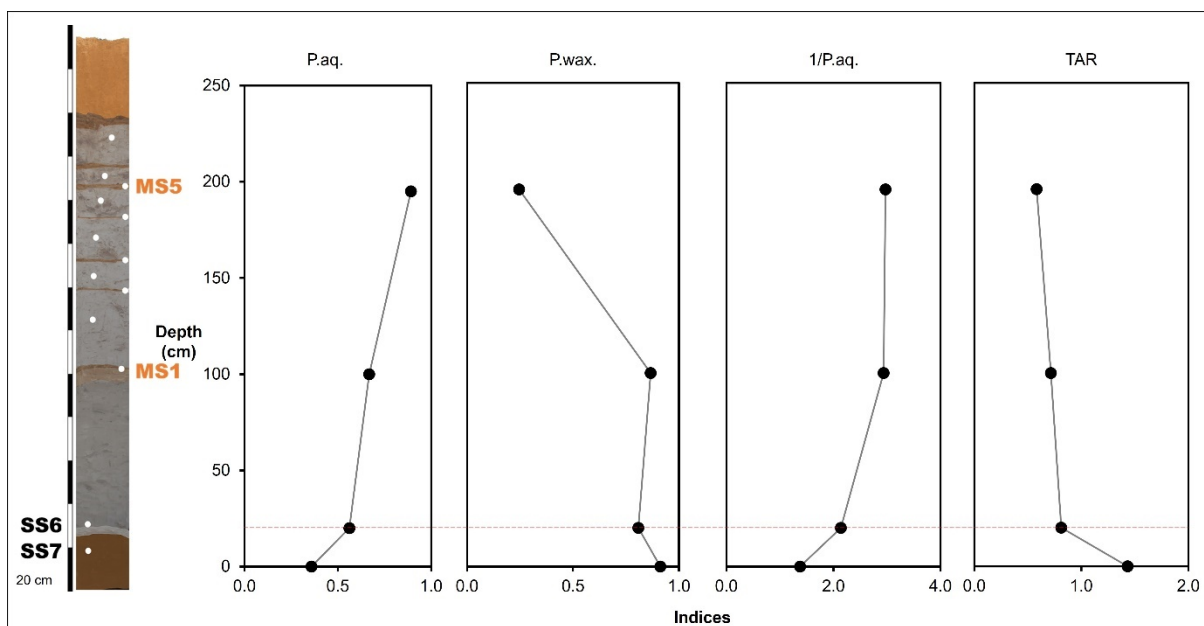
Figure 3.28: Aquatic plant (Paq.) and terrestrial plant (Pwax..) ratio and Terrigenous aquatic ratio (TAR). Note the inverse relationship between Paq. and Pwax. Red dotted line marks the YTT event.

has a higher Paq. value suggesting dominance of submerged aquatic plants. Similar trend is also manifested in 1/Paq. profile. Inverse Paq. profile suggest YTT and Pre-YTT are more inclined towards emergent macrophytes and highlight the reducing terrestrial contribution in post-YTT phase. Pwax. ratio is inversely related to Paq. ratio suggesting drastic drop in contribution of non-aquatic sources[118,122]. Pwax. ratio also highlight the predominance of lipid originated in autochthonous system[123]. These observations are further verified by terrigenous aquatic ratio (TAR) profile. TAR values of Jwalapuram falls in the category of 0.58 to 1.43. As per TAR values (fig. 3.28) sharp transition from terrestrial source to aquatic source is observed. Jwalapuram, YTT and post-YTT phases are dominated by aquatic sources. On contrary, TAR values are greater than one during pre-YTT phase suggesting higher contribution of terrestrial source that is probably coming from emergent aquatic plants as suggested by P_{aq}.data[124,125].

C_{27}/C_{31} and C_{29}/C_{31} ratio (fig. 3.29) explain the differences in the contribution of woody plants and graminoids. C_{27}/C_{31} ratio confirms (fig. 3.29) that pre-YTT phase has biogenic origin as value are ranging between 1 and 2[126,127]. YTT and post-YTT phases are dominated by non-biogenic source suggesting higher microbial or algae contribution[126]. C_{23}/C_{29} defines the contribution of aquatic macrophytes and terrestrial high plants. C_{23}/C_{29} ratio of Jwalapuram range from 0.24 to 11.56 where MS5 has the highest values of 11.56. Pre-YTT, YTT and post-YTT (MS1) phase shows the contribution of vascular plants (most probably emergent aquatic plants) as C_{23}/C_{29} values are less than 7[128]. Increasing C_{23}/C_{29} also suggest reducing

contribution of woody plants. Sharp rise in C_{23}/C_{29} is observed at MS5 suggesting dominance of *Sphahgum* (mosses) plants represented by C_{23}[123,128]. $C_{25}/(C_{25}+C_{29})$ also confirms the fact that post-YTT phases was dominated by aquatic macrophytes. $\Sigma(C_{24}-C_{35})/ \Sigma(C_{14}-C_{21})$ defines the character of the source based on spatial parameters. As Mead et al mentioned that organic matter basically sourced from two end member (allochthonous/terrestrial vs. autochthonous/microbial) systems. It is important to understand whether organic matter influx. $\Sigma(C_{24}-C_{35})/ \Sigma(C_{14}-C_{21})$ ratio suggest all sediment samples in Jwalapuram are coming from autochthonous sources suggestion higher contribution of microbial and algae sources[129]. Sharp fall in $\Sigma(C_{24}-C_{35})/ \Sigma(C_{14}-C_{21})$, particularly during MS5 highlights predominance of microbial
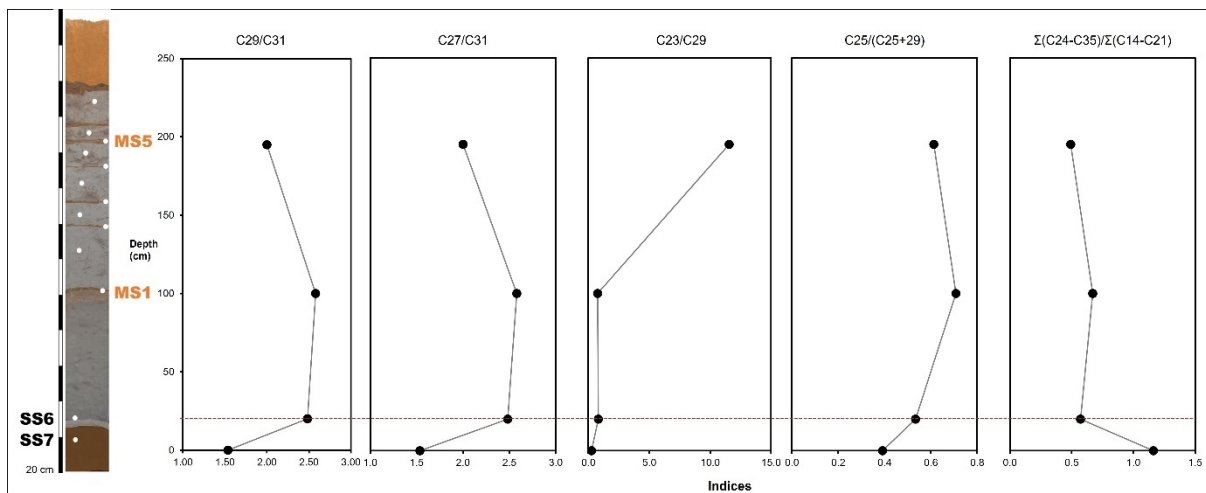
Figure 3.29: Different *n*-alkane ratio of Jwalapuram, exhibiting differences in sources and explaining contribution of mid-chain and long-chain *n*-alkanes. Dotted red line marks YTT event.

and algal sources.

3.3.2. Tejpor

Leaf-wax biomarker

Current investigation put special emphasis on pre-YTT (S8), YTT (EA1) and post-YTT (S10) stratums. Total three sample were analysed under GC-MS for leaf-wax biomarkers. All three samples have long series of homologues (*n*-alkanes) ranging from C_{11} to C_{35}. Main objective is to analyses the *n*-alkane distribution for understanding the paleoenvironmental and paleovegetation fluctuations may have caused by ~74ka Toba eruption. Relative intensity of *n*-alkanes is much higher in post-YTT phase (S10) and lowest at pre-YTT phase (S8) in compared to other phases, point towards certain fluctuations in environmental trend. Relative intensity of short-chain and mid-chain *n*-alkanes is relatively constant during pre-YTT (S8) and YTT (EA1) phase. There is a sharp increase (around 16%) in short-chain *n*-alkanes is observed

during post-YTT phase (S10) (fig. 3.30) It is possible that increase in short-chain n-alkane could be result of charred biomass or formation of topsoil which contains the aerosol produced due to thermal degradation[130]. It is mostly reflected in the relative intensity of short-chain even numbered carbon n-alkanes. Post-YTT phase (S10) does show higher relative intensity of even short-chain n- alkanes in compared to YTT (EA1) and pre-YTT phases (S8) (fig. 3.30). More likely, higher abundance of short-chain n-alkanes could be related to the predominance of microbial and algal sources. As like short-chain n-alkanes, mid-chain n-alkanes are also increased during post-YTT phase suggesting increase in contribution of aquatic macrophytes, algae and mosses[121,122,127]. Presence of active aquatic environment also suggest increasing soil microbial activity and algal contribution which is manifested in the increasing relative intensity of C_{21} [116].

Trend of long-chain n-alkanes give important insights about the impact of Toba eruption on the local environment of Tejpor. Relative intensity of long-chain n-alkanes is relatively constant during pre-YTT (S8) and YTT phase (EA1). Sharp fall of 20% in long-chain n-alkanes is noticed at post-YTT phase (S10) indicate the severe of terrestrial high plants (fig. 3.31 and 3.32). Within long-chain n-alkanes, C_{27} and C_{29} shows remarkable fall from 13.44% (S8) to 5.43 % (S10) suggesting severe loss of woody plants immediately after YTT event. Similar loss is also noticed in C_{31}, C_{33}, C_{35} suggesting certain loss in graminoids (grass) population. However, relative intensity of long-chain alkanes is comparatively lesser than mid-chain and short-chain n-alkanes. Most of the n-alkane ratio (fig. 3.33 and 3.34) reflect the presence of emergent aquatic plants than terrestrial high plants[119,122,127].

n-Alkane ratio

Different ratios are calculated based on the relative-intensity of n-alkanes explaining the sourcing and distribution within homologues. 5 different carbon preference indices are calculated to understand the proportional differences between odd and even numbered n-alkanes (fig. 3.33 and 3.34). All CPI value suggest predominance of odd over even numbered n-alkanes. CPI based on mid-chain and long-chain n-alkane suggest dominance of terrestrial sources, possible coming from aquatic plants as most of the CPI values range from 1.28 to 1.45[63].
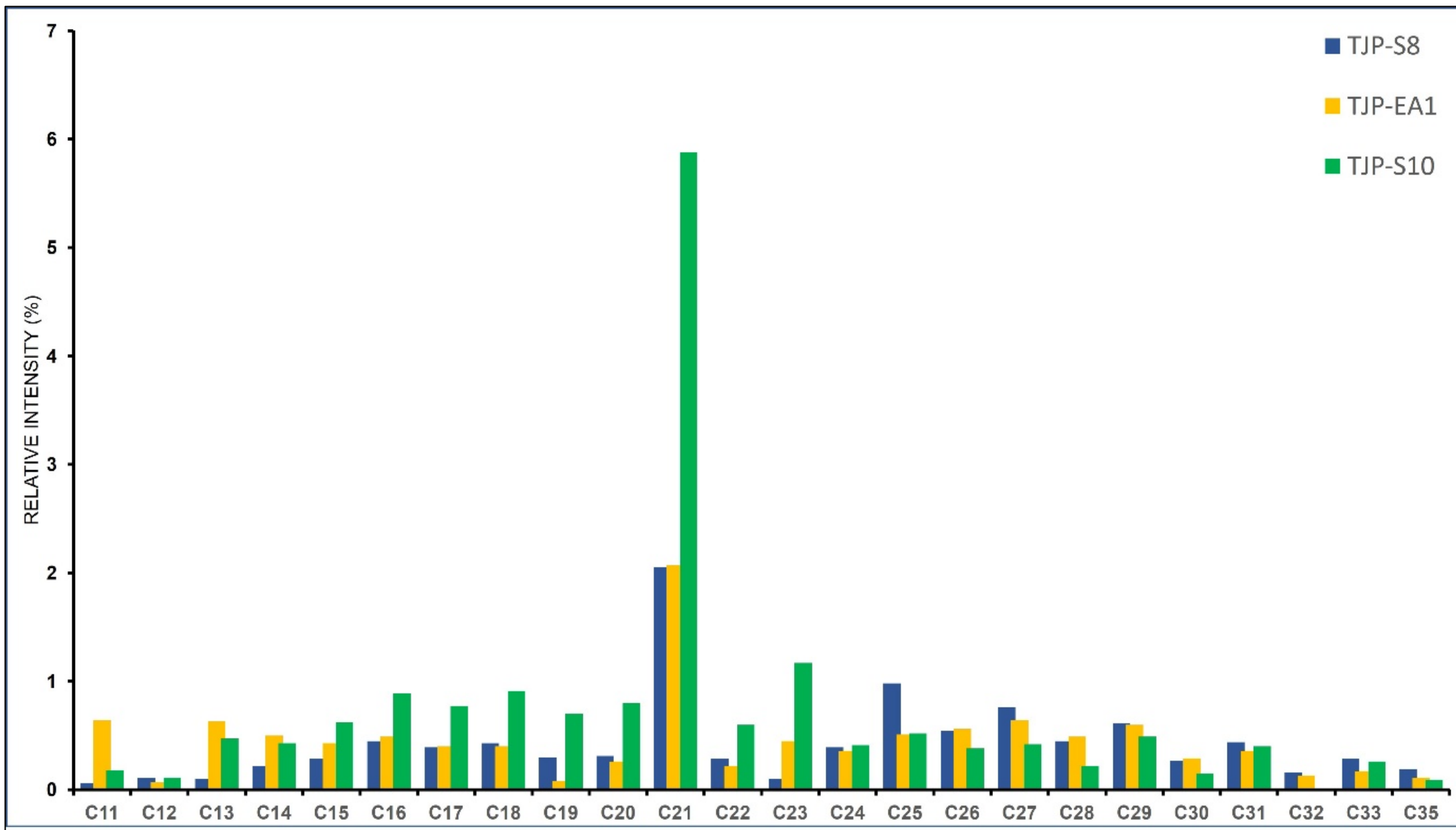
Figure 3.30: Plot of n-alkane distribution in Tejpor. Note the higher relative intensity of short-chain n-alkanes in S10 suggesting higher contribution of aquatic sources.
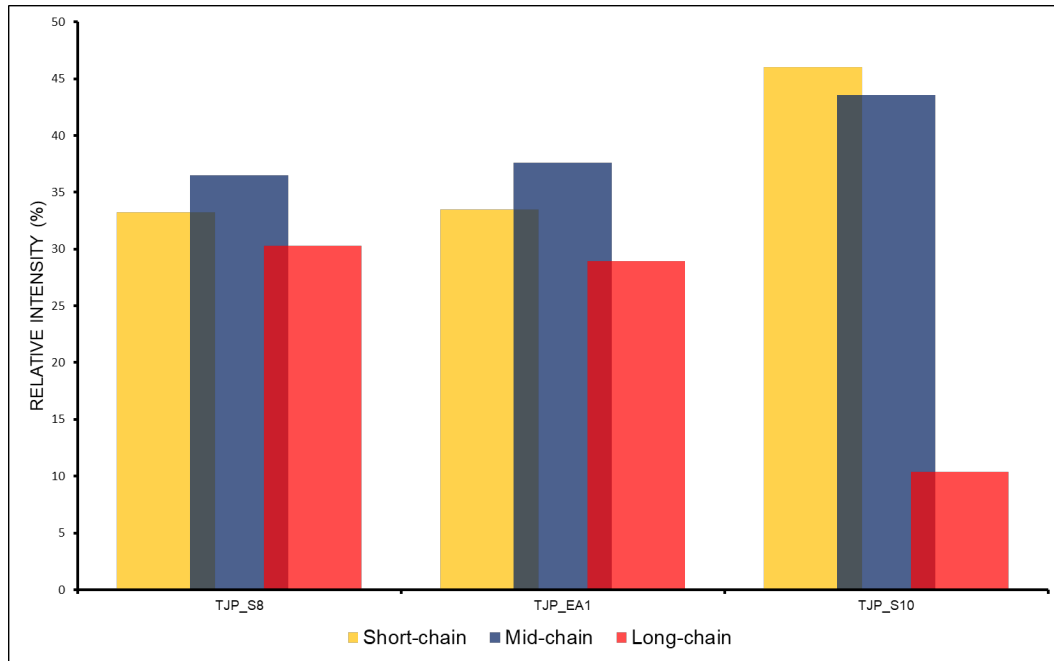
Figure 3.31: Plot showing difference in the relative intensity of short, mid, and long-chain n-alkane in Tejpor. Note the decreasing relative intensity of long-chain n-alkanes.
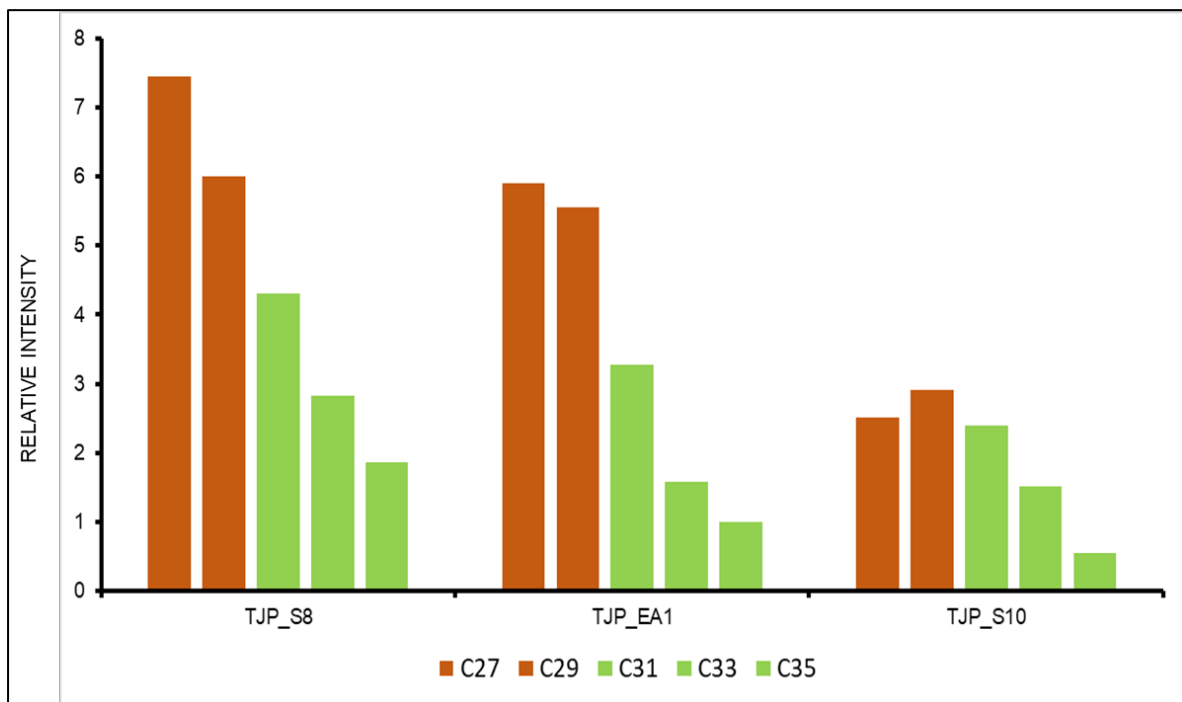
Figure 3.32: Distribution of long-chain n-alkanes. Note the gradual fall in C_{27} and C_{29} suggesting severe loss in woody plant cover during post-YTT phase.
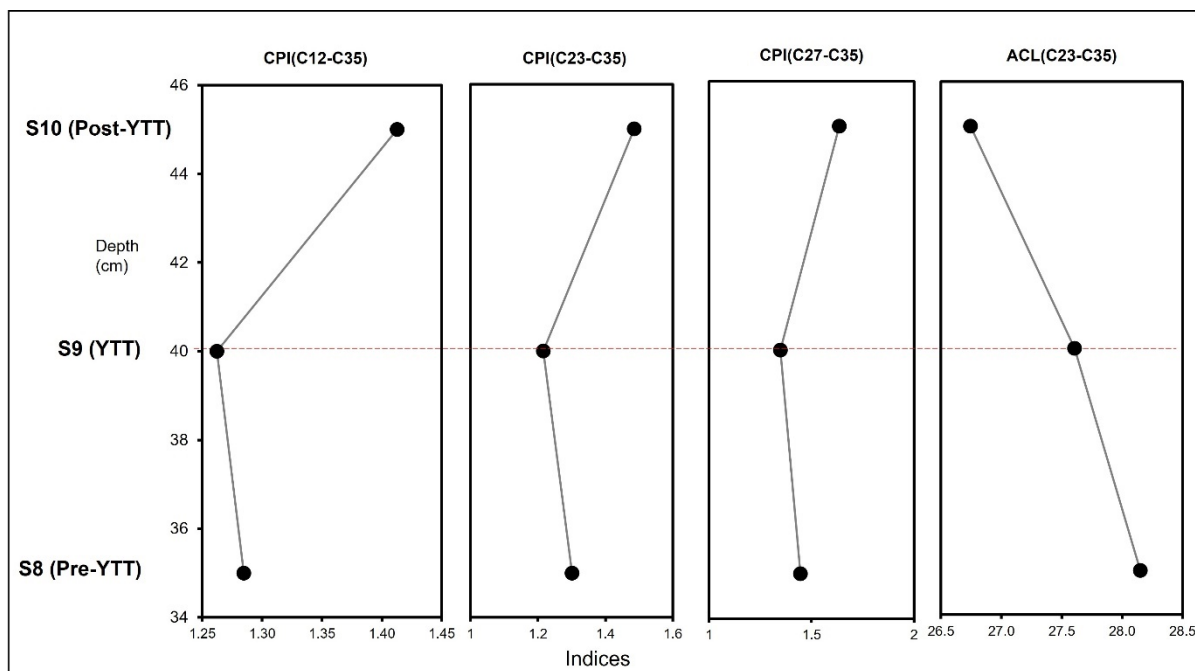
Figure 3.33. Carbon preference index and Average chain length values of Tejpor. CPI values of post-YTT phase is slightly positive than previous phases. Dotted red line marks the YTT event.

Similar CPI trend is also observed in Jwalpuram, indicating shift in terrestrial source (aquatic plants in particular). ACL values (fig. 3.33) of Tejpor shows reducing trend, ranging from 28.15 – 26.74. ACL cannot be inferred as signature of environmental change as shift in homologue preferences is dependent on several factors [57,121].

Aquatic plant and terrestrial plant ratio provide crucial information regarding environmental shift. P.aq values of Tejpor ranges from 0.51 to 0.66 where post-YTT phase has highest value of 0.66 suggesting higher contribution of submerged aquatic plants[122,127,128]. Pre-YTT and YTT phase are showing the signatures of emergent aquatic plants. Inverse Paq. of Tejpor falls in the category of 2.3 to 3.9 where post-YTT phase has highest 1/Paq. value of 3.92. Inverse Paq. data compliments P.aq. data and suggesting mixed vegetation which is predominated by aquatic plants[127]. Emergent aquatic plants were more prominent during YTT and pre-YTT phase, it gradually reduces during post-YTT phase which is dominated by submerged and floating aquatic plants[122]. Higher relative intensity of C_{21} confirms the drastic increase in algal population[57]. It is possible that aquatic system in Tejpor was becoming more eutrophic which is also complimented by sharp increase in short-chain alkanes suggesting higher contribution of microbial community[61,131].

Pwax.. values of Tejpor falls in the range of 0.55 to 0.96 where post-YTT phase lowest value of 0.55. Pre-YTT and YTT phase was pre-dominated by emergent macrophytes, also confirmed by Paq. and 1/Paq. profile. Post-YTT phase in Tejpor experienced certain degree of shift in

vegetation, showing dominance of the submerged or floating aquatic plants[121,122,127]. It is further compliment by terrigenous aquatic ratio (TAR). TAR values of Tejpor falls in the category of 0.63 to 1.85. Pre-YTT and YTT phase indicate a higher contribution of terrestrial sources, mostly contributed by emergent and sub-emergent aquatic plants. Sharp fall in TAR values is observed during post-YTT phase suggesting dominance of aquatic sources, mostly contributed by algal and other submerged aquatic plant communities[122].
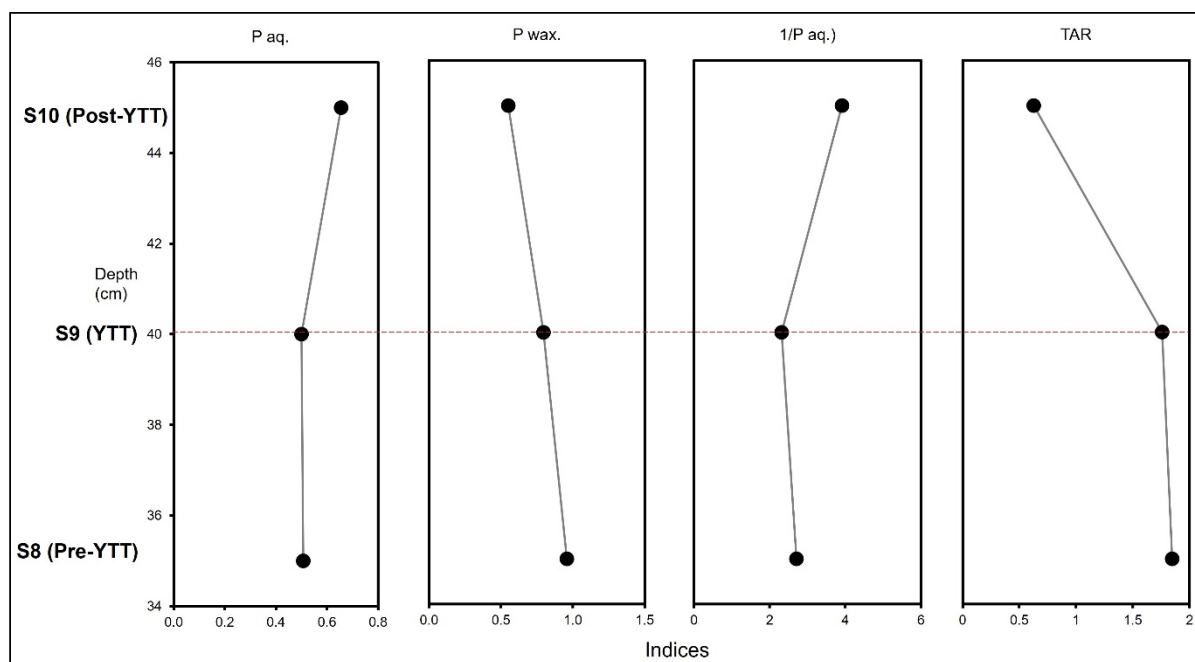
Figure 3.34: Plot of Paq., Pwax.., 1/Paq. and TAR of Tejpor showing ratio between aquatic and terrestrial sources. Paq. and Pwax.. explains the contribution of aquatic and non-aquatic plants, inversely proportionate to each other.

Different n-alkanes are compared to distinguish the different sources of soil organic matter. C_{27}, C_{29} and C_{31} are long-chain n-alkanes, their ratio defines the nature of source whether it is biogenic or not. All the value of C_{29}/C_{31} and C_{27}/C_{31} ratio fall in category of 1 and 1.7 suggesting biogenic source[126]. C_{23}/C_{29} ratio show the higher contribution of vascular plants, mostly contributed by the aquatic ones. Rapid increase in C_{23}/C_{29} during post-YTT phase shows the Tejpor is dominated by submerged macrophytes and floating aquatic plants[122,127]. Certain signatures of environmental weakening are also noticed in $\Sigma(C_{24}-C_{35})/\Sigma(C_{14}-C_{21})$ ratio. $\Sigma(C_{24}-C_{35})/\Sigma(C_{14}-C_{21})$ defines the character of the source based on spatial parameters, whether it is allochthones (terrestrial sourced) or autochthones (sourced from microbial and algae communities). All the $\Sigma(C_{24}-C_{35})/\Sigma(C_{14}-C_{21})$ ratio values of Tejpor are less than two suggesting autochthonous nature of the source. Drastic reduction in catchment are less than two suggesting

autochthonous nature of the source suggesting higher contribution of microbial and algal populations[129].
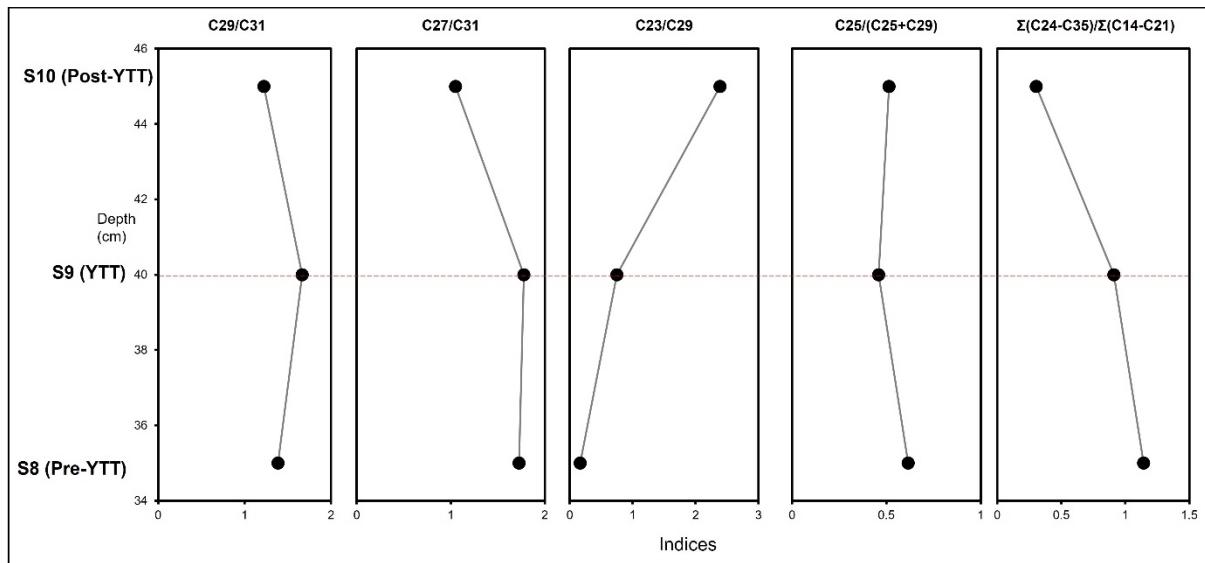
Figure 3.35: Different *n*-alkane ratio of Tejpor, exhibiting differences in sources and explaining contribution of mid-chain and long-chain n-alkanes. Dotted red line marks YTT event.

Chapter IV

Inferences and conclusion

Current investigation employs multi-proxy approach to understand the impact of ~74 ka Toba super eruption on local and regional environmental of South Asia. Two sites (i.e., Jwalapuram and Tejpor) with distinct geographical settings show spatial variability in the environmental impact of ~74 ka Toba although ecologically they share several similarities. However, it is critical that both sites are evaluated independently, shouldn't compared on direct or linear basis due to differences in chronological resolution. Although, both sites show significant immediate impact of ~74ka Toba eruption as reflected by leaf-wax biomarkers.

4.1. Jwalapuram

Jwalapuram represents mosaic environmental conditions characterised by tropical savannah or woody-grassland like vegetation settings[132,133]. Paleolandcape of Jwalapuram may have experienced severe environmental transition although its mosaic conditions[45,132,133] and constant availability of resources makes it hospitable and habitable for past hominin population as reflected in the long hominin occupation record[18,19,134,135]. It is crucial to assess the role and impact of ~74 ka Toba eruption in human-environmental relationship in Jwalapuram. For deeper understanding, different signatures of environmental changes reflected in the multi-proxy record of Jwalapuram is discuss below.

- Leaf-wax biomarker

    It is one of the most significant paleoenvironmental proxy. Most of ratios based on n-alkane distribution suggest remarkable environmental changes occurred in Jwalapuram after Toba ashfall. Proxies like TAR, Paq. and mid-chain n-alkane distribution confirms and proves the idea that Jwalapuram had active lacustrine/marshy conditions as argued by previous researchers[23,69,132,133]. The possible wetland was active during YTT ashfall, verifies the fact that YTT was deposited in aqueous environment[24]. Distribution of long-chain n-alkanes, TAR, Paq., and Pwax. suggest sharp shift in terrestrial source during YTT (SS6) and post-YTT phase (MS2 and MS5). It seems nature of paleovegetation shifted from emergent aquatic plants to submerged aquatic plants[122,125]. Drastic increase in C_{23} shows rising population of *Sphagnum* mosses[118] suggesting water-logged condition[136]. Transformation of Jwalapuram landscape from fluvial oriented wetland-marshy conditions[23,133] to water-logged environment is an indicator of environmental deterioration during post-YTT phase. Cyclical deposition of reworked ash deposits

indicates relatively rapid removal of the YTT from upland areas, swamping and choking the Jurreru Valley and smoothing the ponded topography[133]. Thick deposits of volcanic ash may have buried most of the plantscape causing rapid deforestation[23] and hydrological contamination[69]. Predominance of *Sphagnum* mosses[119] during post-YTT phase support that fact that landscape experienced rapid swamping and water logging[1]. Hence, leaf-wax biomarker data suggest the strong possibility that Jurreru valley may have faced severe immediate impact of ~74ka Toba eruption.

- Paleopedological proxies (based on ED-XRF and XRD analysis)

Jwalapuram palaeosol sequence yield multiple elemental and mineralogical signatures also narrate the episodes of environmental deterioration during post-YTT phase. Elemental proxies based of ED-XRF spectrometry suggest higher mobility among base elements (fig. 3.8 and 3.9). Mobility among these base elements is mostly caused due to chemical weathering[50,52,54] of tuff components, led to formation of new sequioxides[107]. Chemical weathering is occurring in oscillatory manner, it reduces during the redeposition of YTT (SS stratums) and sharply increases at the end of every YTT redeposition cycle suggesting wetter environment during SS stratums and drier during MS stratums. These oscillating conditions are evident in different paleopedological proxies (fig. 3.10, 3.15a, 3.16). These proxies shows strong signature of low temperature dolomite that is a prime indicator of environmental aridification[102]. Due to changes in chemical processes, elements like- Ca and Mg dissolves and precipitates, forms finer pale greyish hardpans (MS stratums) predominated by dolomitic compounds (fig. 3.14, 3.15, and 3.15a) which is at highest during MS5 suggesting period of severe aridity. Interestingly, similar signature is also observed at pre-Toba stratum (SS7). SS7 shows higher LOI and formation of dolomite during its formation, pointing towards the initiation of arid environmental conditions prior to Toba eruption. Earlier $\delta^{13}C_{org.}$ and $\delta^{13}C_{pdb}$ data suggest that Jwalapuram had drier environmental conditions prior to YTT ashfall, showing local terrestrial signature of global GI-20S arid phase[45,133]. It is complemented by different paleopedological proxies discussed in chapter III (fig. 3.15, 3.15a, 3.16). Although, YTT seems to have amplified the aridification of environmental conditions and led to the vegetation shift (what is noticed in current leaf-wax biomarker data). However, sedimentary environment get steady and stable during SS1 and SSO suggesting conditions may have recovered radily[23]. Sharp transitions in elemental, and mineralogical profile suggest that
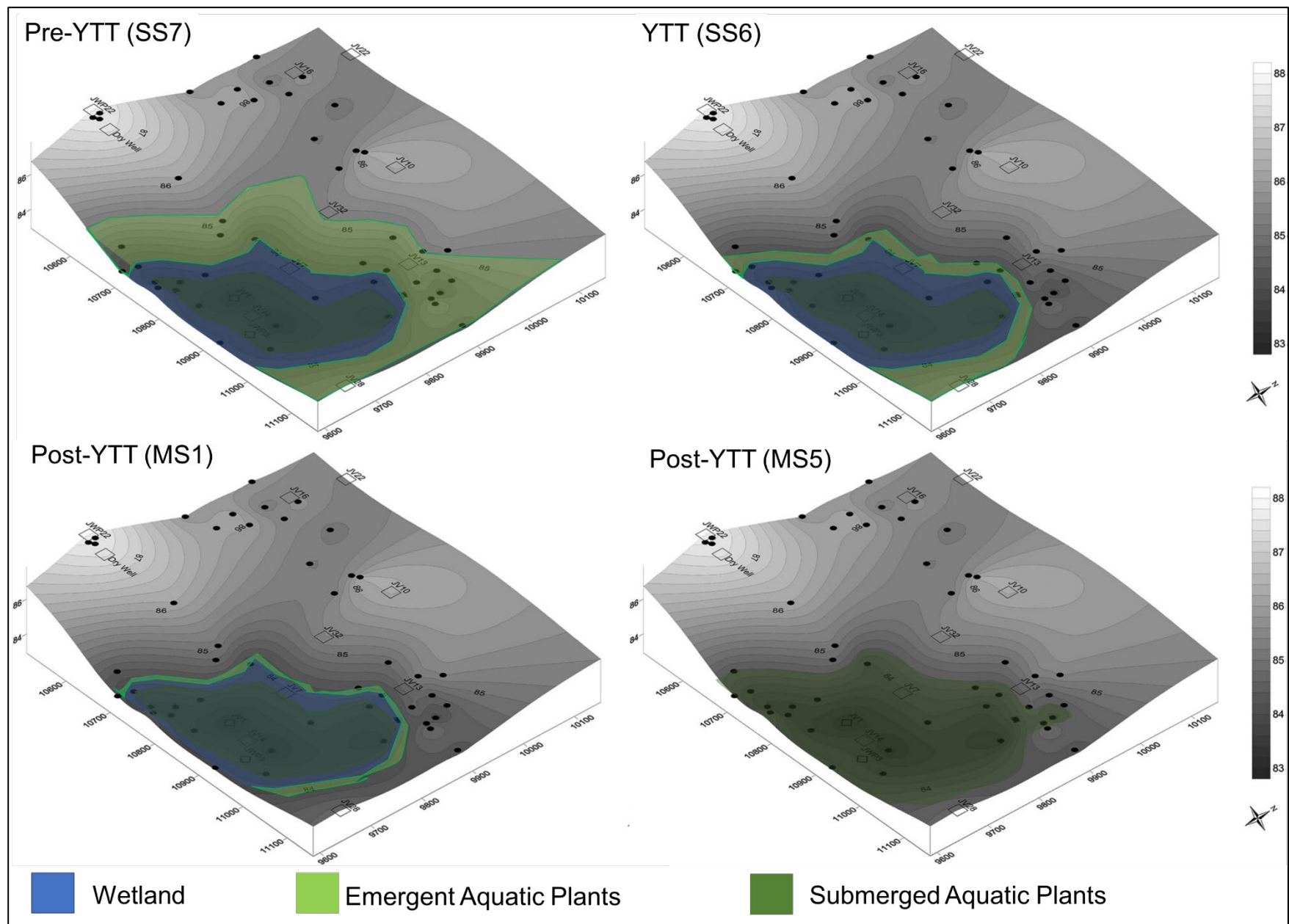
Figure 4.1: Hypothetical paleovegetation settings of Jwalapuram based on leaf-wax biomarker data. As CPI ($C_{12} - C_{35}$) value suggested that Jwalapuram had very minimal or no contribution or terrestrial high plants. It is dominated by aquatic plant sources. Paq. and Pwax. ratio highlighted the shift from emergent aquatic plants to submerged aquatic plants. Remarkable increase in C23 during MS5 show higher contribution of *Sphagnum* mosses plants. DEM models suggest low-lying regions of Jwalapuram may have converted into swampy water-logged environment during MS5. DEM data is modified from Blinkhorn *et. al.* 2012.

the sediment sequence in Jwalapuram may represents the seasonal environmental variation rather than decadal or millennial. However, current research suggest that Jwalapuram may have faced severe immediate impact of YTT eruption. We also know the fact that Hominin populations were living in the Jurreru valley till very moment of YTT ashfall[45]. It is quite probably that Hominins have continued occupying the higher margins of Jurreru valley that are less affected by YTT deposition[45,133]. As Blinkhorn et al. pointed out that the Jurreu valley have highly heterogenous paleovegetation suggesting mosaic environmental conditions[1,132]. It must have provided ample amount of resources to past hominin population particularly during the YTT event[1].

4.2. Tejpor

Like Jwalapuram, Tejpor also represents dry ecosystem. Region is dominated by dry tropical woodland, typical of Indian deciduous zones of India[113]. Regional conditions tend to get drier during arid phases (such as MIS 4 or LGM), shifting to sub-desert or savannah like vegetation[113]. Tejpor has scarce record of environmental and palaeolithic research. However, adjoining regions of Orsang, Sukhi, and Sabarmati basin continuously occupied hominin population[137,138]. Current investigation presents novel evidence of environmental impact of ~74 ka Toba eruption on the local environment of Tejpor. Environmental signature based on multiple organic and inorganic proxies are discussed below.

- Leaf-wax biomarker analysis

  According to leaf-wax biomarker analysis, Tejpor was an active riverine system as suggested by Paq. and mid-chain *n*-alkanes distribution[122]. Pre-YTT environmental conditions in Tejpur is open and relatively wet than post-YTT environment. CPI (C_{12} – C_{35}) and Pwax. values suggest lesser contribution of terrestrial high plants. Paq. profile suggest transition within aquatic plants, shifting from emergent aquatic macrophytes to submerged aquatic plants and mosses. It could be possible signature of environmental change due to YTT event.

- Paleopedological proxies (based on ED-XRF and XRD analysis)

  Tejpor shows mosaic of paedogenic feature, suggesting relatively balanced environmental conditions. There are two signals of environmental changes were noticed, one at pre-YTT (S4) and other after YTT ashfall. These changes are complimented by most of inorganic proxies (fig. 3.19 and 3,20). These phases are highlighted by rise in relative intensity of base elements, LOI, and weathering indices

(such as BA, and WIP). However, most of these pedological changes are not very severe suggesting steady and stable environment.

Limitation of current research

Sample set used for leaf-wax biomarker analyses is very small and it unable to explore the spatial diversity of mosaic environmental conditions[132]. It is crucial that Pre-YTT, YTT and post-YTT samples should be analysed at varying gradient to understand the altimetric variation within paleovegetation. Another crucial problem with current leaf-wax biomarker data is absence of diagenetic data. Different homologues of *n*-alkanes are susceptible to diagenetic alteration that can severe impact the pattern of *n*-alkane distribution[57,59,68]. Employment of compound-specific isotope of *n*-alkanes can be an important tool to assess the sourcing of OM in much refined way.

It is important to acknowledge that paleopedological proxies are based on XRF elemental data that has certain degree of error due to the problem in sampling protocol. However, all sample are analysed in same conditions and results shows mirroring trends which can be further supported by XRD data. Nevertheless, it is important that XRF analysis is revised as per standardized protocol[139].

4.3. Conclusion

Current investigation has highlighted certain crucial factors. It is important to understand that high temporal resolution is necessary to understand the immediate impact of such massive event. Multi-proxy environmental data from both site portrays local environment suffered immediate severe impact as it is manifested in most on the environmental proxies. However, the inability to correlate both sequences on temporal grounds restrict us to explain the immediate span of the impact. Although multiple environmental proxies at Tejpor show that conditions were relatively arid for span of ~10ka. However, nature of environmental shift is not that severe. Current study and recent investigations[20] have successfully demonstrated that ~74 ka Toba event had a highly variable environmental impact. However, it is important to highlight that impact was remarkable that it may have forced past human population to change their subsistence system[140,141]. Although, recent evidence of Dhaba showed cultural continuity suggesting no change in human behaviour[25].
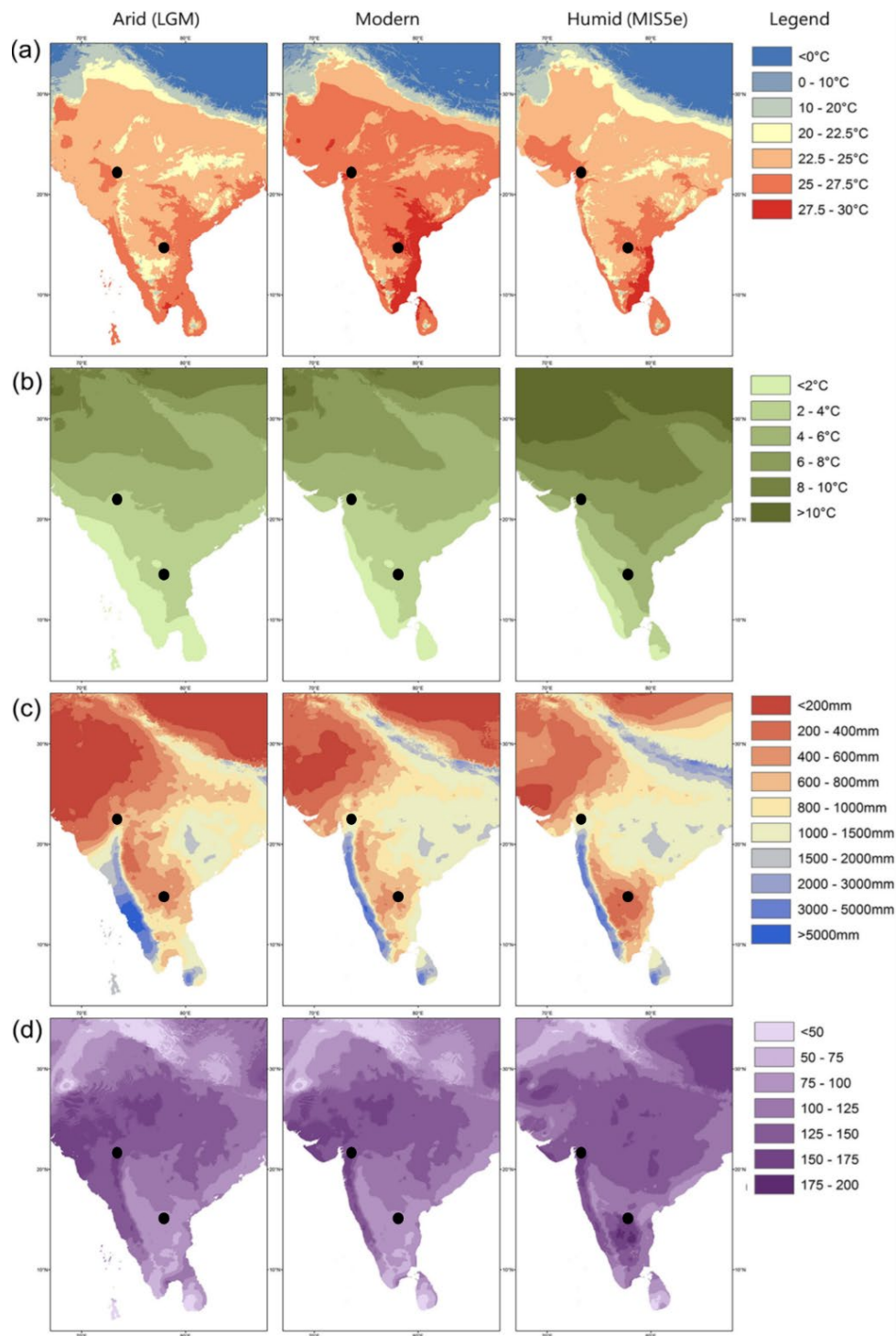
Figure 4.1. Patterns of climate variability affecting South Asia during the Last Glacial Maximum (LGM) (left), modern conditions (centre) and MIS5e (right) with a location Tejpor on west and Jwalapuram on South-east. Image illustrates (a) mean annual temperature and (b) its standard deviation, and (c) annual precipitation and (d) its coefficient of variance. This indicates that although climate change is likely to have modulated temperatures, the impact of this is likely to have been limited in contrast to variability in precipitation. Significant decrease in precipitation is observed over the LGM, which is likely to be comparable to other phases of suppressed monsoonal intensity, particularly affecting western and central India. Increased seasonal variability in precipitation during MIS 5e probably indicates stronger summer monsoon rainfall, particularly affecting western and north-central India. (Image courtesy: Patrick Roberts).

South Asian mosaics appears to have provided a constant diversity and availability of natural resources making it a sustainable region for the long survival of humans[1]. Different basins (such as Jurreru basin) act as hospitable refugia, away from the impact of climatic stress (like Toba eruption) leading to the formation of centre of cultural evolution[3,142]. Multiple phases of human habitation at Jwalapuram advocates the fact that it may have been one of the cultural innovation centers[143]. Late persistence of megafauna populations[144] and no major changes in many faunal population over the last 200,000 years[145,146] suggest high degree of continuity among faunal populations which is attributed to interconnected mosaic habitats, and stability in topography and precipitation(fig. 4.2)[1]. Late survival of archaic hominin population also compliment the fact that oriental realm of South Asia is an everlasting hospitable zone harbouring unimaginable amount of biodiversity[147]. As Black *et. al.* suggested that India may have been a geographical refugium that have supported the subsistence of past human population[20]. It is quite unlikely that ~74ka Toba caused human extinction or climate havoc in South Asia[12,15,20,25,45]. Although event such as Toba eruption is massive[21] and may have affect extreme biogeographical zones of South Asia such as Thar desert and Trans-Himalayan zone[148]. Hence, it is important to ask at what extent, Toba eruption and caused climatic fluctuations and environmental instability contributed to behavioural evolution in South Asia.

Now it is crucial to expand the size of dataset and analyses different YTT sequence at higher resolution by employing leaf-wax biomarkers and compound-specific isotopes along with paleopedological proxies. Use of aforementioned technique will allow us characterize past-vegetation, water-landscape and paedogenic environment and how it is varying through-out the chronology. Current investigation demonstrate the potentiality of such investigation and how it is crucial for understanding the key questions of Human evolution[147,149]. However, understanding regional climate response is necessary and of paramount significance, especially for relating global volcanic perturbations to proxies for local- to regional-scale climate, to understand temporal changes in climate relevant to hominin evolution and migration, and to inform estimates of the climate effects of large-scale sulfur release and global-cooling from future explosive eruptions[20].

References

1. Roberts, P., Blinkhorn, J. & Petraglia, M. D. A transect of environmental variability across South Asia and its influence on Late Pleistocene human innovation and occupation. *J. Quat. Sci.* **33**, 285–299 (2018).

2. Groucutt, H. S. *et al.* Multiple hominin dispersals into Southwest Asia over the past 400,000 years. *Nature* **597**, 376–380 (2021).

3. Blinkhorn, J. & Petraglia, M. D. Environments and cultural change in the Indian Subcontinent: implications for the dispersal of Homo sapiens in the Late Pleistocene. *Curr. Anthropol.* **58**, S463–S479 (2017).

4. Raza, W. *et al.* Indian summer monsoon variability in southern India during the last deglaciation: Evidence from a high resolution stalagmite δ18O record. *Palaeogeogr. Palaeoclimatol. Palaeoecol.* **485**, 476–485 (2017).

5. Allu, N. C. *et al.* Stalagmite δ18O variations in southern India reveal divergent trends of Indian Summer Monsoon and East Asian Summer Monsoon during the last interglacial. *Quat. Int.* **371**, 191–196 (2015).

6. Rampino, M. R. & Ambrose, S. H. Volcanic winter in the Garden of Eden: The Toba supereruption and the late Pleistocene human population crash. *Spec. Pap. Geol. Soc. Am.* **345**, 71–82 (2000).

7. Ambrose, S. H. Did the super-eruption of Toba cause a human population bottleneck? Reply to Gathorne-Hardy and Hartcourt-Smith. *J. Hum. Evol.* **45**, 231–237 (2003).

8. Williams, M. A. J. *et al.* Environmental impact of the 73 ka Toba super-eruption in South Asia. *Palaeogeogr. Palaeoclimatol. Palaeoecol.* **284**, 295–314 (2009).

9. Harpending, H. C., Sherry, S. T., Rogers, A. R. & Stoneking, M. The Genetic Structure of Ancient Human Populations. *Curr. Anthropol.* **34**, 483–496 (1993).

10. Ambrose, S. H. Late Pleistocene human population bottlenecks, volcanic winter, and differentiation of modern humans. *J. Hum. Evol.* **34**, 623–651 (1998).

11. Zielinski, G. A. *et al.* Potential atmospheric impact of the Toba mega-eruption ~71,000 years ago. *Geophys. Res. Lett.* **23**, 837–840 (1996).

12. Ge, Y. & Gao, X. Understanding the overestimated impact of the Toba volcanic super-

eruption on global environments and ancient hominins. *Quat. Int.* **559**, 24–33 (2020).

13. Jackson, L. J., Stone, J. R., Cohen, A. S. & Yost, C. L. High-resolution paleoecological records from Lake Malawi show no significant cooling associated with the Mount Toba supereruption at ca. 75 ka. *Geology* **43**, 823–826 (2015).

14. Smith, E. I. *et al.* Humans thrived in South Africa through the Toba eruption about 74,000 years ago. *Nature* **555**, 511–515 (2018).

15. Petraglia, M. *et al.* Middle paleolithic assemblages from the Indian subcontinent before and after the Toba super-eruption. *Science (80-.).* **317**, 114–116 (2007).

16. Yost, C. L., Jackson, L. J., Stone, J. R. & Cohen, A. S. Subdecadal phytolith and charcoal records from Lake Malawi, East Africa imply minimal effects on human evolution from the ∼74 ka Toba supereruption. *J. Hum. Evol.* **116**, 75–94 (2018).

17. Lane, C. S., Chorn, B. T. & Johnson, T. C. Ash from the Toba supereruption in Lake Malawi shows no volcanic winter in East Africa at 75 ka. *Proc. Natl. Acad. Sci. U. S. A.* **110**, 8025–8029 (2013).

18. Petraglia, M. *et al.* After the Toba Super-Eruption. *Science (80-.).* **317**, 114–116 (2007).

19. Petraglia, M. D., Ditchfield, P., Jones, S., Korisettar, R. & Pal, J. N. The Toba volcanic super-eruption, environmental change, and hominin occupation history in India over the last 140,000 years. *Quat. Int.* **258**, 119–134 (2012).

20. Black, B. A., Lamarque, J. F., Marsh, D. R., Schmidt, A. & Bardeen, C. G. Global climate disruption and regional climate shelters after the Toba supereruption. *Proc. Natl. Acad. Sci. U. S. A.* **118**, 1–8 (2021).

21. Costa, A., Smith, V. C., Macedonio, G. & Matthews, N. E. The magnitude and impact of the Youngest Toba Tuff super-eruption. *Front. Earth Sci.* **2**, 1–8 (2014).

22. Williams, M. The ~73 ka Toba super-eruption and its impact: History of a debate. *Quat. Int.* **258**, 19–29 (2012).

23. Jones, S. C. Palaeoenvironmental response to the ∼74 ka Toba ash-fall in the Jurreru and Middle Son valleys in southern and north-central India. *Quat. Res.* **73**, 336–350 (2010).

24. Jones, S. C. The Toba supervolcanic eruption: Tephra-fall deposits in India and paleoanthropological implications. *Vertebr. Paleobiol. Paleoanthropology* 173–200 (2007) doi:10.1007/1-4020-5562-5_8.

25. Clarkson, C. *et al.* Human occupation of northern India spans the Toba super-eruption ~74,000 years ago. *Nat. Commun.* **11**, (2020).

26. Simkin, T., Siebert, L. & Sigurdsson, H. Earth's volcanoes and eruptions: An overview. *Encycl. volcanoes* 249–262 (2000).

27. Mason, B. G., Pyle, D. M. & Oppenheimer, C. The size and frequency of the largest explosive eruptions on Earth. *Bull. Volcanol.* **66**, 735–748 (2004).

28. Chesner, C. A. & Rose, W. I. Stratigraphy of the Toba tuffs and the evolution of the Toba caldera complex, Sumatra, Indonesia. *Bull. Volcanol.* **53**, 343–356 (1991).

29. Mark, D. F. *et al.* A high-precision 40Ar/39Ar age for the Young Toba Tuff and dating of ultra-distal tephra: Forcing of Quaternary climate and implications for hominin occupation of India. *Quat. Geochronol.* **21**, 90–103 (2014).

30. Rose, W. I. & Chesner, C. A. Dispersal of ash in the great Toba eruption, 75 ka. *Geology* **15**, 913–917 (1987).

31. Chesner, C. A. Petrogenesis of the Toba Tuffs, Sumatra, Indonesia. *J. Petrol.* **39**, 397–438 (1998).

32. Chesner, C. A. The Toba Caldera Complex. *Quat. Int.* **258**, 5–18 (2012).

33. Schulz, H., Emeis, K. C., Erlenkeuser, H., von Rad, U. & Rolf, C. The Toba volcanic event and interstadial/stadial climates at the marine isotopic stage 5 to 4 transition in the Northern Indian Ocean. *Quat. Res.* **57**, 22–31 (2002).

34. Acharyya, S. K. & Basu, P. K. Toba ash on the indian subcontinent and its implications for correlation of late pleistocene alluvium. *Quaternary Research* vol. 40 10–19 (1993).

35. Westgate, J. A. *et al.* All Toba tephra occurrences across peninsular India belong to the 75 000 yr BP eruption. *Quat. Res.* **50**, 107–112 (1998).

36. Neudorf, C. M., Roberts, R. G. & Jacobs, Z. Assessing the time of final deposition of Youngest Toba Tuff deposits in the Middle Son Valley, northern India. *Palaeogeogr.*

Palaeoclimatol. Palaeoecol. **399**, 127–139 (2014).

37. Biswas, R. H., Williams, M. A. J., Raj, R., Juyal, N. & Singhvi, A. K. Methodological studies on luminescence dating of volcanic ashes. *Quat. Geochronol.* **17**, 14–25 (2013).

38. Rogers, A. R. & Jorde, L. B. Genetic evidence on modern human origins. *Hum. Biol.* 1–36 (1995).

39. Timmermann, A. & Friedrich, T. Late Pleistocene climate drivers of early human migration. *Nature* **538**, 92–95 (2016).

40. Westaway, K. E. *et al.* An early modern human presence in Sumatra 73,000–63,000 years ago. *Nature* **548**, 322–325 (2017).

41. Sieveking, A. The Palaeolithic Industry of Kota Tampan, Perak, Northwestern Malaya. *Asian Perspect.* **2**, 91–102 (1958).

42. Majid, Z. & Tjia, H. D. Kota Tampan, Perak: The geological and archaeological evidence for a late Pleistocene site. *J. Malays. Branch R. Asiat. Soc.* **61**, 123–134 (1988).

43. Louys, J. Mammal community structure of Sundanese fossil assemblages from the Late Pleistocene, and a discussion on the ecological effects of the Toba eruption. *Quat. Int.* **258**, 80–87 (2012).

44. Louys, J. Limited effect of the Quaternary's largest super-eruption (Toba) on land mammals from Southeast Asia. *Quat. Sci. Rev.* **26**, 3108–3117 (2007).

45. Haslam, M. *et al.* A southern Indian Middle Palaeolithic occupation surface sealed by the 74 ka Toba eruption: Further evidence from Jwalapuram Locality 22. *Quat. Int.* **258**, 148–164 (2012).

46. Balter, M. Of two minds about toba's impact. *Science (80-.).* **327**, 1187–1188 (2010).

47. Raj, R. Occurrence of volcanic ash in the quaternary alluvial deposits, lower Narmada basin, western India. *J. Earth Syst. Sci.* **117**, 41–48 (2008).

48. Babechuk, M. G., Widdowson, M. & Kamber, B. S. Quantifying chemical weathering intensity and trace element release from two contrasting basalt profiles, Deccan Traps, India. *Chem. Geol.* **363**, 56–75 (2014).

49.   Sheldon, N. D. & Tabor, N. J. Quantitative paleoenvironmental and paleoclimatic reconstruction using paleosols. *Earth-Science Rev.* **95**, 1–52 (2009).

50.   Harnois, L. The CIW index: A new chemical index of weathering. *Sediment. Geol.* **55**, 319–322 (1988).

51.   Lu, S., Wang, S. & Chen, Y. Palaeopedogenesis of red palaeosols in Yunnan Plateau, southwestern China: Pedogenical, geochemical and mineralogical evidences and palaeoenvironmental implication. *Palaeogeogr. Palaeoclimatol. Palaeoecol.* **420**, 35–48 (2015).

52.   Price, J. R. & Velbel, M. A. Chemical weathering indices applied to weathering profiles developed on heterogeneous felsic metamorphic parent rocks. *Chem. Geol.* **202**, 397–416 (2003).

53.   Osipov, S. *et al.* The Toba supervolcano eruption caused severe tropical stratospheric ozone depletion. *Commun. Earth Environ.* **2**, 1–7 (2021).

54.   Nesbitt, Hw. & Young, G. M. Early Proterozoic climates and plate motions inferred from major element chemistry of lutites. *Nature* **299**, 715–717 (1982).

55.   Berke, M. A. *et al.* Characterization of the last deglacial transition in tropical East Africa: Insights from Lake Albert. *Palaeogeogr. Palaeoclimatol. Palaeoecol.* **409**, 1–8 (2014).

56.   Meyers, P. A. Organic geochemical proxies of paleoceanographic. *Org. Geochem.* **27**, 213–250 (1997).

57.   Berke, M. A. *Reconstructing terrestrial paleoenvironments using sedimentary organic biomarkers*. *Vertebrate Paleobiology and Paleoanthropology* (Springer International Publishing, 2018). doi:10.1007/978-3-319-94265-0_8.

58.   Eglinton, T. I. & Eglinton, G. Molecular proxies for paleoclimatology. *Earth Planet. Sci. Lett.* **275**, 1–16 (2008).

59.   Patalano, R., Roberts, P., Boivin, N., Petraglia, M. D. & Mercader, J. Plant wax biomarkers in human evolutionary studies. *Evol. Anthropol.* 1–14 (2021) doi:10.1002/evan.21921.

60.   Eglinton, G. & Hamilton, R. J. The distribution of alkanes. *Chem. plant Taxon.* **187**,

217 (1963).

61. Zhang, Z., Zhao, M., Eglinton, G., Lu, H. & Huang, C. Y. Leaf wax lipids as paleovegetational and paleoenvironmental proxies for the Chinese Loess Plateau over the last 170 kyr. *Quat. Sci. Rev.* **25**, 575–594 (2006).

62. Meyers, P. A. Applications of organic geochemistry to paleolimnological reconstructions: a summary of examples from the Laurentian Great Lakes. *Org. Geochem.* **34**, 261–289 (2003).

63. Bray, E. E. & Evans, E. D. Distribution of n-paraffins as a clue to recognition of source beds. *Geochim. Cosmochim. Acta* **22**, 2–15 (1961).

64. Andrea, B. Bulk geochemical, biomarker and leaf wax isotope records of Mfabeni peatland, KwaZulu Natal, South Africa since the late Pleistocene. (2016).

65. Jaffé, R., Mead, R., Hernandez, M. E., Peralba, M. C. & DiGuida, O. A. Origin and transport of sedimentary organic matter in two subtropical estuaries: a comparative, biomarker-based study. *Org. Geochem.* **32**, 507–526 (2001).

66. Bourbonniere, R. A. & Meyers, P. A. Sedimentary geolipid records of historical changes in the watersheds and productivities of Lakes Ontario and Erie. *Limnol. Oceanogr.* **41**, 352–359 (1996).

67. Georgiou, C. D. *et al.* Evidence for photochemical production of reactive oxygen species in desert soils. *Nat. Commun.* **6**, 1–11 (2015).

68. Häggi, C., Zech, R., Mcintyre, C. & Eglinton, T. On the stratigraphic integrity of leaf-wax biomarkers in loess-paleosols. *Biogesciences Discuss.* **10**, 16903–16922 (2013).

69. Jones, S. C. A Human Catastrophe? The impact of the ~74,000 year-old supervolcanic eruption of Toba on hominin populations in India. *Unpubl. PhD thesis, Dep. Archaeol.* **II**, (2007).

70. Srivastava, A. K., Singh, A., Sharma, N. & Khare, N. Weathering pattern of Youngest Toba Tuff, Purna alluvial basin, Central India. *Arab. J. Geosci.* **13**, (2020).

71. Krishnan, G. & Achyuthan, H. Incipient Weathering of the ~74ka Young Toba Tuff (YTT) Biotite Grains, Sagileru Valley, Andhra Pradesh. *J. Geol. Soc. India* **94**, 573–578 (2019).

72. Retallack, G. J. Palaeosols in the upper Narrabeen Group of New South Wales as evidence of Early Triassic palaeoenvironments without exact modern analogues. *Aust. J. Earth Sci.* **44**, 185–201 (1997).

73. Retallack, G. J. Neogene expansion of the North American prairie. *Palaios* **12**, 380–390 (1997).

74. Retallack, G. J. Early forest soils and their role in Devonian global change. *Science (80-.).* **276**, 583–585 (1997).

75. Hamer, J. M. M., Sheldon, N. D. & Nichols, G. J. Global aridity during the Early Miocene? A terrestrial paleoclimate record from the Ebro Basin, Spain. *J. Geol.* **115**, 601–608 (2007).

76. Grant, K. M. *et al.* A 3 million year index for North African humidity/aridity and the implication of potential pan-African Humid periods. *Quat. Sci. Rev.* **171**, 100–118 (2017).

77. Song, B., Ji, J., Wang, C., Xu, Y. & Zhang, K. Intensified aridity in the Qaidam Basin during the Middle Miocene: constraints from ostracod, stable isotope, and weathering records. *Can. J. Earth Sci.* **54**, 242–256 (2017).

78. Felton, A. A. *et al.* Paleolimnological evidence for the onset and termination of glacial aridity from Lake Tanganyika, Tropical East Africa. *Palaeogeogr. Palaeoclimatol. Palaeoecol.* **252**, 405–423 (2007).

79. Bokhorst, M. P. *et al.* Pedo-chemical climate proxies in Late Pleistocene Serbian–Ukranian loess sequences. *Quat. Int.* **198**, 113–123 (2009).

80. Dong, G., Xia, Z., Elston, R., Sun, X. & Chen, F. Response of geochemical records in lacustrine sediments to climate change and human impact during middle Holocene in Mengjin, Henan Province, China. *Front. Earth Sci. China* **3**, 279–285 (2009).

81. Liu, S. *et al.* Reconstruction of monsoon evolution in southernmost Sumatra over the past 35 kyr and its response to northern hemisphere climate changes. *Prog. Earth Planet. Sci.* **7**, 1–13 (2020).

82. Dill, H. Terrestrial ferromanganese ore concentrations from mid-european basement blocks and their implication concerning the environment of formation during the late cenozoic (northern Bavaria, F.R.G.). *Sediment. Geol.* **45**, 77–96 (1985).

83. Fantasia, A., Adatte, T., Spangenberg, J. E. & Font, E. Palaeoenvironmental changes associated with Deccan volcanism, examples from terrestrial deposits from Central India. *Palaeogeogr. Palaeoclimatol. Palaeoecol.* **441**, 165–180 (2016).

84. Leroux, A. *et al.* Late Glacial-Holocene sequence of Lake Saint-Point (Jura Mountains, France): Detrital inputs as records of climate change and anthropic impact. *Comptes Rendus Geosci.* **340**, 883–892 (2008).

85. Hajdas, I. & Ochs, S. I. 10. Quaternary environments: landscapes, climate, ecosystems, human activity during the past 2.6 million years.

86. Ding, F. & Ding, Z. Chemical weathering history of the southern Tajikistan loess and paloclimate implications. *Sci. China Ser. D Earth Sci.* **46**, 1012–1021 (2003).

87. Qiao, Y. *et al.* Intensification of aridity in the eastern margin of the Tibetan plateau since 300 ka BP inferred from loess-soil sequences, western Sichuan Province, Southwest China. *Palaeogeogr. Palaeoclimatol. Palaeoecol.* **414**, 192–199 (2014).

88. Yang, S., Ding, F. & Ding, Z. Pleistocene chemical weathering history of Asian arid and semi-arid regions recorded in loess deposits of China and Tajikistan. *Geochim. Cosmochim. Acta* **70**, 1695–1709 (2006).

89. Ruxton, B. P. Measures of the degree of chemical weathering of rocks. *J. Geol.* **76**, 518–527 (1968).

90. Nesbitt, H. W. & Wilson, R. E. Recent chemical weathering of basalts. *Am. J. Sci.* **292**, 740–777 (1992).

91. Derakhshan-Babaei, F. *et al.* Relating the spatial variability of chemical weathering and erosion to geological and topographical zones. *Geomorphology* **363**, 107235 (2020).

92. Smith, V. C. *et al.* Geochemical fingerprinting of the widespread Toba tephra using biotite compositions. *Quat. Int.* **246**, 97–104 (2011).

93. Kaczmarek, S. E., Gregg, J. M., Bish, D. L., Machel, H. G. & Fouke, B. W. Dolomite, very high-magnesium calcite, and microbes— implications for the microbial model of dolomitization. *SEPM Spec. Publ.* **109**, 7–20 (2017).

94. Bar-Matthews, M., Matthews, A. & Ayalon, A. Environmental controls of speleothem

mineralogy in a karstic dolomitic terrain (Soreq Cave, Israel). *J. Geol.* **99**, 189–207 (1991).

95. Yu, K. *et al.* Chemical origin of early Permian saddle dolomites in the Junggar Basin, NW China. *J. Asian Earth Sci.* **184**, 103990 (2019).

96. Al-Aasm, I. Origin and characterization of chemical dolomite in the Western Canada Sedimentary Basin. *J. Geochemical Explor.* **78**, 9–15 (2003).

97. Lovering, T. S. The origin of chemical and low temperature dolomite. *Econ. Geol.* **64**, 743–754 (1969).

98. Nesbitt, H. W. & Young, G. M. Formation and diagenesis of weathering profiles. *J. Geol.* **97**, 129–147 (1989).

99. Kampman, N., Bickle, M., Becker, J., Assayag, N. & Chapman, H. Feldspar dissolution kinetics and Gibbs free energy dependence in a CO2-enriched groundwater system, Green River, Utah. *Earth Planet. Sci. Lett.* **284**, 473–488 (2009).

100. Pacheco, F. A. L. & Szocs, T. "Dedolomitization reactions" driven by anthropogenic activity on loessy sediments, SW Hungary. *Appl. Geochemistry* **21**, 614–631 (2006).

101. Wang, X. *et al.* In-situ high-temperature XRD and FTIR for calcite, dolomite and magnesite: Anharmonic Contribution To The Thermodynamic Properties. *J. Earth Sci.* **30**, 964–976 (2019).

102. Polyak, V. J., Asmerom, Y. & Lachniet, M. S. Rapid speleothem δ13C change in southwestern North America coincident with Greenland stadial 20 and the Toba (Indonesia) supereruption. *Geology* **45**, 843–846 (2017).

103. Ji, J., Ge, Y., Balsam, W., Damuth, J. E. & Chen, J. Rapid identification of dolomite using a Fourier Transform Infrared Spectrophotometer (FTIR): A fast method for identifying Heinrich events in IODP Site U1308. *Mar. Geol.* **258**, 60–68 (2009).

104. Mroczkowska-Szerszeń, M. & Orzechowski, M. Infrared spectroscopy methods in reservoir rocks analysis – semiquantitative approach for carbonate rocks. *Nafta-Gaz* **74**, 802–812 (2018).

105. Gunasekaran, S. & Anbalagan, G. Thermal decomposition of natural dolomite. *Bull. Mater. Sci.* **30**, 339–344 (2007).

106. Jiang, C. L., Zeng, W., Liu, F. S., Tang, B. & Liu, Q. J. First-principles analysis of vibrational modes of calcite, magnesite and dolomite. *J. Phys. Chem. Solids* **131**, 1–9 (2019).

107. Tabor, N. J. & Myers, T. S. Paleosols as indicators of paleoenvironment and paleoclimate. *Annu. Rev. Earth Planet. Sci.* **43**, 333–361 (2015).

108. Beverly, E. J., Lukens, W. E. & Stinchcomb, G. E. Paleopedology as a tool for reconstructing paleoenvironments and paleoecology. in *Methods in paleoecology* 151–183 (Springer, 2018).

109. Snowball, I. F. Geochemical control of magnetite dissolution in subarctic lake sediments and the implications for environmental magnetism. *J. Quat. Sci.* **8**, 339–346 (1993).

110. Shuman, B. Controls on loss-on-ignition variation in cores from two shallow lakes in the northeastern United States. *J. Paleolimnol.* **30**, 371–385 (2003).

111. Heiri, O., Lotter, A. F. & Lemcke, G. Loss on ignition as a method for estimating organic and carbonate content in sediments: reproducibility and comparability of results. *J. Paleolimnol.* **25**, 101–110 (2001).

112. Fereres, S., Lautenberger, C., Fernandez-Pello, C., Urban, D. & Ruff, G. Mass flux at ignition in reduced pressure environments. *Combust. Flame* **158**, 1301–1306 (2011).

113. Chamyal, L. S., Maurya, D. M., Bhandari, S. & Raj, R. Late Quaternary geomorphic evolution of the lower Narmada valley, Western India: implications for neotectonic activity along the Narmada–Son Fault. *Geomorphology* **46**, 177–202 (2002).

114. Juyal, N., Raj, R., Maurya, D. M., Chamyal, L. S. & Singhvi, A. K. Chronology of late Pleistocene environmental changes in the lower Mahi basin, western India. *J. Quat. Sci.* **15**, 501–508 (2000).

115. Bush, R. T. & McInerney, F. A. Variation in n-Alkane Distributions of Modern Plants: Questioning Applications of n-Alkanes in Chemotaxonomy and Paleoecology. in *AGU Fall Meeting Abstracts* vol. 2010 PP21C-1704 (2010).

116. Zhang, Y. *et al.* Anthropogenically driven differences in n-alkane distributions of surface sediments from 19 lakes along the middle Yangtze River, Eastern China. *Environ. Sci. Pollut. Res.* **26**, 22472–22484 (2019).

117. Sun, Q. *et al.* Alkanes, compound-specific carbon isotope measures and climate variation during the last millennium from varved sediments of Lake Xiaolongwan, northeast China. *J. Paleolimnol.* **50**, 331–344 (2013).

118. Bush, R. T. & McInerney, F. A. Leaf wax n-alkane distributions in and across modern plants: Implications for paleoecology and chemotaxonomy. *Geochim. Cosmochim. Acta* **117**, 161–179 (2013).

119. Bush, R. T. & McInerney, F. A. Leaf wax n-alkane distributions in and across modern plants: Implications for paleoecology and chemotaxonomy. *Geochim. Cosmochim. Acta* **117**, 161–179 (2013).

120. Chikaraishi, Y. & Naraoka, H. Compound-specific δD-δ13C analyses of n-alkanes extracted from terrestrial and aquatic plants. *Phytochemistry* **63**, 361–371 (2003).

121. Bush, R. T. & Mcinerney, F. A. Organic Geochemistry Influence of temperature and C 4 abundance on n -alkane chain length distributions across the central USA. **79**, 65–73 (2015).

122. Ficken, K. J., Li, B., Swain, D. L. & Eglinton, G. An n-alkane proxy for the sedimentary input of submerged/floating freshwater aquatic macrophytes. *Org. Geochem.* **31**, 745–749 (2000).

123. Derenne, S. & Quéné, K. Analytical pyrolysis as a tool to probe soil organic matter. *J. Anal. Appl. Pyrolysis* **111**, 108–120 (2015).

124. Lee, D. H. *et al.* Evaluation of alkane indexes for quantifying organic source from end member mixing experiments based on soil and algae. *Ecol. Indic.* **107**, 105574 (2019).

125. Mead, R., Xu, Y., Chong, J. & Jaffe, R. Sediment and soil organic matter source assessment as revealed by the molecular distribution and carbon isotopic composition of n -alkanes. **36**, 363–370 (2005).

126. Wang, Y. *et al.* Predominance of even carbon-numbered n-alkanes from lacustrine sediments in Linxia Basin, NE Tibetan Plateau: Implications for climate change. *Appl. Geochemistry* **25**, 1478–1486 (2010).

127. Derrien, M., Yang, L. & Hur, J. Lipid biomarkers and spectroscopic indices for identifying organic matter sources in aquatic environments: A review. *Water Res.* **112**, 58–71 (2017).

128. Routh, J. *et al.* Multi-proxy study of soil organic matter dynamics in permafrost peat deposits reveal vulnerability to climate change in the European Russian Arctic. *Chem. Geol.* **368**, 104–117 (2014).

129. Poerschmann, J., Koschorreck, M. & Górecki, T. Organic matter in sediment layers of an acidic mining lake as assessed by lipid analysis. Part II: Neutral lipids. *Sci. Total Environ.* **578**, 219–227 (2017).

130. Eckmeier, E. & Wiesenberg, G. L. B. Short-chain n-alkanes (C16-20) in ancient soil are useful molecular markers for prehistoric biomass burning. *J. Archaeol. Sci.* **36**, 1590–1596 (2009).

131. Aichner, B., Wilkes, H., Herzschuh, U., Mischke, S. & Zhang, C. Biomarker and compound-specific δ13C evidence for changing environmental conditions and carbon limitation at Lake Koucha, eastern Tibetan Plateau. *J. Paleolimnol.* **43**, 873–899 (2010).

132. Blinkhorn, J., Parker, A. G., Ditchfield, P., Haslam, M. & Petraglia, M. Uncovering a landscape buried by the super-eruption of Toba, 74,000 years ago: A multi-proxy environmental reconstruction of landscape heterogeneity in the Jurreru Valley, south India. *Quat. Int.* **258**, 135–147 (2012).

133. Haslam, M. *et al.* The 74 ka Toba super-eruption and southern Indian hominins: Archaeology, lithic technology and environments at Jwalapuram Locality 3. *J. Archaeol. Sci.* **37**, 3370–3384 (2010).

134. Clarkson, C. *et al.* The oldest and longest enduring microlithic sequence in India: 35 000 years of modern human occupation and change at the Jwalapuram Locality 9 rockshelter. *Antiquity* **83**, 326–348 (2009).

135. Haslam, M. *et al.* A southern Indian Middle Palaeolithic occupation surface sealed by the 74 ka Toba eruption: Further evidence from Jwalapuram Locality 22. *Quat. Int.* **258**, 148–164 (2012).

136. Inglis, G. N. *et al.* Ecological and biogeochemical change in an early Paleogene peat-forming environment : Linking biomarkers and palynology. *Palaeogeogr. Palaeoclimatol. Palaeoecol.* **438**, 245–255 (2015).

137. Ajithprasad, P. Pleistocene stratigraphy and prehistoric archaeology of the orsang

valley. (1988).

138. Ajithprasad, P. Early middle palaeolithic: a transition phase between the upper acheulian and middle palaeolithic cultures in the Orsang Valley, Gujarat. *Man Environ.* **30**, 1–11 (2005).

139. Moita, P. *et al.* Mineral Carbonation of CO2 in Mafic Plutonic Rocks, II—Laboratory Experiments on Early-Phase Supercritical CO2–Brine–Rock Interactions. *Appl. Sci.* **10**, 5083 (2020).

140. Bush, R. T. *et al.* Palaeoclimates, plasticity, and the early dispersal of Homo sapiens. *J. Archaeol. Sci.* **38**, 17–37 (2011).

141. Henshilwood, C. S. *et al.* A 100,000-year-old ochre-processing workshop at Blombos Cave, South Africa. *Science (80-.).* **334**, 219–222 (2011).

142. Korisettar, R. Toward developing a basin model for Paleolithic settlement of the Indian subcontinent: geodynamics, monsoon dynamics, habitat diversity and dispersal routes. in *The evolution and history of human populations in South Asia* 69–96 (Springer, 2007).

143. Petraglia, M. *et al.* Population increase and environmental deterioration correspond with microlithic innovations in South Asia ca. 35,000 years ago. *Proc. Natl. Acad. Sci.* **106**, 12261–12266 (2009).

144. Jukar, A. M., Patnaik, R., Chauhan, P. R., Li, H.-C. & Lin, J.-P. The youngest occurrence of Hexaprotodon Falconer and Cautley, 1836 (Hippopotamidae, Mammalia) from South Asia with a discussion on its extinction. *Quat. Int.* **528**, 130–137 (2019).

145. Chauhan, P. R. Large mammal fossil occurrences and associated archaeological evidence in Pleistocene contexts of peninsular India and Sri Lanka. *Quat. Int.* **192**, 20–42 (2008).

146. Roberts, P. *et al.* Continuity of mammalian fauna over the last 200,000 y in the Indian subcontinent (Proceedings of the National Academy of Sciences of the United States of America (2014) 111 (5848-5853) DOI 10.1073/pnas.1323465111). *Proc. Natl. Acad. Sci. U. S. A.* **113**, E1963 (2014).

147. Dennell, R. *From Arabia to the Pacific: How our species colonised Asia*. (Routledge,

2020).

148. Boivin, N., Fuller, D. Q., Dennell, R., Allaby, R. & Petraglia, M. D. Human dispersal across diverse environments of Asia during the Upper Pleistocene. *Quat. Int.* **300**, 32–47 (2013).

149. Dennell, R. & Porr, M. *Southern Asia, Australia and the search for human origins*. (Cambridge University Press, 2014).

SUPPLEMENTARY DATA

Paleopedological Data
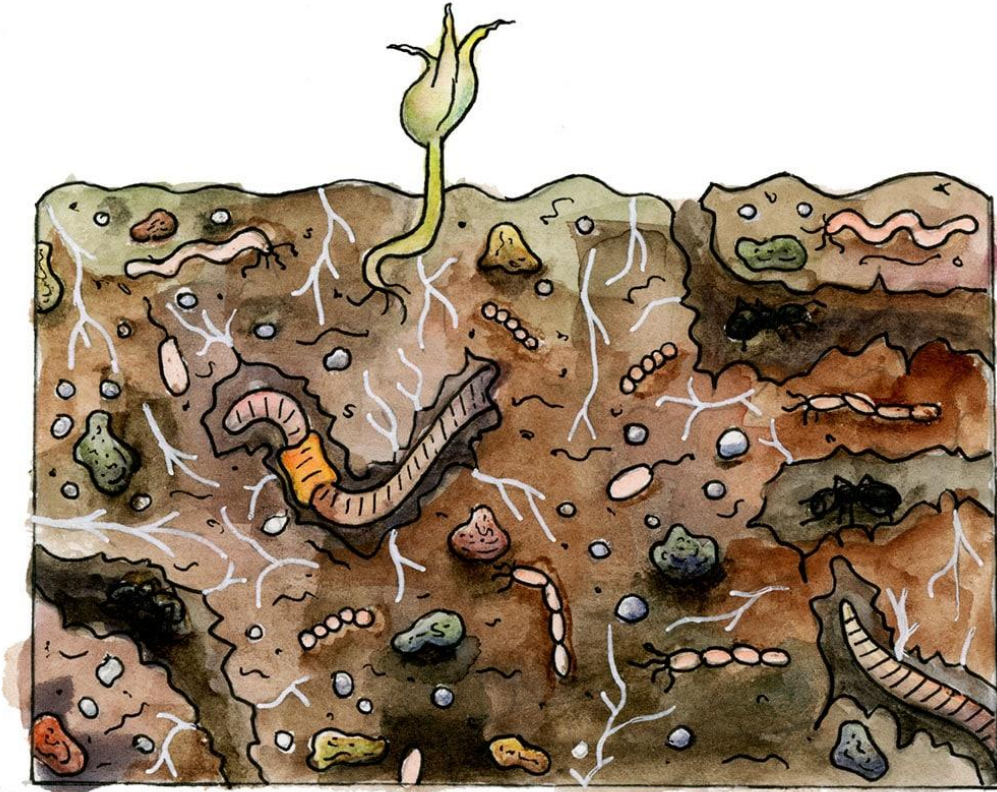
Sample Name	Sample Detail	Depth from Surface (cm)	Normalized Depth (cm)
SS0	Redeposited Toba ash	50	212
SS1	Redeposited Toba ash	80	200
MS5	Greyish Hardpan	85	195
SS2	Redeposited Toba ash	92	188
MS4	Greyish Hardpan	100	180
SS3	Redeposited Toba ash	112	168
MS3	Greyish Hardpan	123	157
SS4	Redeposited Toba ash	133	147
MS2	Greyish Hardpan	140	140
SS5	Redeposited Toba ash	155	125
MS1	Greyish Hardpan	180	100
SS6	Primary Toba ash	260	20
SS7	Pre-Toba Sediment	280	0

XRF Data   Jwalapuram

	Age	Depth	Na2O	Na2O(m)	MgO	MgO(m)	Al2O3	Al2O3(m)	SiO2	SiO2(m)	P2O5	P2O5(m)	K2O	K2O(m)	CaO	CaO(m)	TiO2	TiO2 (m)	Fe2O3	Fe2O3(m)
JWP_SS7		0	0.93	0.015	7.630	0.189	14.540	0.143	53.480	0.890	0.030	0.000158	2.100	0.022	9.640	0.172	0.660	0.008	7.640	0.048
JWP_SS6	74ka	20	3.78	0.061	0.360	0.009	13.350	0.131	74.820	1.245	0.017	0.000090	3.631	0.039	1.080	0.019	0.108	0.001	1.556	0.010
JWP_MS1		100	3.433	0.055	1.714	0.043	13.700	0.134	71.990	1.198	0.015	0.000079	3.711	0.039	1.690	0.030	0.179	0.002	2.481	0.016
JWP_SS5		125	3.407	0.055	1.160	0.029	13.040	0.128	74.970	1.248	0.012	0.000063	3.981	0.042	1.353	0.024	0.101	0.001	1.454	0.009
JWP_MS2		140	2.966	0.048	3.970	0.098	12.280	0.120	69.630	1.159	0.019	0.000100	3.642	0.039	4.046	0.072	0.140	0.002	1.899	0.012
JWP_SS4		147	3.531	0.057	0.608	0.015	13.060	0.128	75.290	1.253	0.014	0.000074	4.150	0.044	1.007	0.018	0.098	0.001	1.382	0.009
JWP_MS3		157	2.564	0.041	4.843	0.120	12.750	0.125	68.980	1.148	0.017	0.000090	3.451	0.037	4.009	0.071	0.233	0.003	2.774	0.017
JWP_SS3		168	3.128	0.050	4.062	0.101	12.010	0.118	69.110	1.150	0.017	0.000090	3.859	0.041	5.502	0.098	0.109	0.001	1.339	0.008
JWP_MS4		180	2.695	0.043	9.351	0.232	13.640	0.134	72.320	1.204	0.037	0.000195	3.365	0.036	9.655	0.172	0.225	0.003	2.950	0.018
JWP_SS2		188	3.229	0.052	3.439	0.085	12.280	0.120	69.130	1.150	0.020	0.000105	3.920	0.042	5.271	0.094	0.099	0.001	1.300	0.008
JWP_MS5		195	2.735	0.044	10.520	0.261	9.195	0.090	56.960	0.948	0.028	0.000147	2.203	0.023	12.370	0.221	0.087	0.001	1.086	0.007
JWP_SS1		200	3.505	0.057	0.368	0.009	13.420	0.132	75.660	1.259	0.018	0.000095	4.182	0.044	0.995	0.018	0.113	0.001	1.438	0.009
JWP_SS0		212	4.04	0.065	0.446	0.011	13.590	0.133	74.830	1.245	0.020	0.000105	4.095	0.043	1.025	0.018	0.128	0.002	1.627	0.010

	Na	Mg	Al	Si	P	Cl	K	Ca	Ti	V	Cr	Mn	Fe	Sr	Y	Zr	Nb	Ba
JWP_SS7	0.69	4.6	7.7	25	0.01	0.01	1.75	6.89	0.4	0.01	0.01	0.2	5.22	0.031	0.002	0.014	0.002	0.085
JWP_SS6	2.806	0.217	7.064	34.97	0.008	0.005	3.014	0.772	0.065	8.05	0.005	0.065	1.088	0.009	0.003	0.016	0.003	0.061
JWP_MS1	2.547	1.034	7.252	33.65	0.007	0.005	3.08	1.208	0.107	0.005	0.001	0.083	1.735	0.014	0.003	0.013	0.002	0.036
JWP_SS5	2.528	0.699	6.901	35.05	0.005	0.005	3.305	0.967	0.061	0.003	0.003	0.068	1.017	0.011	0.003	0.014	0.002	0.062
JWP_MS2	2.2	2.394	6.502	32.55	0.008	0.006	3.023	2.891	0.084	0.004	0.004	0.068	1.328	0.025	0.003	0.011	0.002	0.059
JWP_SS4	2.619	0.367	6.913	35.19	0.006	0.005	3.446	0.72	0.058	0.003	0.003	0.067	0.967	0.009	0.004	0.014	0.002	0.056
JWP_MS3	1.902	2.92	6.75	32.24	0.008	0.006	2.865	2.865	0.139	0.003	0.01	0.08	1.9	0.026	0.003	0.013	0.003	0.067
JWP_SS3	2.32	2.45	6.355	32.3	0.007	0.007	3.203	3.933	0.065	0.005	0.002	0.071	0.936	0.033	0.003	0.011	0.003	0.061
JWP_MS4	1.999	5.639	7.219	33.81	0.016	0.006	2.793	6.9	0.135	0.003	0.002	0.095	2.063	0.053	0.003	0.011	0.003	0.059
JWP_SS2	2.395	2.074	6.5	32.32	0.009	0.006	3.254	3.767	0.059	0.005	0.002	0.059	0.909	0.031	0.003	0.011	0.002	0.055
JWP_MS5	2.029	6.345	4.867	26.63	0.012	0.007	1.829	8.84	0.052	0.005	0.014	0.058	0.759	0.085	0.003	0.004	0.003	0.048
JWP_SS1	2.6	0.222	7.103	35.36	0.008	0.005	3.472	0.711	0.068	0.002	0.002	0.069	1.006	0.009	0.004	0.015	0.003	0.057
JWP_SS0	2.997	0.269	7.193	34.98	0.009	0.005	3.399	0.733	0.077		0.002	0.065	1.138	0.009	0.004	0.015	0.002	0.062

XRF Data

Jwalapuram

	LOI	CIA	CIW (CIA-K)	PIA	STI	R	V	WIP	Sa	Saf	A-CN-K	BA	Base/Ti	MIA(o)	MIA(R)	IOL
JWP_SS7	18.55	40.54	43.28	39.16	17.28	6.24	0.44	29.85	6.24	6.29	0.88	2.79	48.23	32.34	34.20	17.63
JWP_SS6	5.24	52.43	62.00	53.52	51.81	9.51	1.90	35.87	9.51	9.52	3.85	0.98	94.49	52.41	52.55	10.15
JWP_MS1	7.48	51.82	61.11	52.62	40.91	8.92	1.36	36.42	8.92	8.93	3.50	1.25	74.74	47.24	46.79	11.12
JWP_SS5	7.01	51.31	61.79	51.98	52.85	9.76	1.58	34.64	9.76	9.76	3.47	1.17	118.76	47.71	48.63	9.89
JWP_MS2	13.02	43.15	50.09	40.53	44.12	9.62	0.73	38.39	9.62	9.63	2.98	2.13	146.75	33.98	37.96	10.25
JWP_SS4	5.23	51.84	63.09	52.86	53.55	9.78	1.91	34.26	9.78	9.79	3.60	1.05	109.30	50.50	50.66	9.84
JWP_MS3	10.75	45.55	52.56	43.93	33.65	9.18	0.69	37.09	9.18	9.20	2.58	2.16	92.45	34.57	36.72	11.04
JWP_SS3	11.36	38.33	44.22	34.08	49.31	9.76	0.64	40.17	9.76	9.77	3.11	2.46	212.79	30.30	37.00	9.89
JWP_MS4	15.65	34.73	38.29	31.26	35.80	9.00	0.38	50.86	9.00	9.01	2.62	3.61	171.62	23.96	28.87	11.23
JWP_SS2	10.81	39.09	45.19	35.05	51.90	9.55	0.70	39.38	9.55	9.56	3.21	2.27	220.33	32.02	39.16	10.05
JWP_MS5	19.88	23.84	25.41	20.15	48.55	10.51	0.22	54.52	10.51	10.52	2.58	6.09	504.20	15.01	21.20	9.28
JWP_SS1	4.77	52.58	63.92	54.00	50.94	9.57	2.11	33.35	9.57	9.58	3.57	0.97	90.38	52.39	52.50	10.05
JWP_SS0	4.97	51.22	61.49	51.83	48.37	9.34	1.87	38.50	9.34	9.35	4.11	1.04	86.14	50.97	50.64	10.33

	Al/Si	Ba/Sr	K/(Fe+Mg)	Ti/Al	Fe+Mg	∑Bases/Al	Base/Ti	(K+Na)/Al	Fe:Mn	Ca/Sr
JWP_SS7	0.308	1.749407	5.611429	0.051948	9.82	1.80909091	34.825	0.316883117	26.1	485.8948
JWP_SS6	0.202002	4.324351	0.432979	0.009202	1.305	0.96390147	104.7538	0.82389581	16.73846	187.5252
JWP_MS1	0.215513	1.64062	0.899026	0.014755	2.769	1.08507998	73.54206	0.775923883	20.90361	188.6356
JWP_SS5	0.19689	3.596107	0.519213	0.008839	1.716	1.08665411	122.9344	0.84523982	14.95588	192.1846
JWP_MS2	0.199754	1.505725	1.231227	0.012919	3.722	1.61611812	125.0952	0.803291295	19.52941	252.8092
JWP_SS4	0.196448	3.969896	0.387115	0.00839	1.334	1.03457254	123.3103	0.877332562	14.43284	174.8939
JWP_MS3	0.209367	1.644126	1.682373	0.020593	4.82	1.56325926	75.91367	0.706222222	23.75	240.8996
JWP_SS3	0.196749	1.179368	1.057134	0.010228	3.386	1.87348544	183.1692	0.869079465	13.1831	260.5522
JWP_MS4	0.213517	0.710247	2.757608	0.018701	7.702	2.40074803	128.3778	0.663803851	21.71579	284.6151
JWP_SS2	0.201114	1.131969	0.916718	0.009077	2.983	1.76769231	194.7458	0.869076923	15.40678	265.6554
JWP_MS5	0.182764	0.360293	3.88409	0.010684	7.104	3.91267721	366.2115	0.792685433	13.08621	227.3621
JWP_SS1	0.200877	4.040787	0.353687	0.009573	1.228	0.98620301	103.0147	0.854850063	14.57971	172.7078
JWP_SS0	0.205632	4.395242	0.413945	0.010705	1.407	1.02849993	96.07792	0.889197831	17.50769	178.0517

Immobile elements
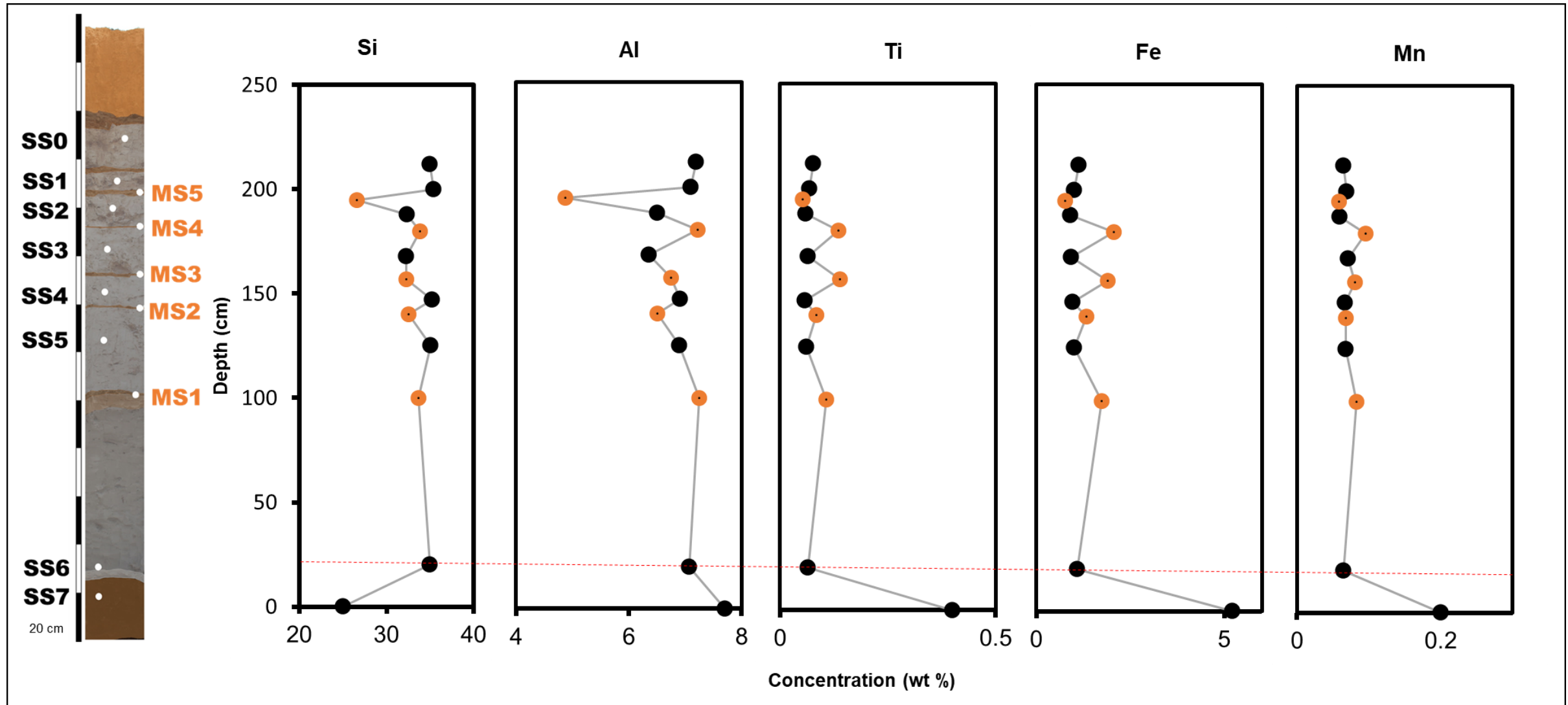
Mobile elements
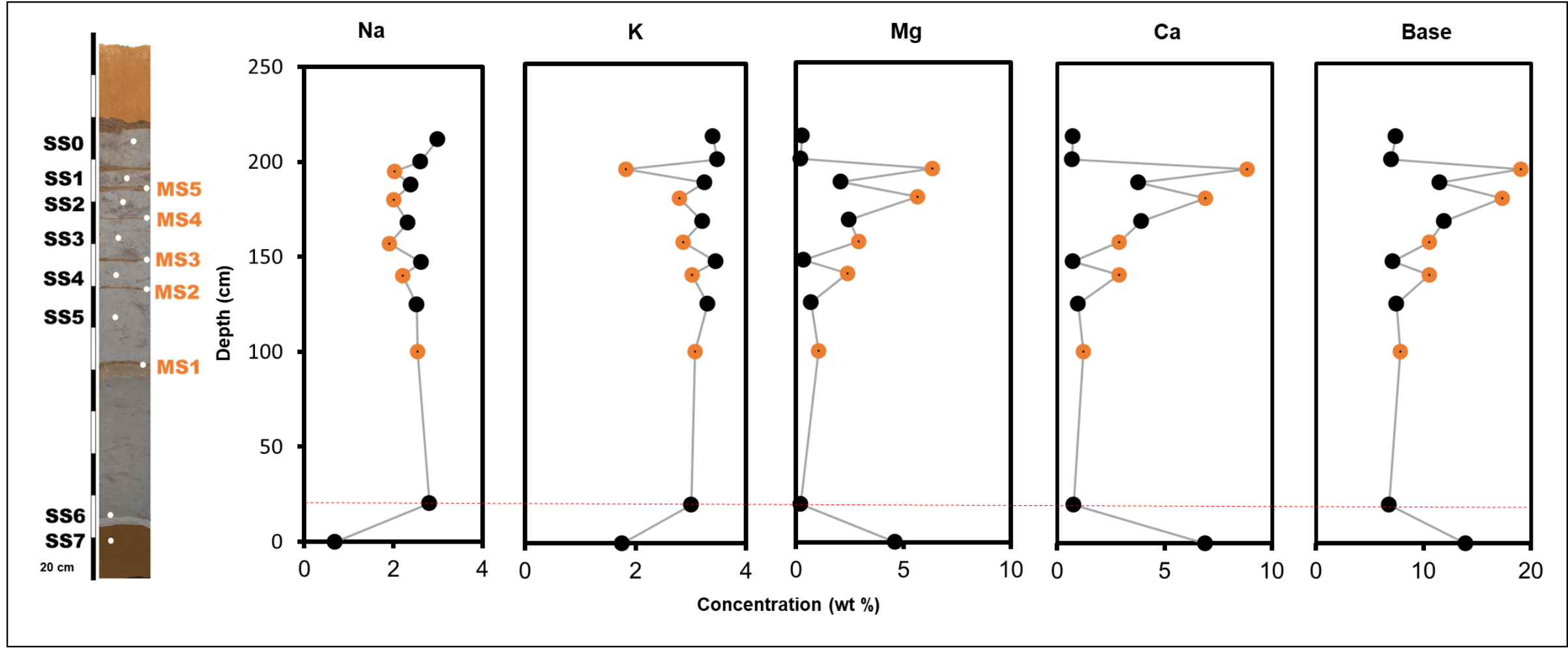
Pedogenic Ratios
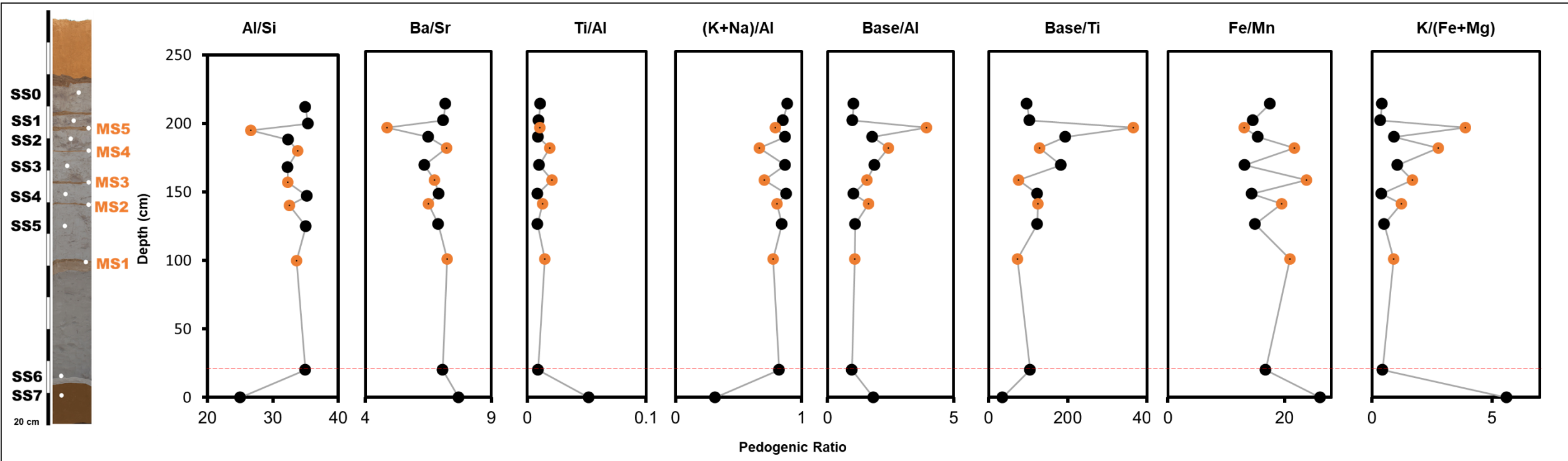
Weathering Indices
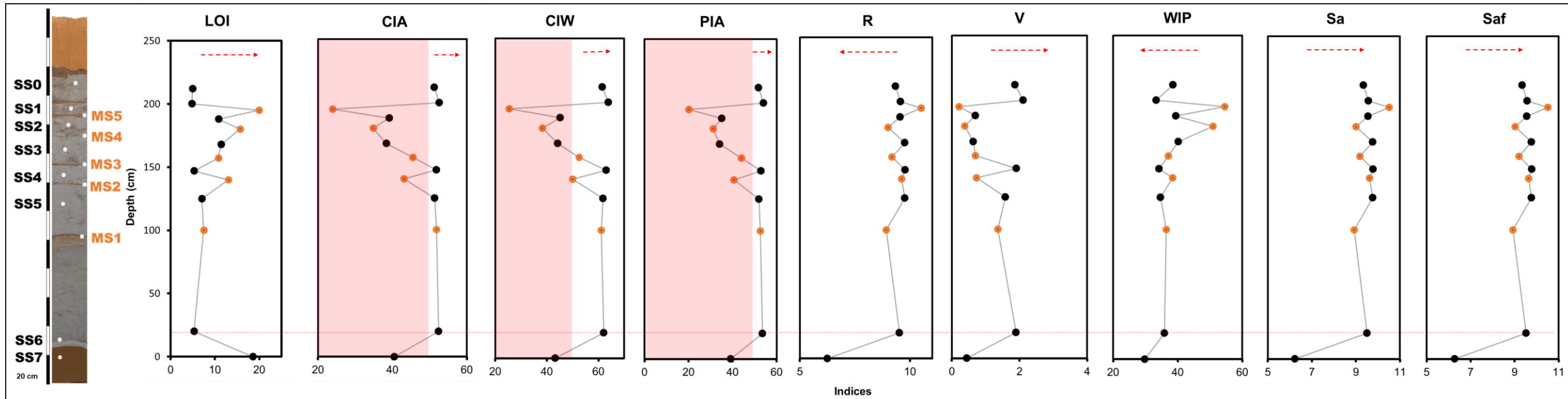
XRD Data

Jwalapuram

Sam ID	Depth (cm)	Crystallinity %			Compounds (S-Q%)					
		Amorphous	Crystalline		Quartz	Plagioclase	Sanidine	Biotite	Dolomite	Clay
JWP_SS0	212	87.1	12.9		6.3	35.2	19.2	39	0.3	0
JWP_SS1	200	89.8	10.2		11.1	22.1	19.6	43.6	1.5	2.1
JWP_MS5	195	70.4	29.6		7.1	21.9	20.8	5	45.2	0
JWP_SS2	188	77.9	22.1		9.3	40.2	22.2	16.6	11.7	0
JWP_MS4	180	60.8	39.2		22.6	21	16.3	8.8	31.3	0
JWP_SS3	168	87	13		12.5	37.2	26	10.1	14.2	0
JWP_MS3	157	76.8	23.2		36.3	20.1	18.4	5.2	20	0
JWP_SS4	147	96.4	3.6		9.6	45.2	24.5	16	4.7	0
JWP_MS2	140	91.1	8.9		19.8	44.2	13.9	10.4	11.7	0
JWP_SS5	125	92.2	7.8		16.7	31.6	21.1	27.5	3.1	0
JWP_MS1	100	86	14		27.2	27.7	18.5	23.2	3.5	0
JWP_SS6	20	91.6	8.4		10.7	47.9	21.3	13.8	0.8	5.5
JWP_SS7	0	30.7	69.3		53.9	10	5.9	0	8	12.1
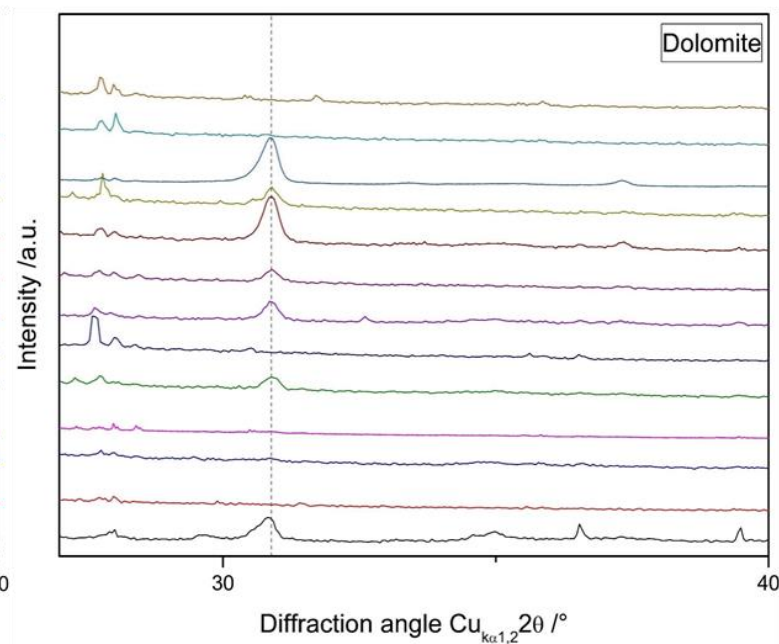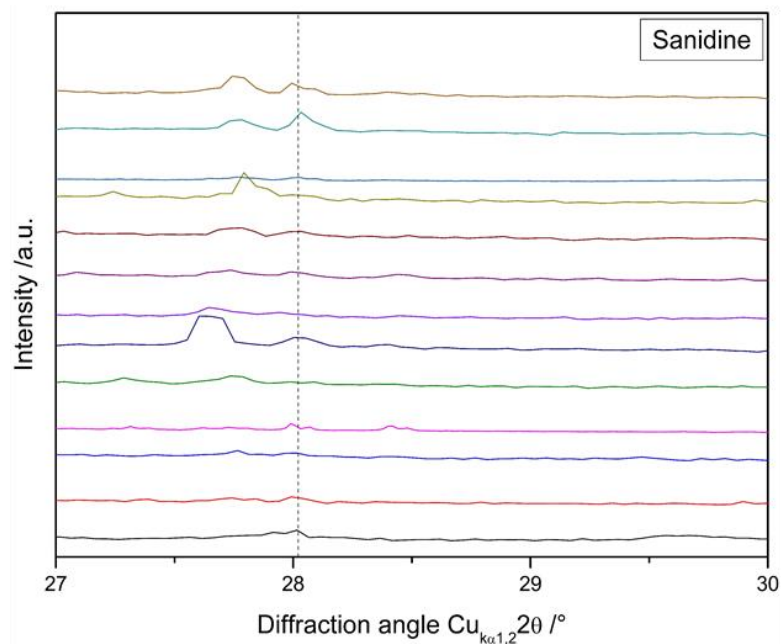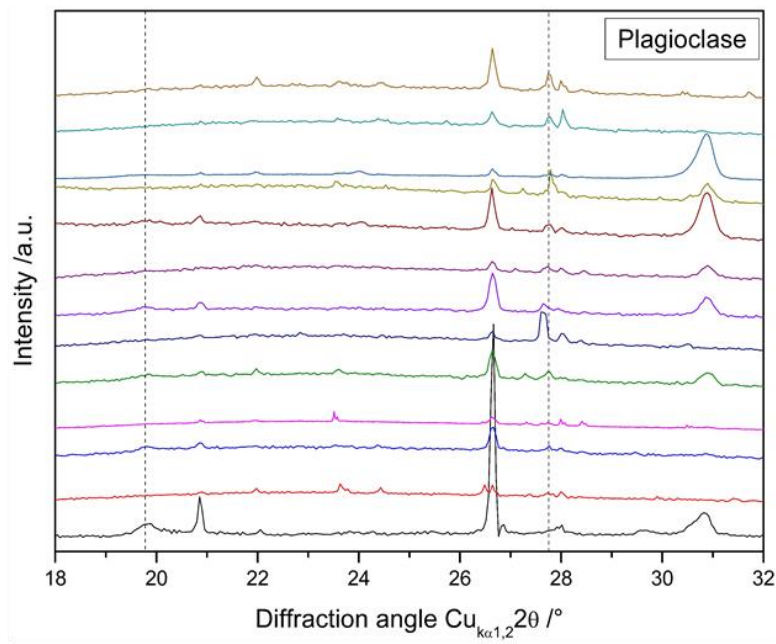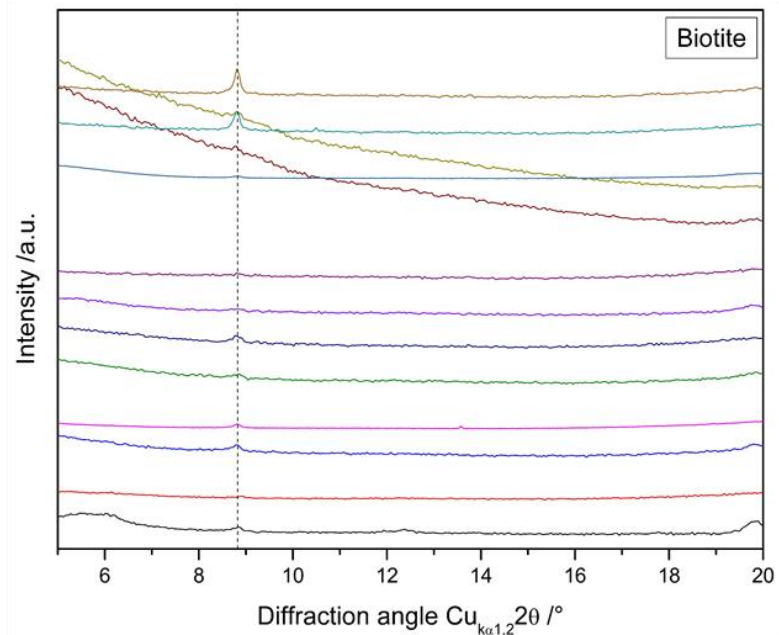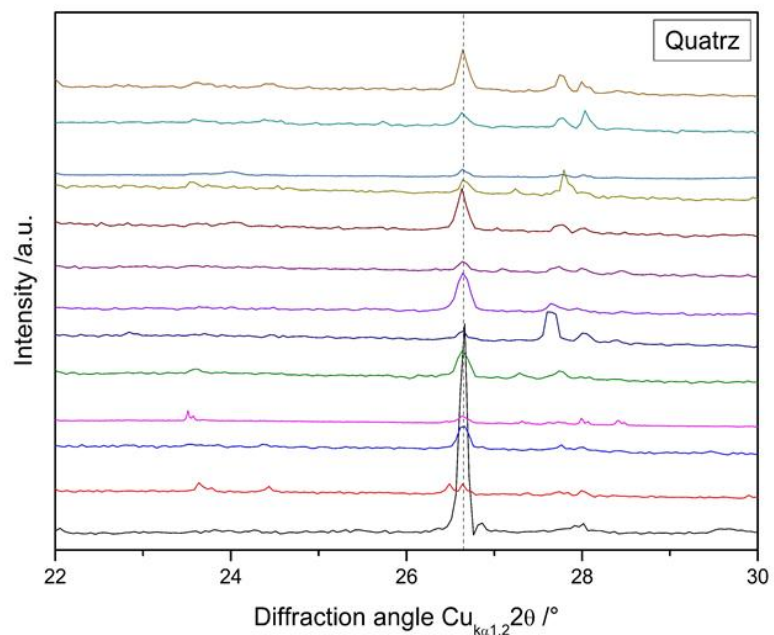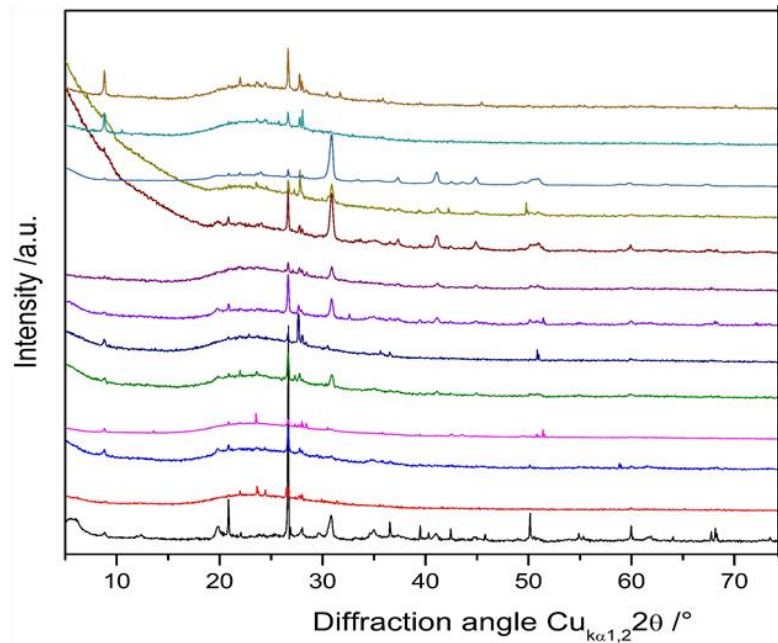
JWP-SS7 —— JWP-SS6 —— JWP-MS1 —— JWP-SS5 —— JWP-MS2 —— JWP-SS4 —— JWP-MS3 —— JWP-SS3 —— JWP-MS4 —— JWP-SS2 —— JWP-MS5 —— JWP-SS1 —— JWP-SS0

Computed Crystallinity

Sample Name	Sample Detail	Depth from YTT layer (cm)	Normalized Depth (cm)
S16	Post-YTT	35	75
S15	Post-YTT	30	70
S14	Post-YTT	25	65
S13	Post-YTT	20	60
S12	Post-YTT	15	55
S11	Post-YTT	10	50
S10	Post-YTT	5	45
S9, T1, EA1, EA2, EA3	YTT	0	40
S8	Pre-YTT	-5	35
S7	Pre-YTT	-10	30
S6	Pre-YTT	-15	25
S5	Pre-YTT	-20	20
S4	Pre-YTT	-25	15
S3	Pre-YTT	-30	10
S2	Pre-YTT	-35	5
S1	Pre-YTT	-40	0

XRF Data

Tejpor

S.No.	Age	Depth	Na2O	Na2O(m)	MgO	MgO(m)	Al2O3	Al2O3(m)	SiO2	SiO2(m)	P2O5	P2O5(m)	K2O	K2O(m)	CaO	CaO(m)	Fe2O3	Fe2O3(m)	TiO2	TiO2(m)
TJP_S16		75	2.106	0.0340	6.177	0.153	19.86	0.195	70.5	1.173	0.287	0.0015	1.643	0.017	7.428	0.132	20.73	0.13	4.536	0.057
TJP_S15		70	1.837	0.0296	4.562	0.113	12.79	0.125	46.62	0.776	0.147	0.0008	1.21	0.013	6.232	0.111	16.21	0.102	3.266	0.041
TJP_S14		65	1.784	0.0288	4.651	0.115	12.97	0.127	46.3	0.771	0.143	0.0008	1.337	0.014	6.508	0.116	17.61	0.11	3.25	0.041
TJP_S13		60	1.805	0.0291	4.947	0.123	13.92	0.137	50.92	0.847	0.188	0.001	1.255	0.013	6.61	0.118	17.04	0.107	3.722	0.047
TJP_S12		55	1.761	0.0284	4.405	0.109	14.16	0.139	51.71	0.861	0.172	0.0009	1.22	0.013	6.947	0.124	14.33	0.09	3.021	0.038
TJP_S11	60±6	50	1.683	0.0272	4.661	0.116	16.44	0.161	57.6	0.959	0.221	0.0012	1.47	0.016	6.112	0.109	14.92	0.093	2.911	0.036
TJP_S10		45	1.947	0.0314	4.448	0.110	13.95	0.137	52.06	0.866	0.225	0.0012	1.425	0.015	5.963	0.106	14.73	0.092	3.33	0.042
TJP_EA1	71±9	40	3.01	0.0486	1.068	0.026	14.33	0.141	70.63	1.175	0.057	0.0003	3.833	0.041	1.655	0.03	3.823	0.024	0.611	0.008
TJP_S9	71±9	40	2.611	0.0421	1.887	0.047	14.24	0.14	67.11	1.117	0.106	0.0006	3.346	0.036	2.754	0.049	6.123	0.038	1.12	0.014
TJP_S8		35	1.994	0.0322	4.486	0.111	14.87	0.146	55.67	0.926	0.246	0.0013	1.515	0.016	5.984	0.107	15.86	0.099	3.516	0.044
TJP_S7		30	1.84	0.0297	4.397	0.109	14.35	0.141	53.41	0.889	0.227	0.0012	1.471	0.016	5.421	0.097	14.83	0.093	3.246	0.041
TJP_S6		25	2.128	0.0343	4.105	0.102	13.41	0.132	51.65	0.86	0.223	0.0012	1.472	0.016	5.689	0.101	15.06	0.094	3.316	0.042
TJP_S5		20	1.914	0.0309	4.216	0.105	13.95	0.137	53.67	0.893	0.231	0.0012	1.487	0.016	5.726	0.102	15.36	0.096	3.436	0.043
TJP_S4		15	2.242	0.0362	5.413	0.134	15.57	0.153	57.67	0.96	0.265	0.0014	1.292	0.014	9.168	0.163	17.22	0.108	3.676	0.046
TJP_S3	74±7	10	2.453	0.0396	5.656	0.140	15.31	0.15	57.02	0.949	0.285	0.0015	1.681	0.018	9.135	0.163	18.88	0.118	3.823	0.048
TJP_S2		5	2.012	0.0325	5.012	0.124	14.44	0.142	56.28	0.937	0.28	0.0015	1.608	0.017	7.618	0.136	18.5	0.116	4.067	0.051
TJP_S1		0	1.971	0.0318	4.803	0.119	12.61	0.124	45.8	0.762	0.143	0.0008	1.336	0.014	6.473	0.115	17.41	0.109	3.411	0.043

XRF Data

Tejpor

S.No.	Na	Mg	Al	Si	P	Cl	K	Ca	Ti	V	Cr	Mn	Fe	Co	Ni	Cu	Zn	Ga	As	Rb	Sr	Y	Zr	Nb	Ba	Th	U
TJP_S16	1.563	3.725	10.61	32.95	0.125	0.005	1.364	5.309	2.719	0.062	0.013	0.245	14.5	0.023	0.007	0.012	0.015	0.002	4.07	0.005	0.027	0.002	0.028	0.004	0.069	0.01	0
TJP_S15	1.363	2.751	6.77	21.79	0.064	0.005	1.005	4.454	1.958	0.041	0.015	0.204	11.34	0.019	0.008	0.001	0.013	0.002	1.74	0.004	0.024	0.002	0.022	0.004	0.073	6.42	0.47
TJP_S14	1.323	2.805	6.863	21.64	0.062	0.005	1.11	4.651	1.948	0.047	0.012	0.213	12.32	0.026	0.007	0.014	0.013	0.003	3.61	0.005	0.025	0.002	0.024	0.003	0.084	6.42	0.12
TJP_S13	1.339	2.983	7.212	23.8	0.082	0.005	1.042	4.724	2.231	0.046	0.012	0.349	11.92	0.009	0.007	0.012	0.014	0.002	2.31	0.004	0.026	0.002	0.022	0.005	0.093	0.001	0.54
TJP_S12	1.306	2.656	7.492	24.17	0.075	0.005	1.013	4.965	1.811	0.04	0.012	0.299	10.03	0.007	0.007	0.012	0.012	0.002	4.08	0.004	0.023	0.002	0.021	0.004	0.079	6.17	0.56
TJP_S11	1.248	2.811	8.7	26.93	0.096	0.005	1.222	4.368	1.745	0.043	0.01	0.305	10.44	0.007	0.006	0.011	0.011	0.002	3.87	0.005	0.024	0.002	0.022	0.004	0.083	9.62	0.31
TJP_S10	1.444	2.682	7.385	24.33	0.098	0.005	1.183	4.262	1.996	0.04	0.012	0.31	10.3	0.007	0.006	0.011	0.013	0.002	2.52	0.005	0.025	0.002	0.021	0.004	0.046	0.001	0.89
TJP_EA1	2.233	0.644	7.582	33.01	0.025	0.005	3.182	1.183	0.366	0.009	0.004	0.115	2.674	0.001	0.002	0.005	0.005	0.002	9.23	0.019	0.012	0.003	0.017	0.003	0.065	0.002	0.73
TJP_S9	1.937	1.138	7.535	31.37	0.046	0.005	2.778	1.968	0.671	0.013	0.0007	0.154	4.283	0.001	0.003	0.005	0.006	0.002	7.08	0.016	0.017	0.003	0.018	0.003	0.077	0.002	1.14
TJP_S8	1.479	2.705	7.871	26.02	0.107	0.005	1.258	4.277	2.108	0.043	0.023	0.32	11.1	0.009	0.009	0.01	0.012	0.002	2.83	0.005	0.026	0.002	0.022	0.004	0.081	3.66	0.57
TJP_S7	1.365	2.652	7.596	24.97	0.099	0.005	1.221	3.874	1.946	0.036	0.01	0.306	10.37	0.008	0.005	0.011	0.012	0.002	4.05	0.005	0.025	0.002	0.021	0.004	0.074	10	0.27
TJP_S6	1.578	2.476	7.098	24.24	0.097	0.006	1.222	4.066	1.988	0.051	0.012	0.191	10.53	0.013	0.006	0.011	0.012	0.002	3.7	0.005	0.027	0.002	0.021	0.005	0.031	10	0.53
TJP_S5	1.42	2.542	7.385	25.09	0.101	0.005	1.235	4.092	2.06	0.047	0.01	0.191	10.74	0.013	0.006	0.011	0.013	0.002	2.44	0.005	0.026	0.003	0.021	0.005	0.076	10	0.52
TJP_S4	1.664	3.264	8.242	26.96	0.116	0.005	1.073	6.552	2.203	0.051	0.009	0.211	12.05	0.017	0.006	0.01	0.014	0.002	3.01	0.004	0.029	0.002	0.022	0.004	0.099	7.03	0.3
TJP_S3	1.819	3.411	8.102	26.65	0.124	0.005	1.396	6.529	2.291	0.061	0.011	0.234	13.2	0.024	0.006	0.011	0.015	0.02	3.23	0.004	0.029	0.002	0.024	0.004	0.093	5.66	0.21
TJP_S2	1.493	3.022	7.645	26.31	0.122	0.005	1.335	5.444	2.438	0.06	0.01	0.221	12.94	0.017	0.006	0.011	0.014	0.002	3.39	0.004	0.028	0.002	0.024	0.004	0.085	10	0.4
TJP_S1	1.46	2.9	6.68	21.41	0.07	0.01	1.11	4.63	2.05	0.049	0.013	0.215	12.18	0.019	0.008	0.013	0.013	0.002	3.43	0.004	0.024	0.002	0.023	0.004	0.08	8.04	0.22

XRF Data

Tejpor

S.No.	LOI	CIA	CIW	Sa	Saf	A-CN-K	BA	Base/Ti	MIA(o)	MIA(R)	IOL	PIA	R	V	WIP
TJP_S16	9.16	51.44	2.00	6.02	6.15	0.079	1.73	5.94	49.06	29.44	21.67	51.59	6.02	0.66	69.31
TJP_S15	9.37	44.95	1.53	6.18	6.29	0.031	2.13	6.53	45.97	25.41	22.63	44.44	6.18	0.54	55.66
TJP_S14	10.42	44.44	1.51	6.06	6.17	0.026	2.16	6.75	46.40	24.85	23.56	43.83	6.06	0.54	57.20
TJP_S13	8.94	45.99	1.60	6.21	6.31	0.034	2.07	6.08	46.22	25.94	22.30	45.60	6.21	0.56	57.77
TJP_S12	10.35	45.67	1.57	6.20	6.29	0.030	1.98	7.26	45.44	27.60	20.99	45.26	6.20	0.58	56.43
TJP_S11	9.37	51.52	2.03	5.94	6.04	0.064	1.66	7.34	48.79	30.89	20.99	51.68	5.94	0.70	56.41
TJP_S10	7.42	47.23	1.70	6.33	6.42	0.047	1.92	6.31	46.53	27.79	20.91	46.91	6.33	0.61	57.50
TJP_EA1	5.26	54.20	2.92	8.36	8.39	0.119	1.03	18.99	53.10	45.38	12.28	56.12	8.36	1.73	67.46
TJP_S9	5.60	52.42	2.54	8.00	8.03	0.097	1.24	12.38	50.63	39.73	13.75	53.30	8.00	1.27	64.70
TJP_S8	7.41	48.48	1.80	6.35	6.45	0.055	1.83	6.05	47.94	28.52	20.93	48.30	6.35	0.65	58.86
TJP_S7	7.52	49.78	1.90	6.32	6.41	0.058	1.78	6.18	48.20	29.04	20.81	49.76	6.32	0.66	55.38
TJP_S6	7.91	46.49	1.65	6.54	6.63	0.049	1.93	6.10	47.14	27.46	20.81	46.05	6.54	0.62	57.92
TJP_S5	7.96	47.91	1.76	6.53	6.62	0.050	1.85	5.89	47.91	28.13	20.69	47.65	6.53	0.64	56.48
TJP_S4	6.52	41.71	1.32	6.28	6.39	0.012	2.28	7.56	42.84	25.11	21.35	41.04	6.28	0.50	69.91
TJP_S3	7.22	40.53	1.28	6.32	6.44	0.009	2.40	7.54	42.67	23.87	22.05	39.52	6.32	0.49	75.75
TJP_S2	7.84	43.31	1.45	6.61	6.73	0.021	2.19	6.08	45.40	24.97	21.56	42.53	6.61	0.54	65.42
TJP_S1	10.88	43.38	1.44	6.16	6.27	0.026	2.27	6.57	45.34	24.10	23.39	42.65	6.16	0.52	59.24

XRF Data   Tejpor

| S.No.	Al/Si	Ba/Sr	K/(Fe+Mg)	Ti/Al	∑Bases/Al	Base/Ti	(K+Na)/Al	Fe:Mn
TJP_S16	0.32	1.630	0.075	0.26	1.127332705	4.399043766	0.275871819	59.18367
TJP_S15	0.31	1.941	0.071	0.29	1.414032496	4.889172625	0.349778434	55.58824
TJP_S14	0.32	2.144	0.073	0.28	1.440915052	5.076488706	0.35450969	57.84038
TJP_S13	0.30	2.282	0.070	0.31	1.398779811	4.52173913	0.330144204	34.15473
TJP_S12	0.31	2.191	0.080	0.24	1.326748532	5.488680287	0.309530166	33.54515
TJP_S11	0.32	2.206	0.092	0.20	1.10908046	5.529512894	0.283908046	34.22951
TJP_S10	0.30	1.174	0.091	0.27	1.296005416	4.79509018	0.355721056	33.22581
TJP_EA1	0.23	3.456	0.959	0.05	0.955156951	19.78688525	0.714191506	23.25217
TJP_S9	0.24	2.890	0.512	0.09	1.037956204	11.6557377	0.625746516	27.81169
TJP_S8	0.30	1.988	0.091	0.27	1.234785923	4.610531309	0.347732181	34.6875
TJP_S7	0.30	1.889	0.094	0.26	1.199578726	4.682425488	0.340442338	33.88889
TJP_S6	0.29	0.733	0.094	0.28	1.316145393	4.699195171	0.394477318	55.13089
TJP_S5	0.29	1.865	0.093	0.28	1.257819905	4.509223301	0.359512525	56.23037
TJP_S4	0.31	2.178	0.070	0.27	1.523052657	5.698138901	0.332079592	57.109
TJP_S3	0.30	2.046	0.084	0.28	1.623673167	5.742034046	0.396815601	56.41026
TJP_S2	0.29	1.937	0.084	0.32	1.477305428	4.632485644	0.369914977	58.55204
TJP_S1	0.31	2.127	0.074	0.31	1.511976048	4.926829268	0.384730539	56.65116

Immobile elements
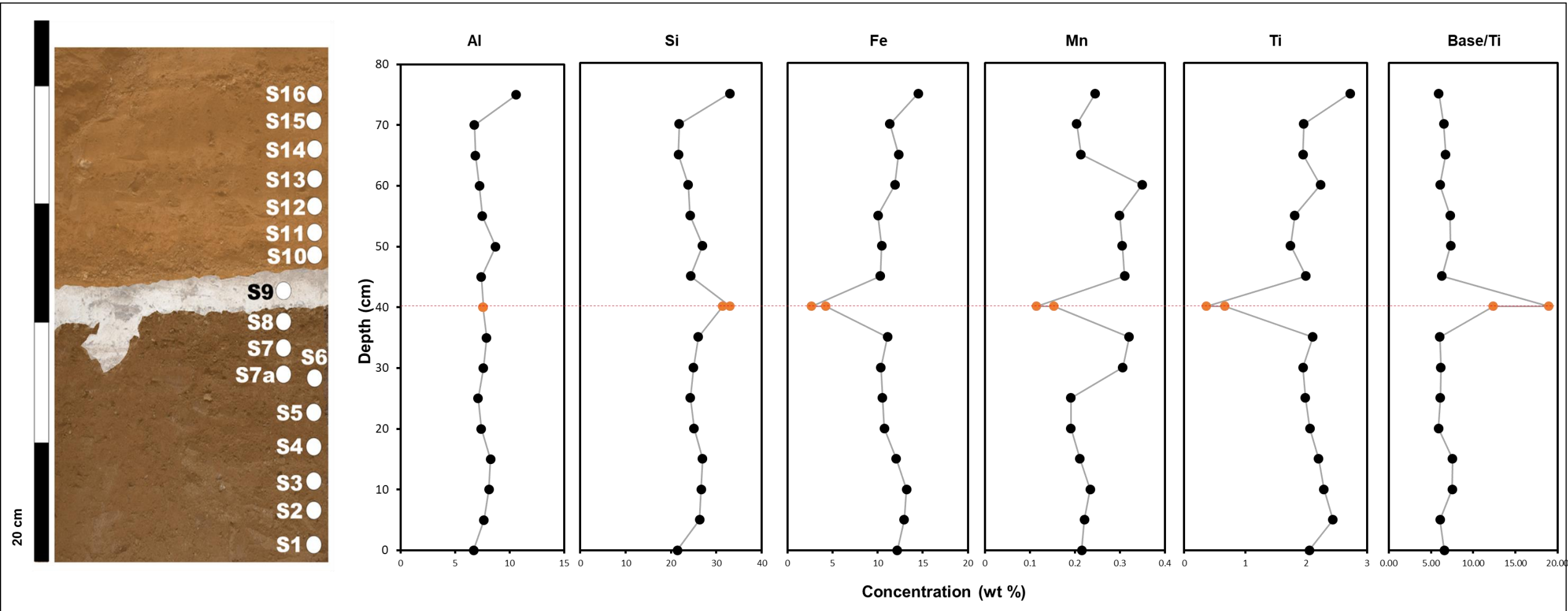
# Mobile elements
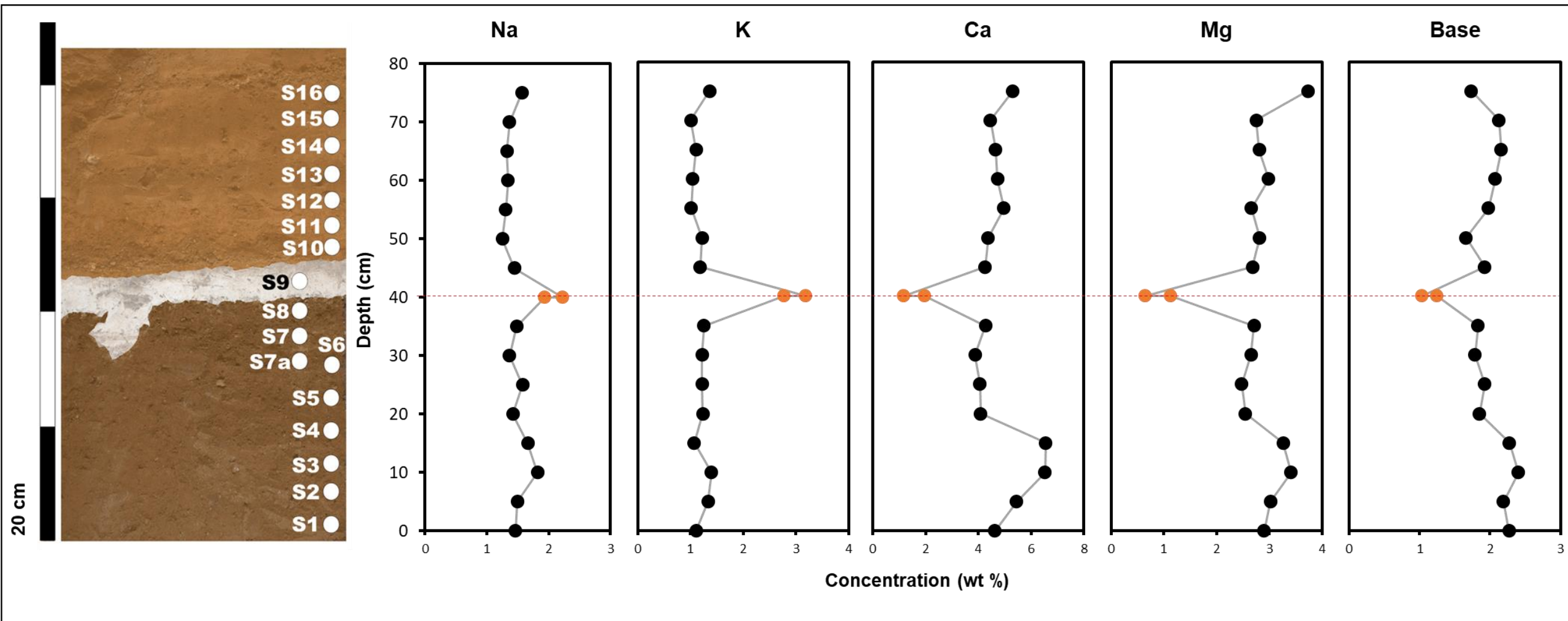
Pedogenic Ratios
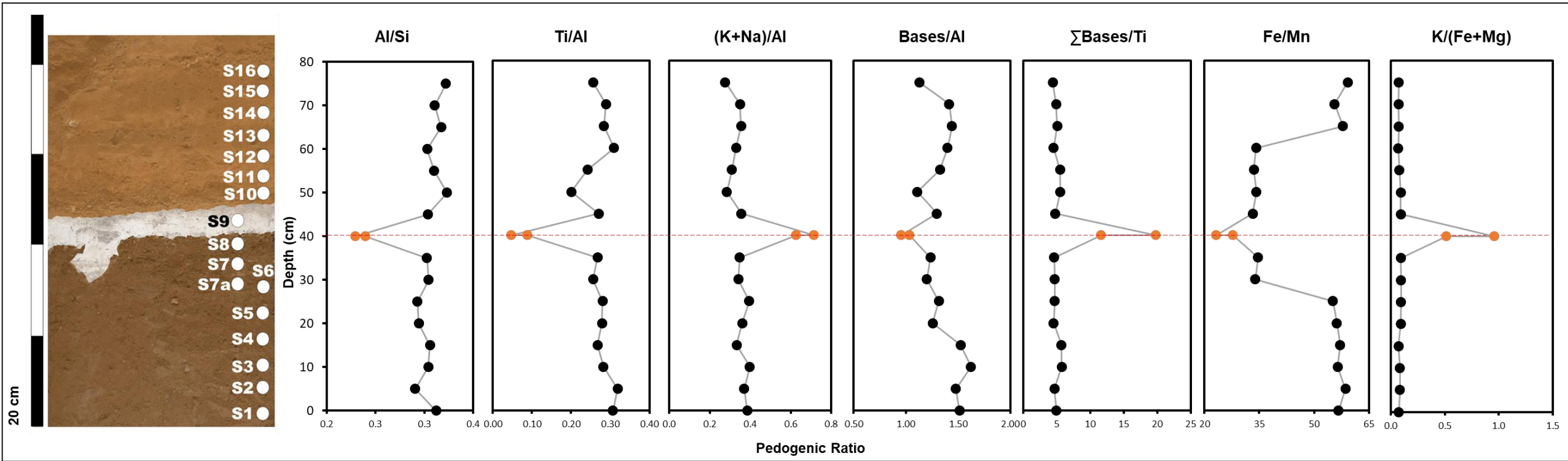
Weathering Indices
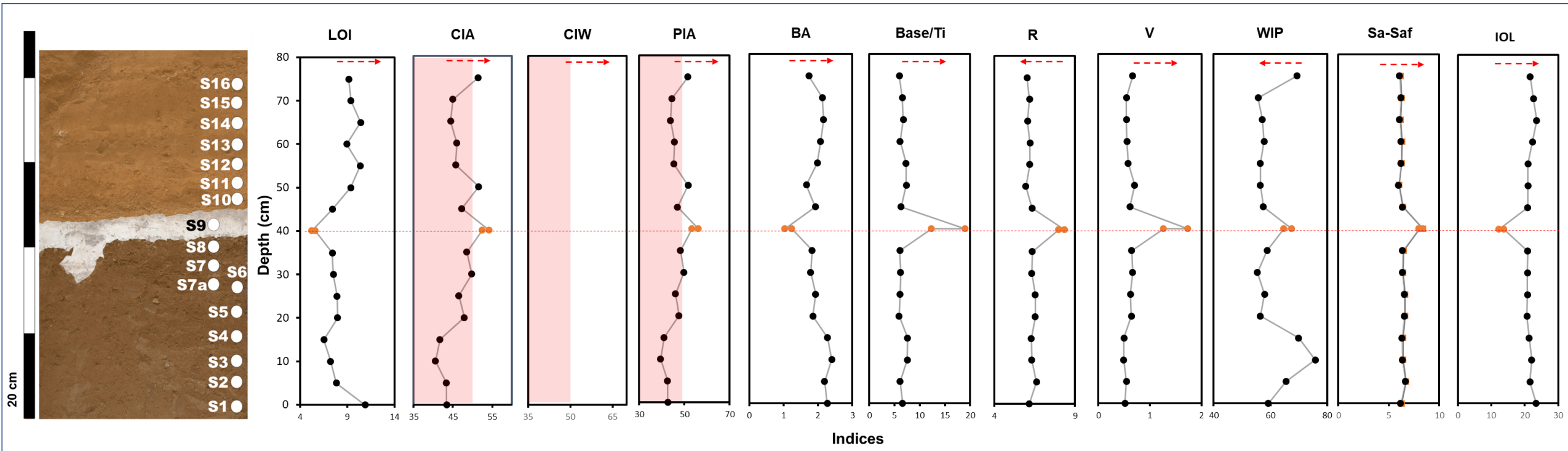
XRD Data

| Sam ID	Depth	Crystallinity%		Compounds (S-Q %)						
		Amorphous	Crystalline	Quartz	Plagioclase	Biotite	Sanidine	Laumontite	Stilbite	Clay (Smectite)
TJP_S1	0	35.5	64.5	14.9	37.8	0.7	0	12	4.1	30.5
TJP_S2	5	42	58	25	34.2	1.1	0	5.4	1.4	33
TJP_S3	10	45.1	54.9	13.3	40.6	2.2	0	9.1	7.4	27.4
TJP_S4	15	17.5	82.5	8.2	55.7	3.1	0	2.8	19	11.3
TJP_S5	20	35.7	64.3	15.6	37.1	2.2	0	7.8	18.4	18.9
TJP_S6	25	41	59	24.7	43.1	1.8	0	6.8	4.6	19
TJP_S7a	25	47.1	52.9	20.5	45.3	4.9	0	10.3	1.5	17.5
TJP_S7	30	40.7	59.3	19	41	3.6	0	4.3	18.3	13.8
TJP_S8	35	51.5	48.5	15.6	47.9	6.5	0	10.6	2.3	17
TJP_T1	40	83.2	16.8	20.7	54.7	13.5	9.5	1.6	0	0
TJP_S9	40	66	34	22.6	51.4	13.4	9.6	3	0	0
TJP_S10	45	48.3	51.7	19.9	34.9	2	20.8	3.5	0.9	18
TJP_S11	50	36.9	63.1	17.7	26.5	9.3	11.4	4.1	4.5	26.5
TJP_S12	55	32.1	67.9	28	21.6	5.6	0	6	11.2	27.6
TJP_S13	60	39.1	60.9	16.7	29.8	5.9	0	7.1	7.1	33.4
TJP_S14	65	39.7	60.3	24.3	29.9	3.5	0	7.1	0	35.2
TJP_S15	70	42.6	57.4	12.7	31.5	4.2	0	7.5	9.1	35
TJP_S16	75	38.2	61.8	19.8	35.4	2.8	0	4.3	4.7	33
TJP_EA1	40	77.3	22.3	14	57	1.5	11.5	0.7		15.3
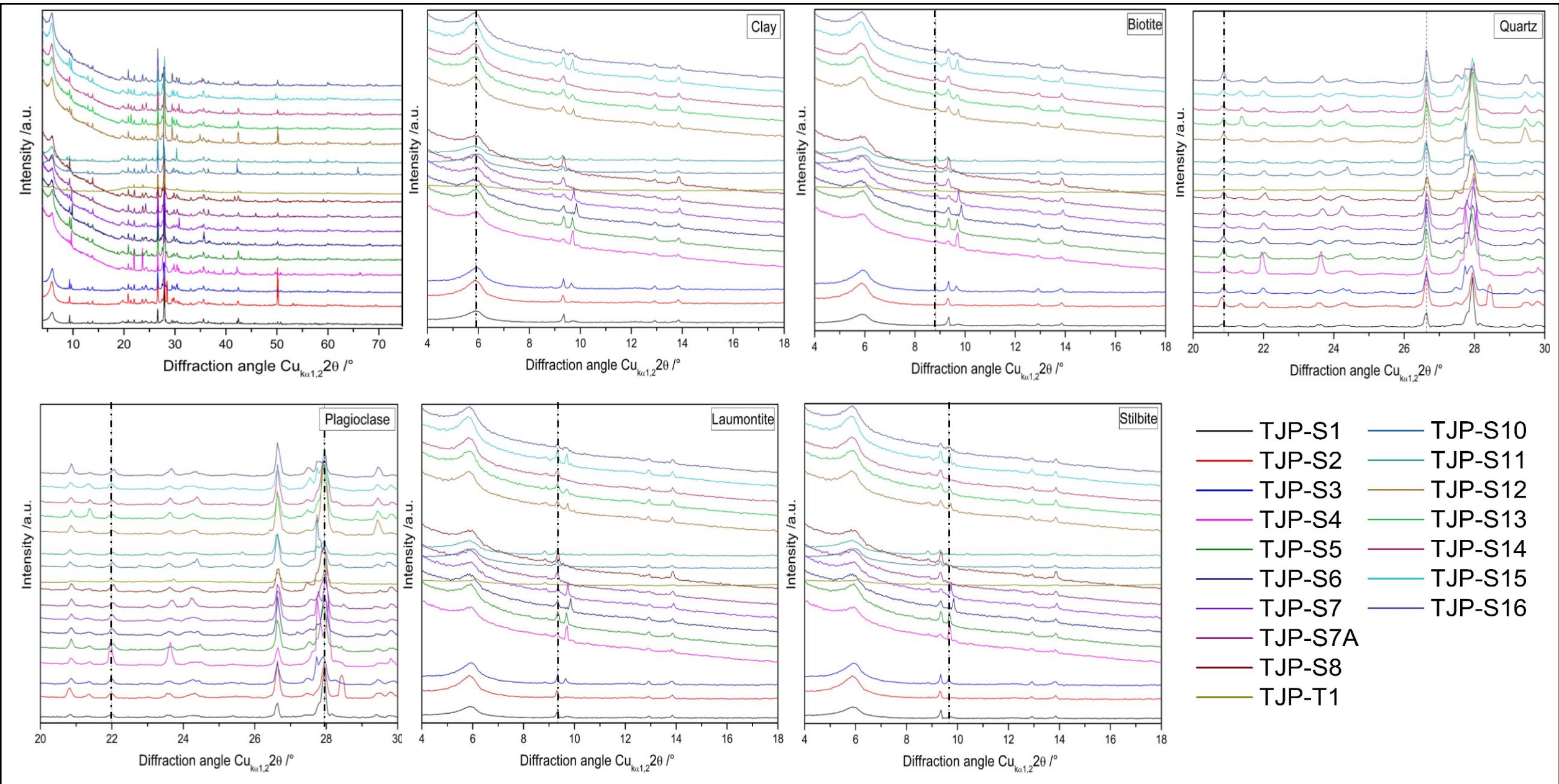
Computed Crystallinity
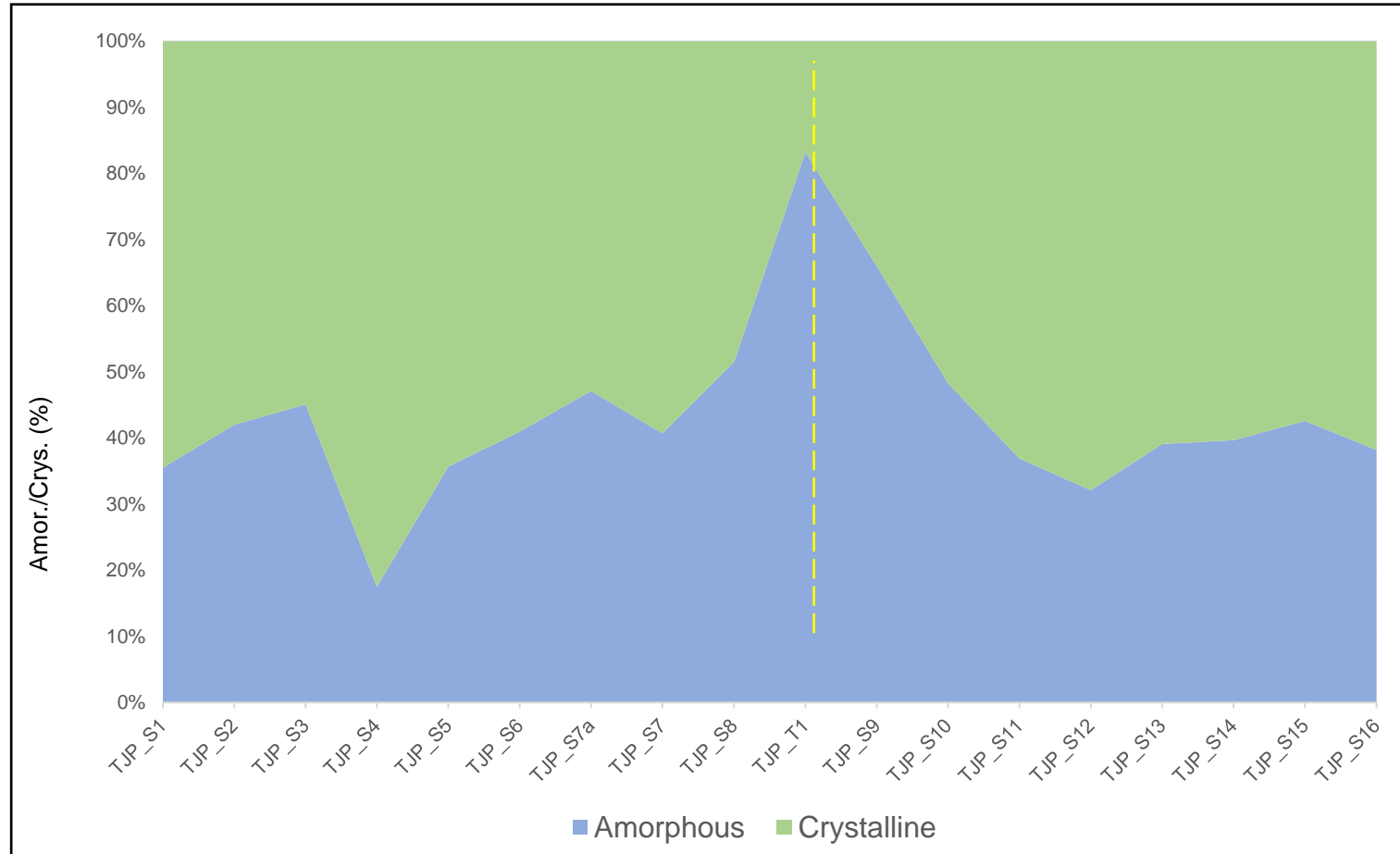
Leaf-wax Biomarker Data
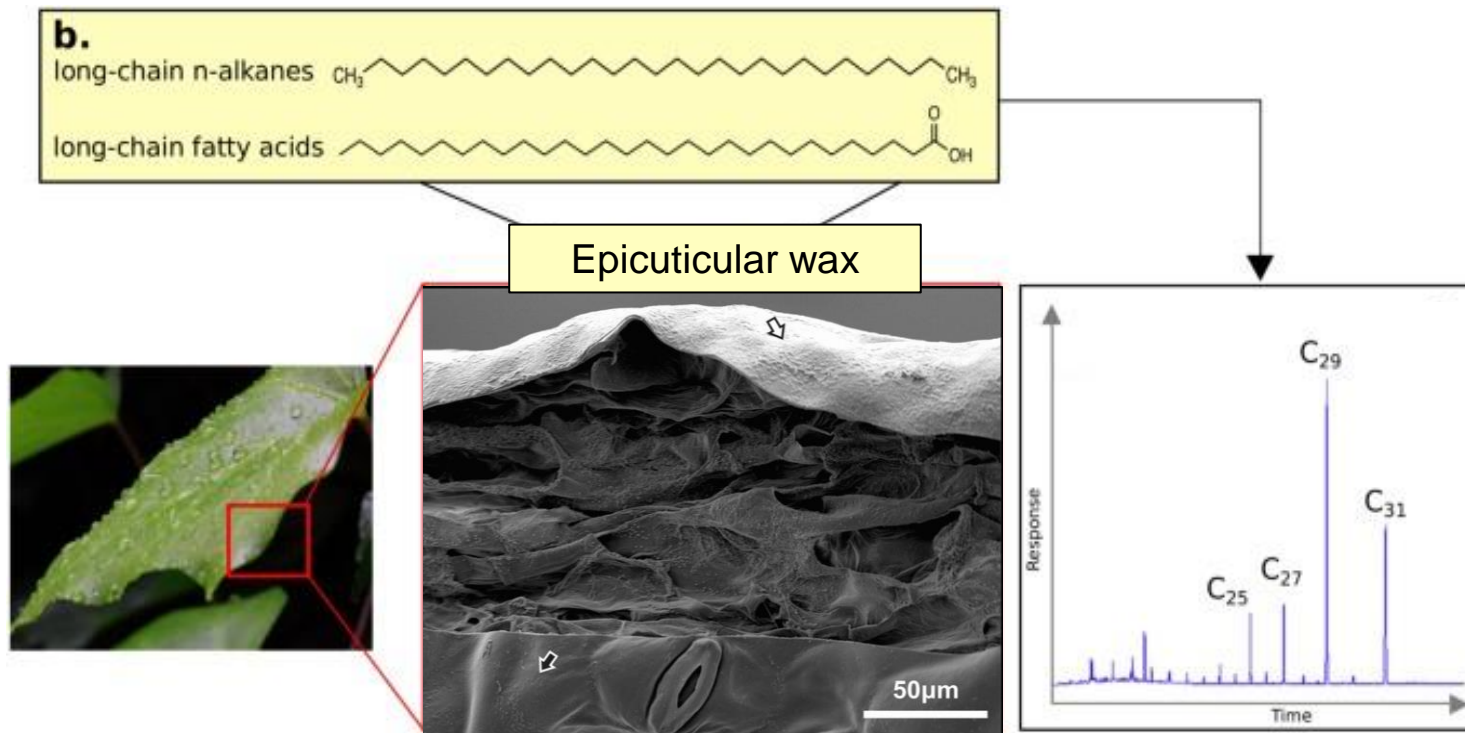
Jwalapuram: Chromatograms: *n*-alkane (*m/z* 85)
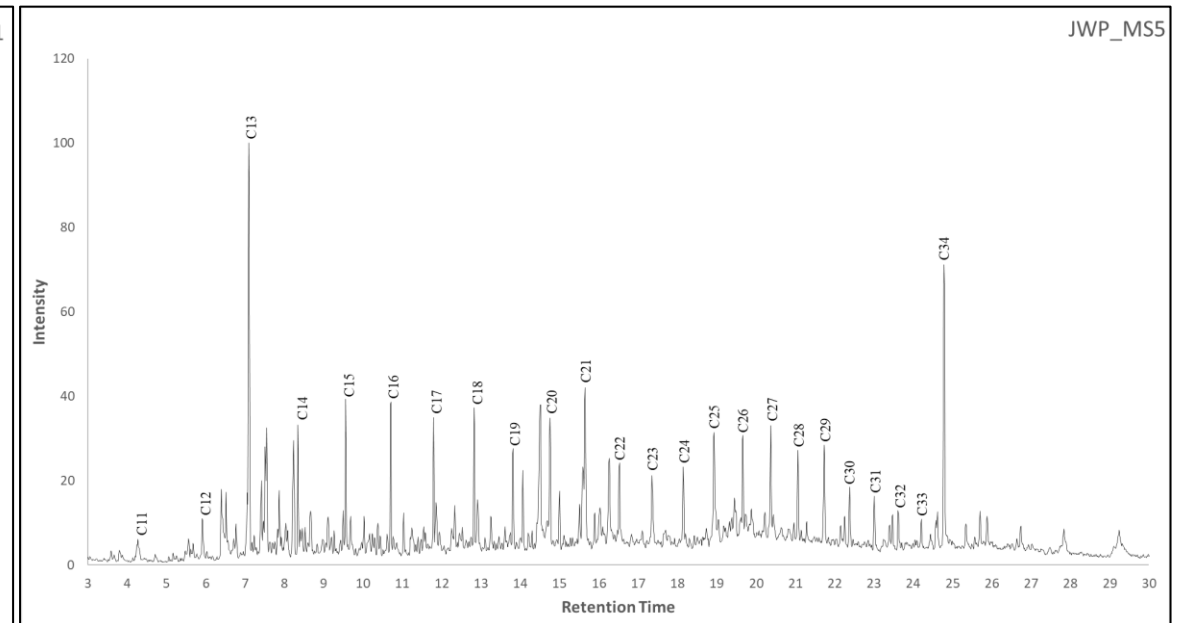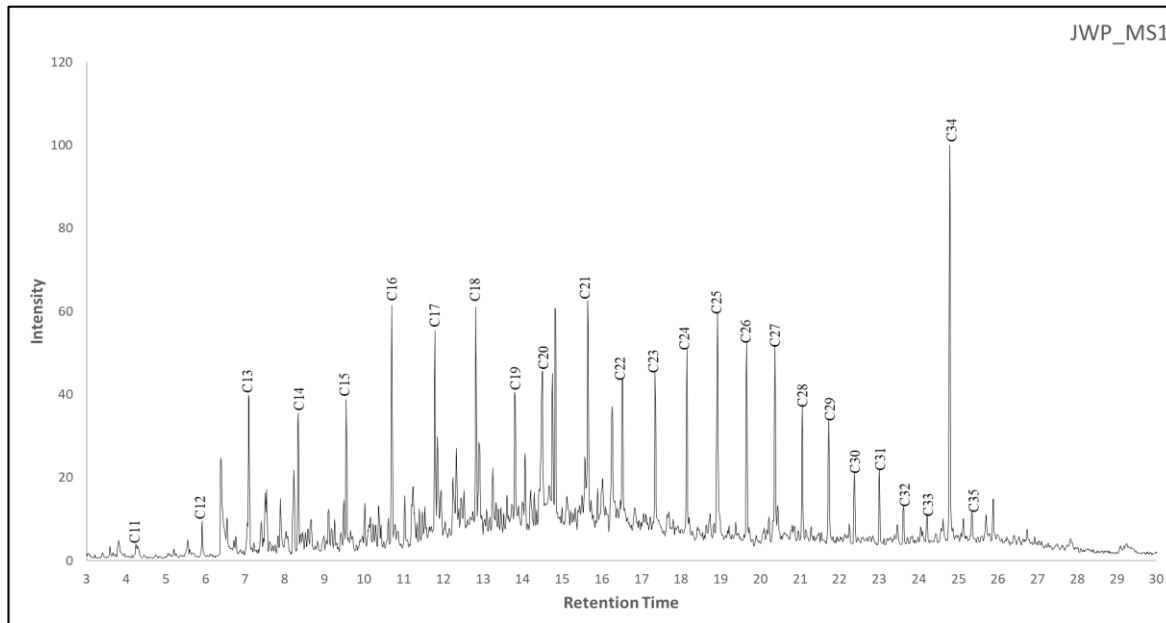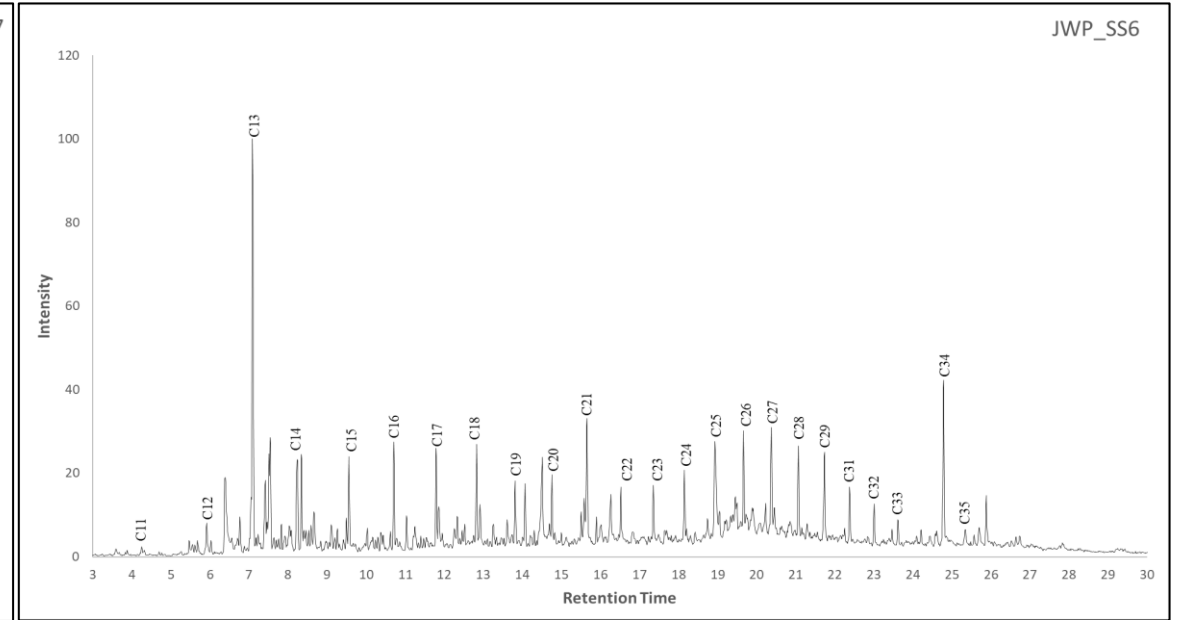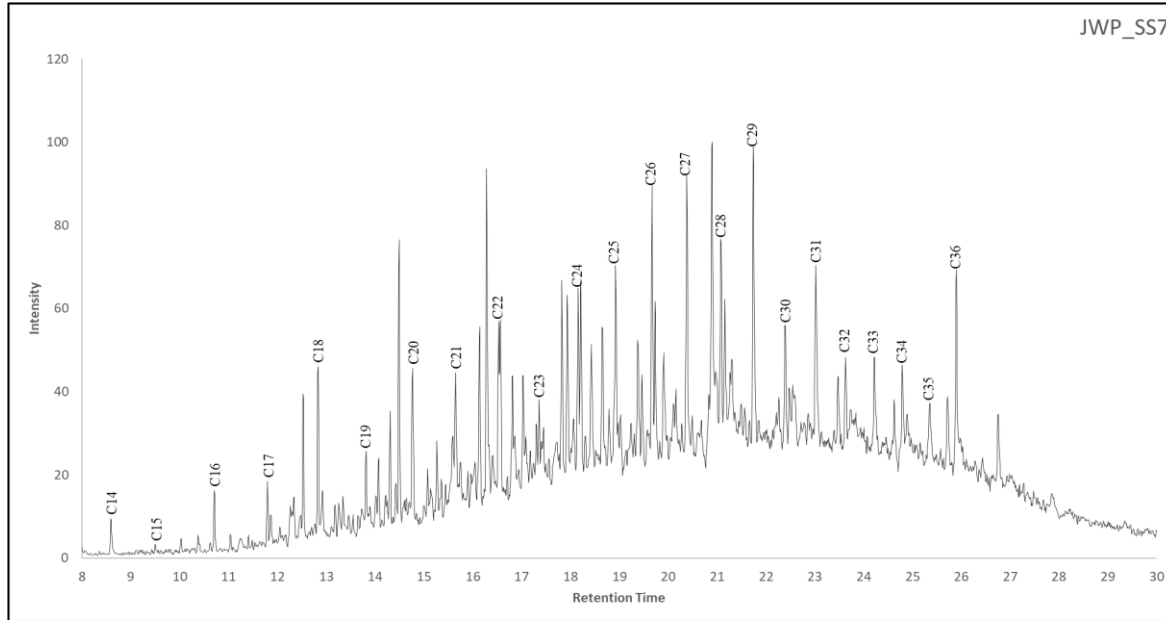
Tejpor: Chromatograms: *n*-alkane (*m/z* 85)
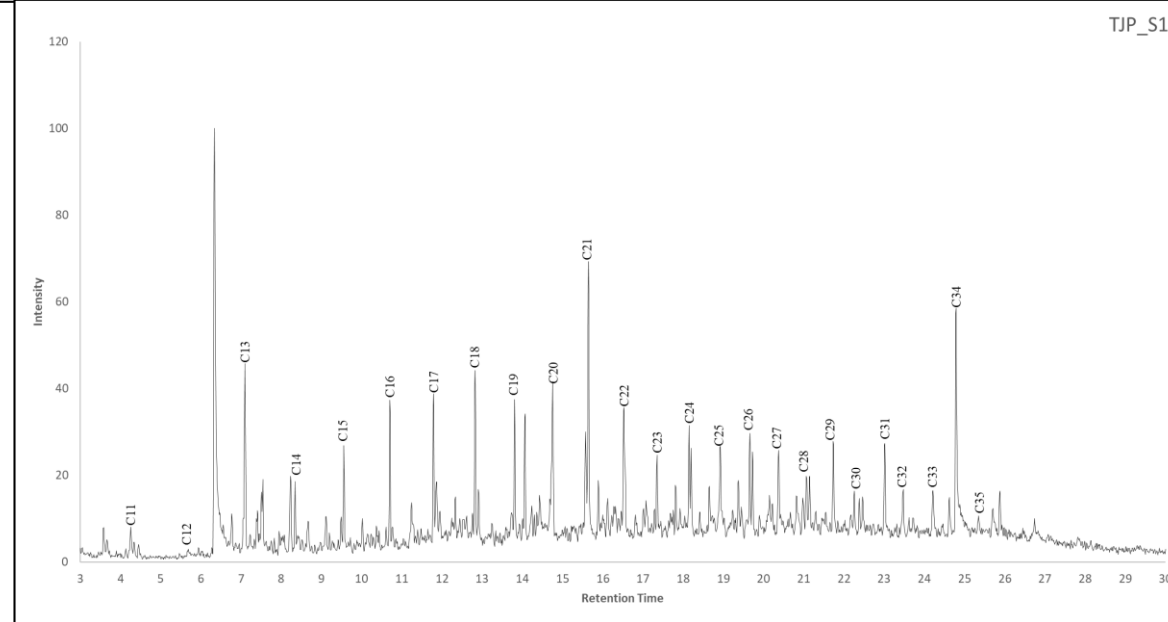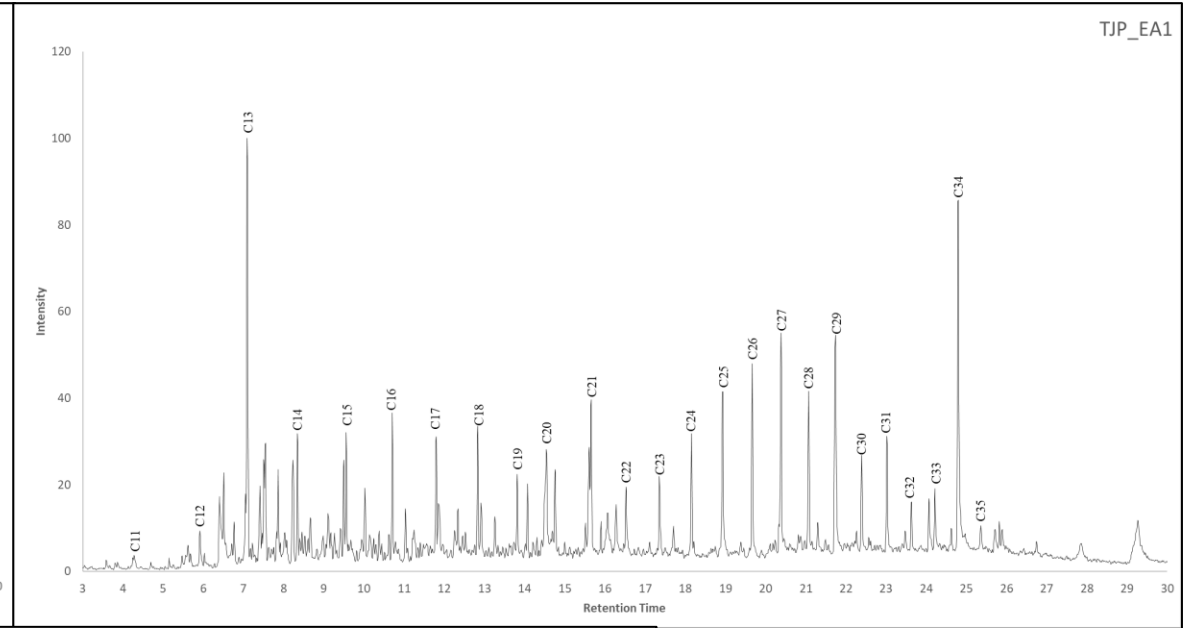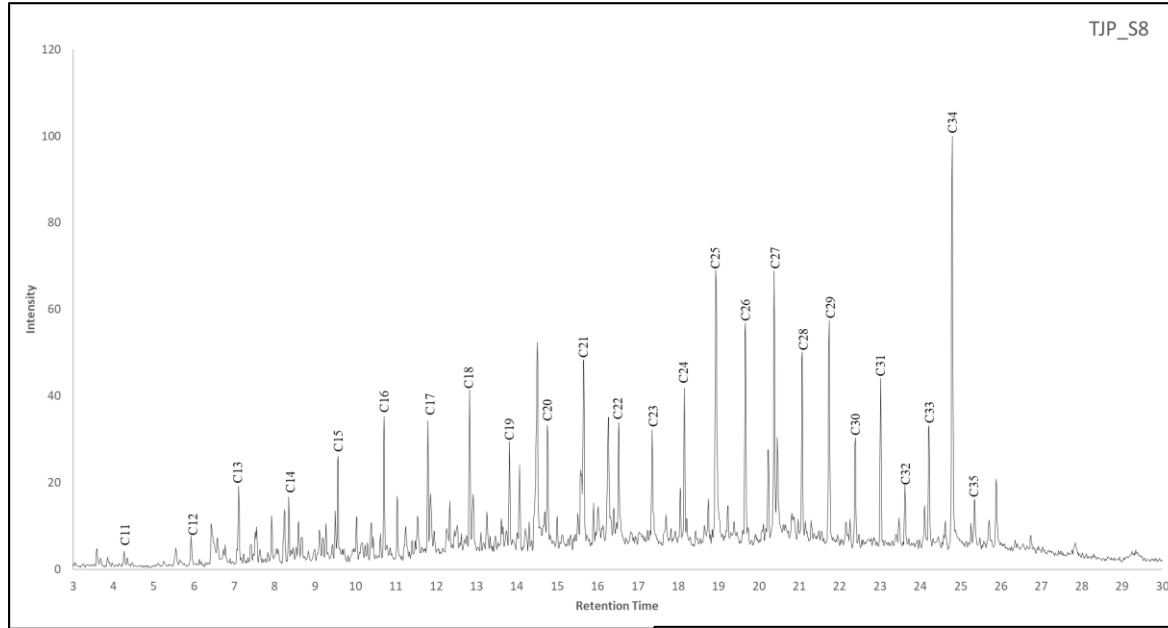
Distribution of *n*-alkane (*m/z* 85)

n-Alkane(%)	JWP_SS7	JWP_SS6	JWP_MS2	JWP_MS5	TJP_S8	TJP_EA1	TJP_S10
C11	0.12	0.08	0.42	1.27	0.06	0.64	0.18
C12		0.21	0.12	0.12	0.11	0.07	0.11
C13		1.35	0.2	0.79	0.10	0.63	0.47
C14	1.74	0.76	0.45	0.64	0.22	0.50	0.43
C15	4.33	0.73	0.46	0.72	0.29	0.43	0.62
C16	1.01	0.87	0.72	0.68	0.45	0.49	0.89
C17	0.95	0.74	0.61	0.58	0.39	0.40	0.77
C18	2.31	0.72	0.58	0.58	0.43	0.40	0.91
C19	1.09	0.45	0.34	0.40	0.30	0.08	0.70
C20	2.04	0.45	0.36	0.50	0.31	0.26	0.80
C21	7.49	3.59	1.93	2.59	2.05	2.07	5.88
C22	2.22	0.35	0.31	0.27	0.29	0.22	0.60
C23	0.9	0.45	0.25	4.16	0.10	0.45	1.17
C24	2.23	0.48	0.48	0.29	0.39	0.36	0.41
C25	2.36	0.63	0.8	0.57	0.98	0.51	0.52
C26	3.39	0.61	0.51	0.43	0.54	0.56	0.38
C27	3.3	0.72	0.49	0.42	0.76	0.64	0.42
C28	2.71	0.57	0.35	0.36	0.45	0.49	0.22
C29	3.68	0.55	0.33	0.36	0.61	0.60	0.49
C30	1.46	0.36	0.18	0.23	0.27	0.29	0.15
C31	2.15	0.29	0.19	0.21	0.44	0.36	0.40
C32	1.07	0.16	0.1	0.14	0.16	0.13	
C33	1.22	0.1	0.07	0.11	0.29	0.17	0.26
C35	0.79	0.28	0.15	0.17	0.19	0.11	0.09

Jwalapuram
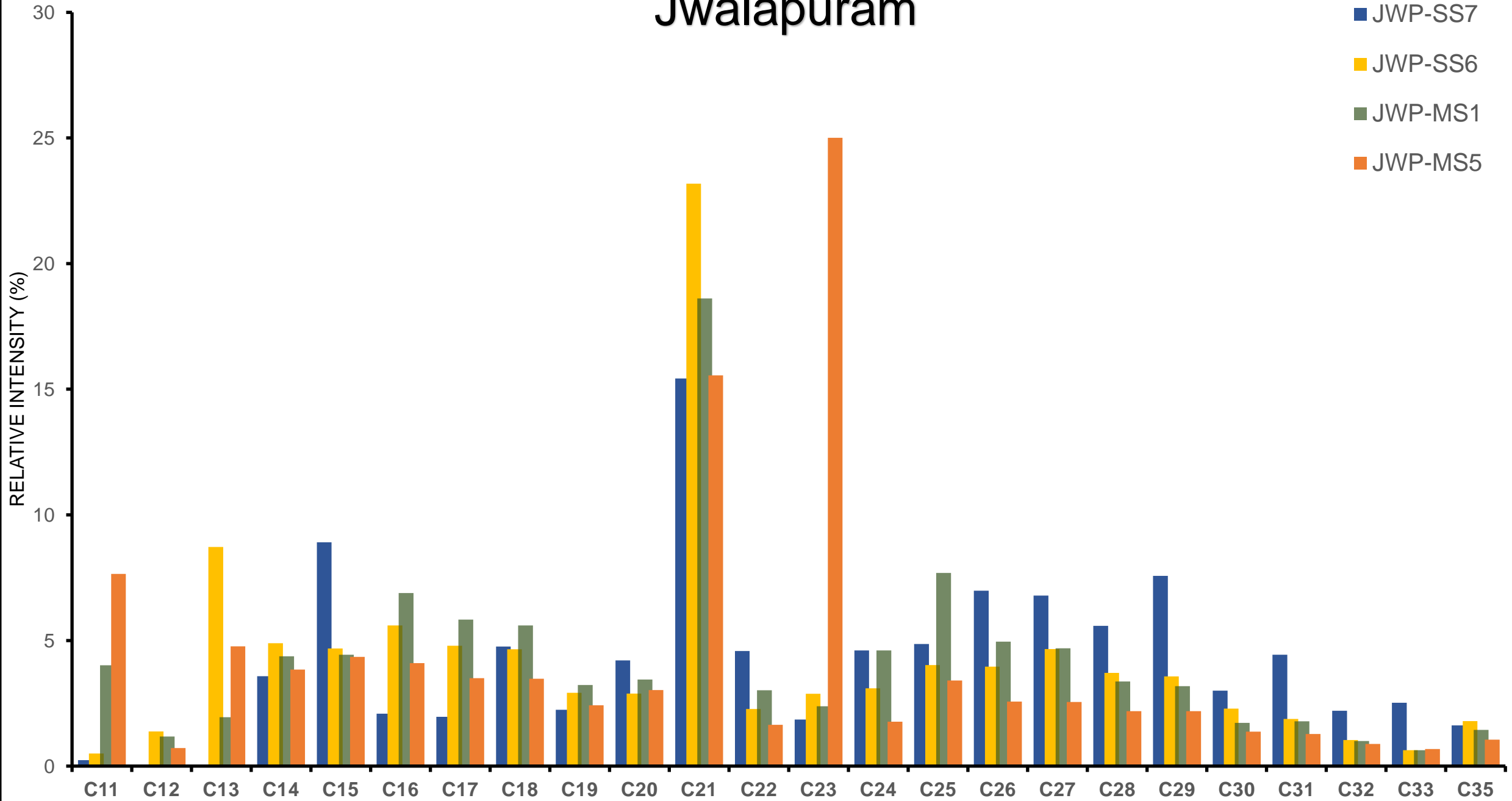
Tejpor
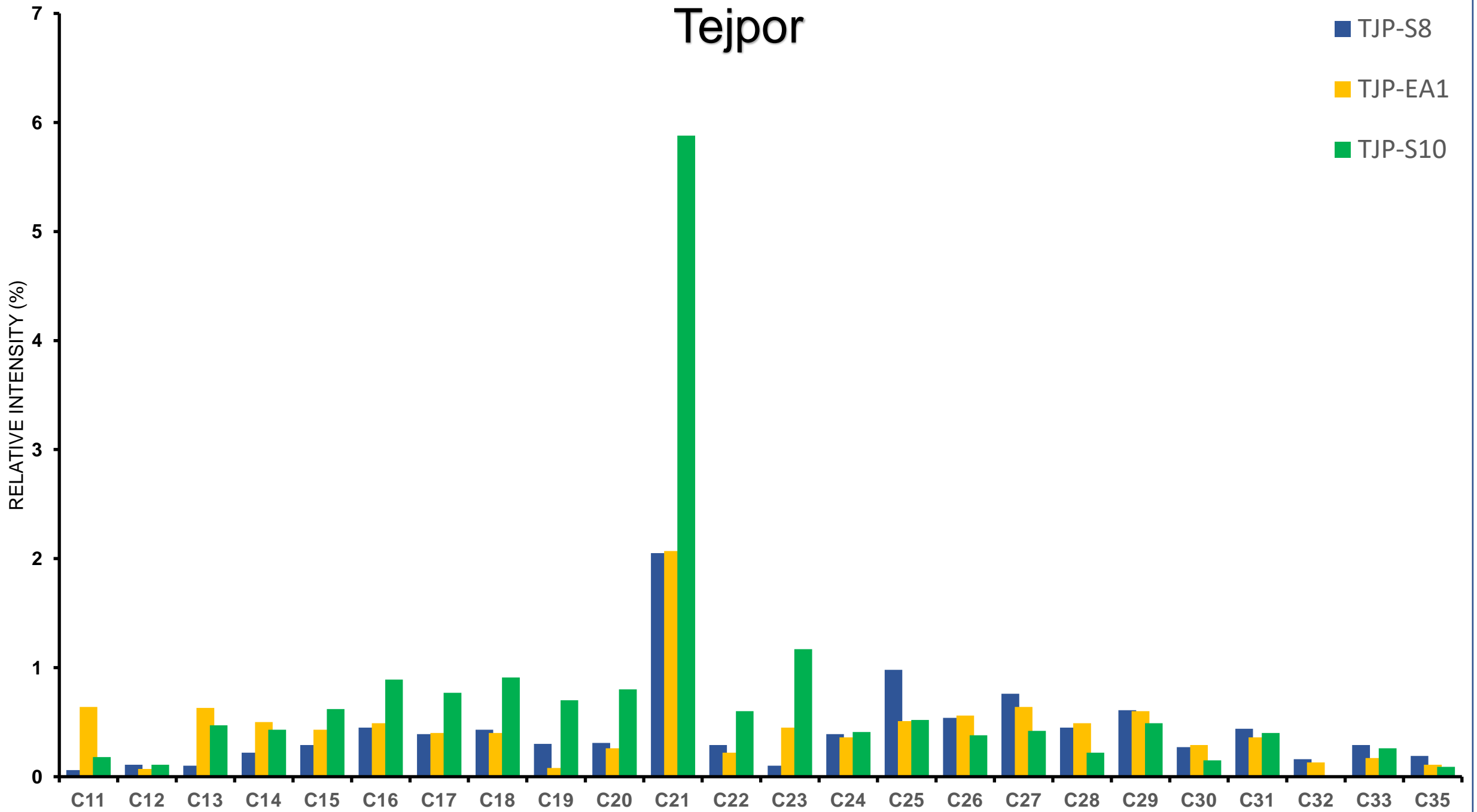
n-alkane ratio and indices

Site	CPI (C23-C35)	ACL(C23-C35)	P aq.	P wax	1/P.aq	TAR	
JWP_SS7	1.14	28.48	0.36	0.91	1.38	1.43	
JWP_SS6	1.16	27.68	0.56	0.81	2.14	0.81	
JWP_MS1	1.17	27.19	0.67	0.87	2.94	0.72	
JWP_MS5	1.61	24.63	0.89	0.25	2.97	0.58	
TJP_S8	1.30	28.15	0.51	0.96	2.71	1.85	
TJP_EA1	1.22	27.61	0.50	0.80	2.32	1.76	
TJP_S10	1.49	26.74	0.66	0.55	3.92	0.63	

Sample	C27/C31	C31/(C29+C31)	C29/(C29+C31)	C27/(C27+C31)	C27/(C27+C29)
JWP_SS7	1.53	0.37	0.63	0.61	0.47
JWP_SS6	2.48	0.34	0.66	0.71	0.57
JWP_MS1	2.63	0.36	0.64	0.72	0.60
JWP_MS5	1.99	0.37	0.63	0.67	0.54
TJP_S8	1.73	0.42	0.58	0.63	0.55
TJP_EA1	1.80	0.37	0.63	0.64	0.51
TJP_S10	1.05	0.45	0.55	0.51	0.46

P aq./P wax (%)